



This is to certify that the
dissertation entitled

A TROUGH LEAKY-WAVE ANTENNA

presented by

CARLOS ALBERTO JARAMILLO

has been accepted towards fulfillment
of the requirements for the

PhD

degree in

Electrical Engineering



Major Professor's Signature

07 December 2009

Date

A Trough Leaky-Wave Antenna

By

Carlos Alberto Jaramillo

A DISSERTATION

Submitted to
Michigan State University
in partial fulfillment of the requirements
for the degree of

DOCTOR OF PHILOSOPHY

Electrical Engineering

2009

ABSTRACT

A Trough Leaky-Wave Antenna

By

Carlos Alberto Jaramillo

Leaky-wave antennas have been an on-going research interest of U.S. government, academic and industrial research groups. One significant feature of these antennas is that the voltage standing wave ratio (VSWR) bandwidth can be greater than that of resonant antennas. This is principally due to the fact that the radiation mechanism is attributed to a traveling-wave as compared to the standing-wave that is responsible for radiation in resonant antennas. Another important aspect of leaky-wave antennas is that the radiation pattern bandwidth is regrettably somewhat narrow since the main-lobe direction varies with operational frequency. This dissertation deals with the effective design of trough leaky-wave (TLW) antennas. A TLW antenna is an electrically narrow trough in a ground plane excited using a coaxial probe feed and terminated in a lumped load. In this antenna, a traveling wave propagates along the aperture with a complex propagation constant which can be computed using the transverse resonance method (TRM) assuming an infinitely long antenna. An alternative approach, that considers the aperture length, is the finite element boundary integral (FE-BI) method. In this work, both formulations are developed and implemented numerically not only to compute the propagation constants but also the antenna impedance and radiation pattern. The major contribution of this work lies in the balun used to feed in concert with the load to terminate the antenna.

To My Parents and Wife

ACKNOWLEDGMENTS

First of all, I would like to thank God for His favor and grace.

During my years at MSU I had the opportunity to meet excellent people that help me to accomplish one of my dreams in my life, a Ph.D in Electrical Engineering.

I would like to express my gratitude to my advisor Dr. Leo C. Kempel and the members of my Ph.D. committee, Dr. B. Shanker, Dr. Edward Rothwell and Dr. Gouwei Wei. Thankyou for participating in this committee and providing their guidance and support when it was needed. I would also like to acknowledge Dr. Stephen W. Scheneider of the Air Force Research Laboratory for motivating this research and collaboration with Dr. Kempel and myself.

Special thanks to the people which through their financial assistance and support made it possible for me to complete this work. Thanks to Dr. Barbara O'Kelly and Dr. Percy Pierre for their confidence during my years at MSU. I would like to thank to Kathleen Kreh and the former graduate secretary Sheryl Hulet for their devotion to their work

I also want to express my gratitude to my fellow graduate students that in a way or another help me over the years at MSU.

A very special thanks to my friends in Puerto Rico Manuel and Carmen Garcia, they were always present during this journey.

Finally, I would like to thank to my Parents Oliva and Pablo, my sisters Martha and Patricia, my brother Pablo and my lovely wife Yanira for their love and sacrifice.

TABLE OF CONTENTS

LIST OF TABLES	vii
LIST OF FIGURES	viii
KEY TO SYMBOLS AND ABBREVIATIONS	xii
 CHAPTER 1	
Introduction	1
1.1 Leaky wave antennas background	1
1.2 Surface wave and leaky waves	8
1.3 Operation modes of leaky-wave antennas	12
1.4 Radiation characteristics of a TLW antenna	14
 CHAPTER 2	
Analytical solution for the TLW antenna	22
2.1 Transverse resonance method	22
2.2 TLW antenna driving point impedance	33
 CHAPTER 3	
Numerical solution for the TLW antenna	42
3.1 Finite element boundary integral method	42
3.2 Finite element formulation	43
3.3 Boundary integral formulation	48
3.4 Antenna feed and load	64
3.5 FE matrix entries using tetrahedrons	65
3.6 BI matrix entries using triangles	74
3.6.1 Numerical integration of BI equations	82
3.6.2 BI self term evaluation	84
3.7 FE-BI program structure	88
3.7.1 Pre-processing	88
3.7.2 Meshing	89
3.7.3 Pre-assembly of FE-BI matrices for the TLW antenna	91
3.7.4 Matrix assembly	92
3.7.5 Matrix solution of FE-BI linear system using biconjugate gra- dient (BiCG) method with preconditioning	92
3.7.6 Post-processing	93
3.7.6.1 Input Impedance, reflection coefficient, and VSWR	94
3.7.6.2 Radiation pattern	94
3.7.6.3 Propagation constants	98

CHAPTER 4	
Antenna design and results	101
4.1 Design of the RT/Duroid 5880-filled TLW antenna	101
4.2 Code validation	106
4.3 Air-filled TLW antenna	111
CHAPTER 5	
Conclusions and future work	135
APPENDIX A	
Review of some complex variable functions	138
A.1 The exponential function $w(z) = e^z$	138
A.2 The square root function $w(z) = \sqrt{z}$	139
APPENDIX B	
Thin-substrate approximation for microstrip patch antennas	142
APPENDIX C	
Proof of some properties of RWG basis function	145
C.1 Proof of expression (3.114)	145
C.2 RWG basis function are free of charge accumulation over its support .	148
APPENDIX D	
Analytical computation of integrals with singularities	151
D.1 Integrals with uniform source distribution	151
D.2 Integrals with linearly varying source distribution	153
BIBLIOGRAPHY	156

LIST OF TABLES

Table 3.1	Tetrahedron edge-node local conection.	73
Table 3.2	Triangular coordinates and integration weights [38].	85
Table 4.1	RT/Duroid 5880-filled TLW antenna banwidth for three different values of h	101
Table 4.2	RT/Duroid 5880-filled TLW antenna banwidth for three different values of w	104
Table 4.3	RT/Duroid 5880-filled TLW antenna design parameters.	104
Table 4.4	Air-filled TLW antenna design parameters.	120
Table 4.5	Air-filled TLW antenna circular termination design parameters.	123

LIST OF FIGURES

Figure 1.1	(a) Geometrical description of the TLW antenna (b) Feeding technique.	2
Figure 1.2	Electric field for the EH_{10} mode.	4
Figure 1.3	Illustration of HWLW antenna.	6
Figure 1.4	Field structure for a TLW antenna.	7
Figure 1.5	Leakage from a closed wave guide opened at the top (after [3]).	11
Figure 1.6	Typical dispersion characteristics of the hybrid leaky-wave EH_{10} mode (after [24]).	13
Figure 1.7	Equivalence models for the trough leaky wave antenna mounted on an infinite flat electric ground plane.	15
Figure 1.8	H-plane amplitude pattern for a forward traveling wave distribution aperture mounted on an infinite ground plane.	19
Figure 2.1	Transmission line model of the transverse cross-section of the TLW antenna.	25
Figure 2.2	Transmission line used to illustrate the TRM.	26
Figure 2.3	Shifting reference planes in the transmission line.	28
Figure 2.4	Complex plane representation of $k_z = \pm\sqrt{k_0^2 - k_x^2}$	31
Figure 2.5	Propagation constant for a TLW antenna filled with RT/Duroid 5880.	32
Figure 2.6	Propagation constants for a TLW antenna filled with RT/Duroid 5880 and a TLW antenna filled with air.	34
Figure 2.7	Real and imaginary part of the driving point impedance for an infinitely long TLW antenna (RT/Duroid 5880-filled).	38
Figure 2.8	VSWR for an infinitely long TLW antenna (RT/Duroid 5880-filled).	39
Figure 2.9	Real and imaginary part of the driving point impedance for an infinitely long TLW antenna (air-filled).	40
<i>Figure 2.10</i>	VSWR for an infinitely long TLW antenna (air-filled).	41

Figure 3.1	Geometry of a three-dimensional cavity-backed aperture in an infinite ground plane.	43
Figure 3.2	Tetrahedron element and local edge-node numeration.	66
Figure 3.3	Two triangles sharing an edge and their geometrical parameters.	80
Figure 3.4	Local coordinates for triangle T^q	83
Figure 3.5	Projections of \vec{r} , \vec{r}' , and \vec{r}_j onto the plain that contains T^q	87
Figure 3.6	Different configurations of surfacemesh: (a)Rectangular, (b)Bow-tie, (c)Circular.	90
Figure 4.1	Effect of the variation of h in the propagation constants for the RT/Duroid 5880-filled TLW antenna.	102
Figure 4.2	Effect of the variation of w in the propagation constants for the RT/Duroid 5880-filled TLW antenna.	103
Figure 4.3	TLW antenna with terminations and design parameters. (a)Front view. (b)Side view.	105
Figure 4.4	Real part of the input impedance of the RT/Duroid 5880-filled TLW antenna simulated using ctets and tet.	107
Figure 4.5	Imaginary part of the input impedance of the RT/Duroid 5880-filled TLW antenna simulated using ctets and tet.	108
Figure 4.6	Radiation pattern at F=8.0 GHz of the RT/Duroid 5880-filled TLW antenna simulated using ctets and tet.	109
Figure 4.7	VSWR of the RT/Duroid 5880-filled TLW antenna.	110
Figure 4.8	Magnitude of E_y of the RT/Duroid 5880-filled TLW antenna.	112
Figure 4.9	Phase of E_y at 6 GHz of the RT/Duroid 5880-filled TLW antenna.	113
Figure 4.10	Phase of E_y at 7 GHz of the RT/Duroid 5880-filled TLW antenna.	114
Figure 4.11	Phase of E_y at 8 GHz of the RT/Duroid 5880-filled TLW antenna.	115
Figure 4.12	Slope term computed via FE-BI and the least square method.	116
Figure 4.13	Constant term computed via FE-BI and the least square method.	117

Figure 4.14	Ratio constant to slope term computed via FEBI and least square method.	118
Figure 4.15	Propagation constant of the RT/Duroid 5880-filled TLW antenna computed using FE-BI and TRM.	119
Figure 4.16	Effect of the variation of h in the propagation constants for the air-filled TLW antenna.	121
Figure 4.17	Effect of the variation of w in the propagation constants for the air-filled TLW antenna.	122
Figure 4.18	Different terminations: (a)Rectangular (b)Bow-tie (c)Circular (d)Side view.	124
Figure 4.19	VSWR for the air filled TLW antenna with different terminations.	125
Figure 4.20	Radiation pattern at 12 GHz for the air filled TLW antenna with different terminations.	126
Figure 4.21	Input impedance of the air-filled TLW antenna with circular termination.	127
Figure 4.22	Magnitude of E_y of the air-filled TLW antenna with circular termination.	128
Figure 4.23	Phase of E_y at 6 GHz of the air-filled TLW antenna with circular termination.	129
Figure 4.24	Phase of E_y at 9 GHz of the air-filled TLW antenna with circular termination.	130
Figure 4.25	Phase of E_y at 12 GHz of the RT/Duroid 5880-filled TLW antenna with circular termination.	131
Figure 4.26	Propagation constant of the air filled TLW antenna with circular termination.	132
Figure 4.27	Efficiency of the TLW antenna with circular termination.	133
Figure 4.28	Ratio P_{RL} to P_{in} of the TLW antenna with circular termination.	134
Figure A.1	(a) A circular contour in the z plane. (b) The mapping of the z plane into w plane by the function e^z	140

Figure A.2	(a) A circular contour in the z plane. (b) The mapping of the z plane into w plane by the function \sqrt{z}	141
Figure B.1	Convergence for equation (B.6), ($\epsilon_r = 2.33$).	144
Figure C.1	Current interpolation between two triangles.	150
Figure D.1	Geometrical parameters associated with the evaluation of potential integrals over the triangle T^q (after [50]).	154

KEY TO SYMBOLS AND ABBREVIATIONS

TLW: Trough Leaky-Wave

TRM: Transverse Resonance Method

TE: Transverse Electric

TM: Transverse Magnetic

VSWR: Voltage Standing Wave Ratio

HWLW: Half-Width Leaky-Wave

FE-BI: Finite Element-Boundary Integral

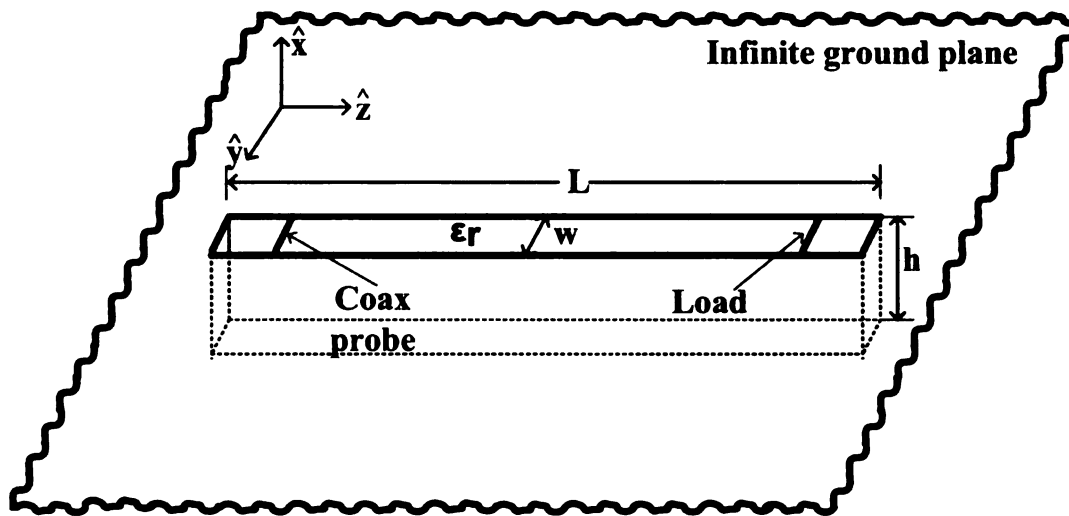
CHAPTER 1

INTRODUCTION

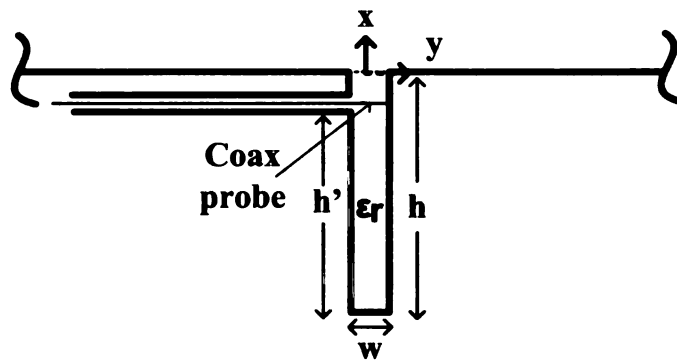
1.1 Leaky wave antennas background

A geometrical description of the Trough Leaky-Wave (TLW) antenna considered in this research is shown in Figure 1.1. The TLW antenna is excited by a coaxial probe and terminated by a lumped load. The trough may be filled with a dielectric (ϵ_r), and the infinite ground plane is a perfect electric conductor. The aperture width is less than one tenth the dielectric wavelength (i.e., $w < \lambda_m/10$), where $\lambda_m = \lambda_0/\sqrt{\epsilon_r}$, λ_0 is the free space wavelength. The aperture length is on the order of seven times the dielectric wavelength (i.e., $L \approx 7\lambda_m$); and the thickness of the trough is on the order of one fourth the dielectric wavelength (i.e., $h \approx \lambda_m/4$).

In the 1950's, structures similar to the TLW antenna were considered. These structures were based on closed waveguides with a cut along the side of the waveguide to radiate power. Rumsey [1] developed a variational procedure to derivate approximate formulas for the complex propagation constant and field configuration of an infinite-length, traveling-wave-slot antenna. His configuration was a rectangular wave-guide. At the same time, Harrington [2] formulated another variational method to determine the attenuation and phase constants for the fields along a slotted circular wave-guide. In both works, analytic results were validated with experimental data. Goldstone *et al.* [3] used the Transverse Resonance Method (TRM) approach to compute the complex propagation constants in terms of the



(a)



(b)

Figure 1.1. (a) Geometrical description of the TLW antenna (b) Feeding technique.

transverse dimensions of the leaky-wave antenna. Hines *et al.* [4] identified three categories of slotted rectangular guides depending on whether the excitation mode was TE, TM or hybrid TE-TM. In addition, they presented analytic and experimental data for these three cases. Oliner [5] has made significant contributions explaining the leaky wave phenomena not only for rectangular slot waveguides but also for dielectric waveguides (i.e., microstrip leaky-wave antennas).

Microstrip leaky-wave antennas are wide-microstrip lines that operate primarily as traveling wave antennas. As a wave propagates along the guiding structure energy leaks out in the form of radiation. Ideally, the structure is designed to be electrically long, by the time the wave reaches the end termination most of the energy has leaked out into free space and therefore, the reflected power does not affect the input match. This leads to a wide input impedance bandwidth and a large effective aperture illumination with a narrow radiated beamwidth. If the feed end of the antenna is properly designed, and a suitable termination load is placed at the opposite end of the antenna, a microstrip leaky-wave antenna is essentially a printed version of the classic Beverage antenna commonly used by the amateur radio community [6]. Such antennas typically can be designed for 25% or more VSWR bandwidth (e.g., VSWR of two or less over a fractional bandwidth of 25% of the center frequency) and have good gain. Unfortunately this antenna diverges from the “perfect antenna” in that it must be relatively long to achieve high radiation efficiency, and the radiation pattern main lobe steers from near broadside to near end-fire across the operational bandwidth of the antenna. Nevertheless, this antenna

is well-suited for applications requiring wide bandwidth and a thin profile. Hence, there is interest in characterizing its operational characteristics and developing effective design procedures.

Microstrip leaky-wave antennas have been the subject of significant research by a number of investigators [7, 8, 9, 10, 11]. Their radiation mechanism is well known, and different feeding and termination techniques have been proposed [10, 11]. Figure 1.2 illustrates the electric field for the EH_{10} mode used by a microstrip leaky-wave antenna.

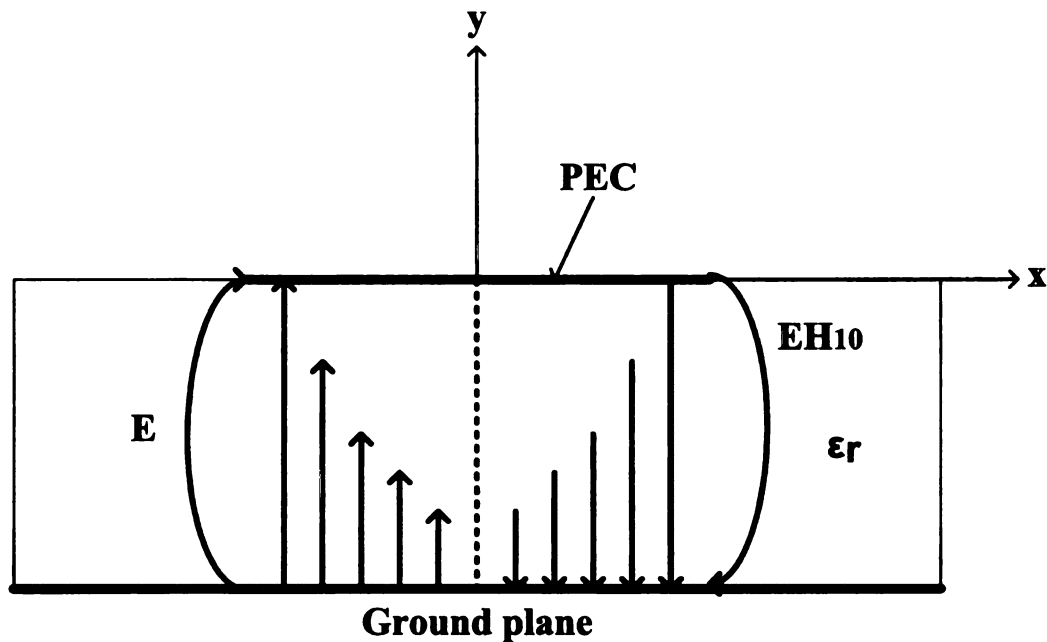


Figure 1.2. Electric field for the EH_{10} mode.

In Figure 1.2, the arrow length is an indication of the electric field strength. Hence, the highest field strength is near the edge of the antenna while a null is formed along the centerline. Since the potential between the ground plane and the microstrip is proportional to the substrate thickness (assumed much less than a wavelength for this work) and to the normal component electric field strength, feeding the antenna near an edge will result in a high driving-point impedance (assuming a matched load at the other end of the antenna). On the other hand, attempting to feed the antenna along the centerline would lead to a low driving-point impedance. Hence, by adjusting the transverse feed position, the driving-point impedance can be adjusted as needed.

An alternative to the traditional microstrip leaky-wave antenna design is the so-called half-width leaky-wave (HWLW) antenna that makes use of the observation that a physical short may be placed along the centerline of the antenna (Figure 1.2) without perturbing the modal fields. This antenna has undergone considerable recent work [12], [14], [15]; one of the principal advantages of this design is the fact that the feeding structure is considerably simplified. Traditional, full-width microstrip leaky-wave antennas, usually require a rather complex feeding structure (for example [16]) to preferentially excite the EH_{10} mode over the fundamental EH_{00} mode (i.e., the usual microstrip Transmission line mode). On the other hand, the HWLW antenna will automatically suppress the EH_{00} mode since it is quasi-TEM, and therefore cannot be supported by the structure shown in Figure 1.3. Hence, the HWLW antenna can be fed with a relatively simple feed, such as a coaxial probe.

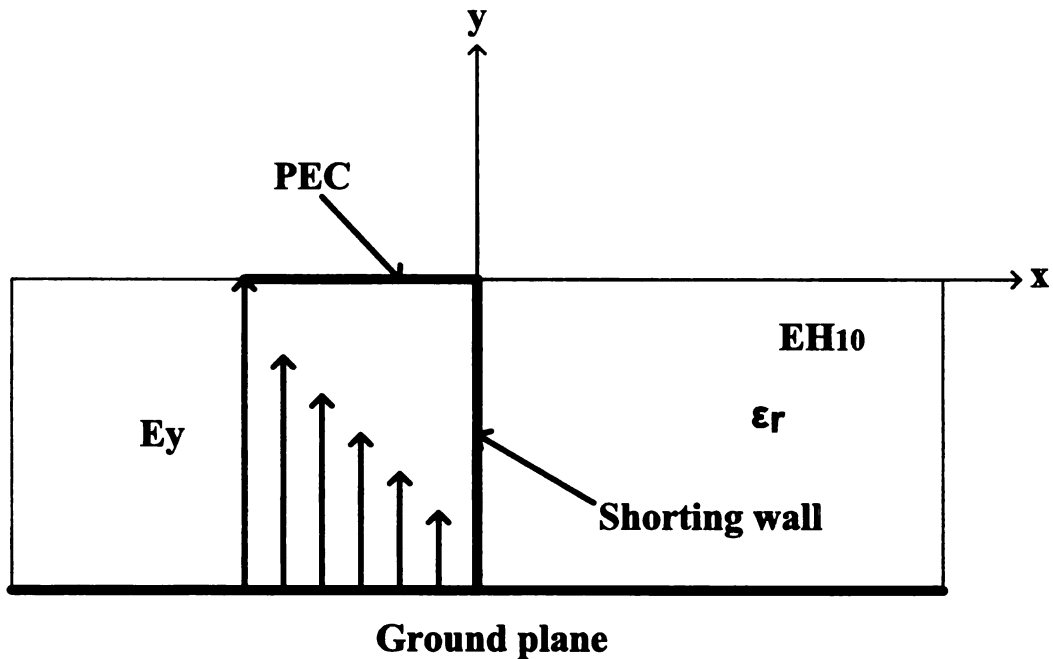


Figure 1.3. Illustration of HWLW antenna.

If the HWLW antenna is rotated by 90° , it is possible to obtain the trough leaky-wave (TLW) antenna as shown in Figure 1.4. One main advantage of this configuration is that the antenna can be integrated with a vehicle and does not require a stand-off dielectric (e.g., the trough can be air-filled to increase bandwidth), thereby reducing drag. A rough sketch of the anticipated electric field inside the cavity of the trough antenna is also shown on Figure 1.4. Due to the narrow trough width, the polarization of the electric field is solely in the y direction, and due to the metallic walls at the start and end of the trough, the tangential component

of the electric field is zero at both ends of the cavity. Therefore some type of end termination design feature is necessary to maintain the bandwidth of the antenna. Should termination features be omitted, the antenna's VSWR bandwidth will be severely limited due to the reflection from the nearby vertical wall of the cavity. In addition, placing the feed near such a vertical wall will "short-out" the feed, leading to an inefficient radiator. The major contribution of this dissertation is the design and analysis of one of such termination scheme.

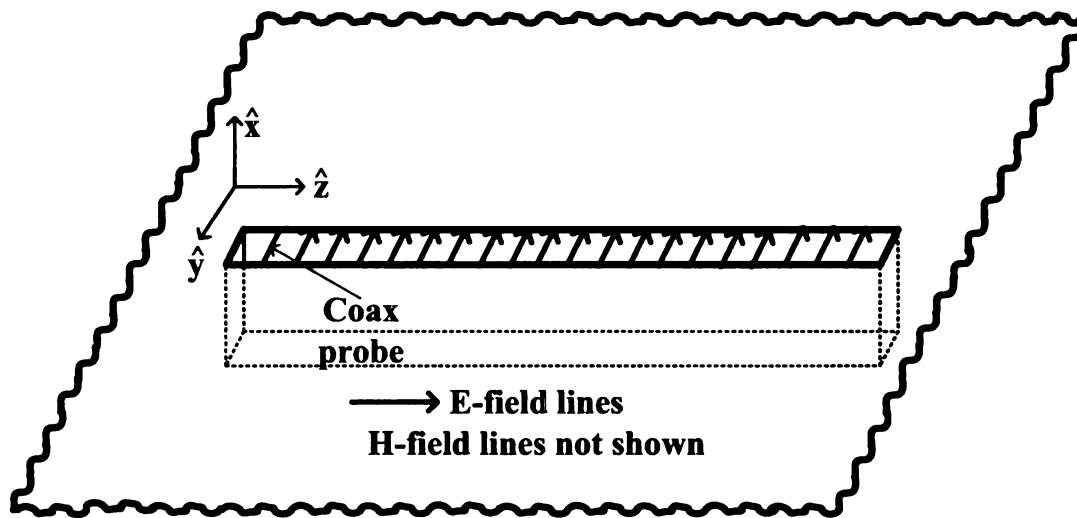


Figure 1.4. Field structure for a TLW antenna.

The objective of this research is to analyze the properties of the TLW antenna using the transverse resonance method (TRM) and the finite element boundary integral (FE-BI) method [17]. Using these two methods, the propagation constant,

the impedance and the radiation characteristics of the TLW antenna are computed. In this research, it is vital to understand how the propagation constant is affected by geometry and electric changes in the structure in order to improve the antenna's far field pattern and bandwidth. Based on FE-BI simulations the TLW antenna terminations are designed. In order to validate the analytic and numerical studies a prototype is fabricated and tested.

This dissertation is organized as follows: the rest of Chapter 1 presents a theory review about leaky-wave antennas. Chapter 2 deals with analytic considerations of an infinitely long TLW antenna in order to compute its propagation constants and driving point impedance. Chapter 3 presents the formulation of the FE-BI method used to perform numerical analysis of the TLW antenna. In this chapter, details of code implementation are given. Chapter 4 validates the code implementation and shows analytic and numerical results. In addition, it contains details about the TLW antenna design, and presents simulation results of the TLW antenna. Conclusions and future work are presented in Chapter 5.

1.2 Surface wave and leaky waves

Surface-wave antennas and leaky wave antennas are related because they may be analyzed as traveling wave type antennas [25], [26]. Consider the TLW antenna shown on Figure 1.4. The wave number in free space for an antenna is related to the propagation constants in x , y , and z by the continuity equation,

$$k_x^2 + k_y^2 + k_z^2 = k^2, \quad (1.1)$$

where $k_i = \beta_i - j\alpha_i$ and $i = x, y, z$.

Knowing the attenuation coefficient (α) and the phase coefficient (β), it is possible to characterize the operational frequencies of a leaky wave antenna along with some of the radiation behavior; this idea will be clarified later. In air, k is real and can be written in terms of the wavelength λ by $k = \beta = 2\pi/\lambda$, and in terms of the speed of light c by $k = \omega/c$. The phase constant β_z can also be written in terms of the surface wavelength λ_z by $\beta_z = 2\pi/\lambda_z$ and in terms of the surface phase velocity v_z by $\beta_z = \omega/v_z$. Therefore,

$$\frac{\beta_z}{k} = \frac{\lambda}{\lambda_z} = \frac{c}{v_z}. \quad (1.2)$$

Traveling wave antennas are classified according to (1.2). When this ratio is equal or greater than one, such structures are known as slow wave or surface wave antennas because their phase velocity is equal to or less than the speed of light. In a surface wave antenna, a wave propagates along an interface between two media. The radiation only occurs at discontinuities and nonuniformities. Bagby and Nyquist [27] have identified this behavior in microstrip lines as the surface wave regime. When the terms in (1.2) are less than 1, the structures are known as fast-wave or leaky-wave antennas because their phase velocity is greater than the speed of light. In these antennas a leaky wave travels and loses energy because of radiation. The fields decay along the structure in the direction of the traveling wave and increase in others. Since the wave loses energy

as it propagates along a plane interface, (1.1) becomes,

$$(\beta_x - j\alpha_x)^2 + (\beta_z - j\alpha_z)^2 = k^2. \quad (1.3)$$

Equating imaginary parts,

$$\alpha_x\beta_x + \alpha_z\beta_z = 0, \quad (1.4)$$

where α_z and β_z are both positive (attenuation and phase constant in the direction of propagation); β_x is also positive (leakage away from the surface). Consequently, α_x must be negative. This means that the leaky-wave field increases away from the antenna's surface. Since the cross section outside the waveguide is unbounded, the leaky wave must increase transversely to infinite which is a violation of the radiation condition. Leaky waves are modal solutions that are improper mathematically because these waves increase in the transverse direction, in contrast to bound waves, which are proper and decrease transversely. As a result, the leaky wave must be mathematically improper, and it corresponds to a complex pole on the improper Riemann sheet of the longitudinal wave number plane. Practical leaky wave antennas are finite in extent. Therefore, leaky waves never reaches infinity. Hines *et al.* [4] made measurements and found that near the waveguide the field increases but some distance away it vanishes very rapidly. As it is shown on Figure 1.5, the field intensity decreases exponentially along z however following the dashed line in x direction the field increases vertically away. Thus this improper behavior happens only in the wedge-shape region.

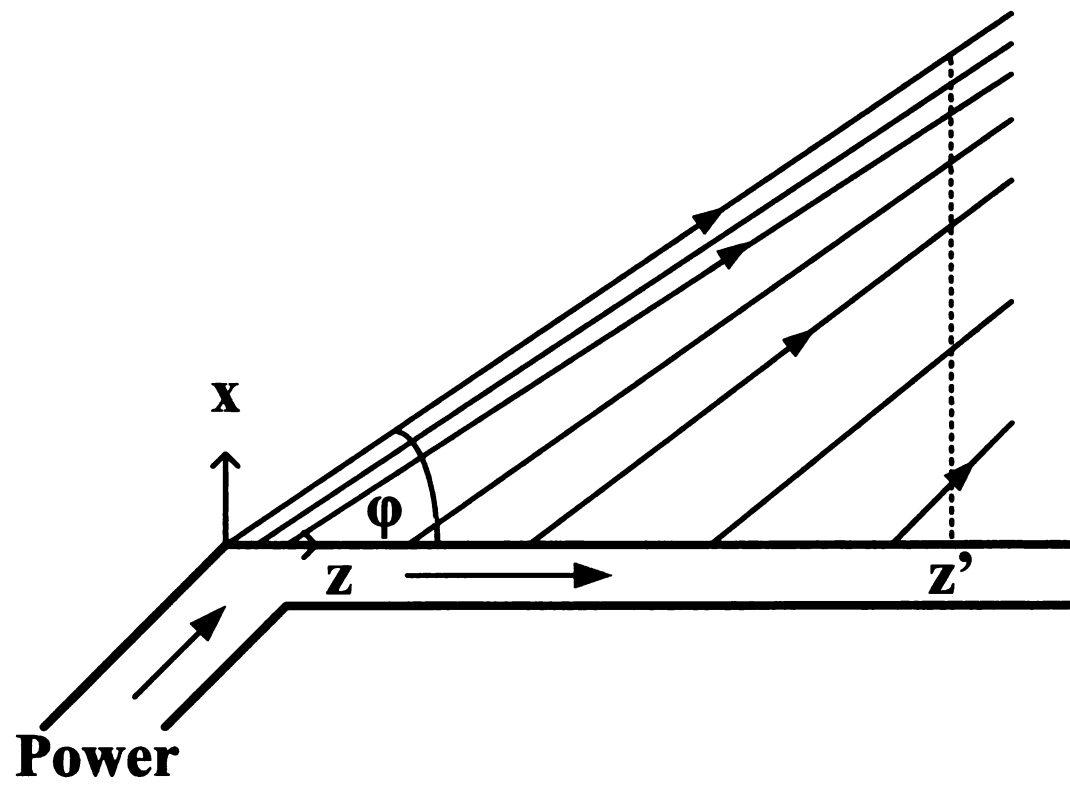


Figure 1.5. Leakage from a closed wave guide opened at the top (after [3]).

1.3 Operation modes of leaky-wave antennas

In the study of any leaky wave antenna, it is fundamental to know its complete propagation mode spectrum. If this mode spectrum is known, the total electromagnetic field of the antenna can be expanded in terms of its modes. The complete modal spectrum of this structure is composed of a continuum of orthogonal radiation modes and a finite number of discrete bound modes [23]. A bound mode does not radiate, which means that the electromagnetic fields are confined to the proximity of the guided region and no power flows transverse to the guide. An example of this mode is the EH_{00} mode for microstrip transmission lines. On the other hand, in radiation mode the electromagnetic fields are not confined to the guiding region and the power flows in the transverse region of the guide. In addition to those modes, a leaky wave mode is a discrete, not confined mode and its field distribution increases exponentially toward infinity. A leaky-wave mode is not part of the proper spectrum; rather it is used to construct the total field by the method of the steepest descent, which is an asymptotic technique but not a modal decomposition. Figure 1.6 shows the three frequency regions associated with the propagation regimes in a microstrip. The reactive, leaky, surface and bound regime. In the first regime, α_z is large causing the microstrip behaves as a reactive load. Above $f = f_c$ energy begins to propagate along the microstrip as β_z grows larger than α_z , the field losses energy due to radiation. The fields in the transverse section of the microstrip increases (Figure 1.5) because less energy leaks per unit length as the wave travels along the structure. Above the frequency at which $\beta_z/k_0 = 1$, α_x increases and the leaky wave starts to attenuate.

This region is known as the surface regime. Finally, the bound follows the surface regime and it is the recommended one for microstrip line operation because the fields are confined inside the transmission line.

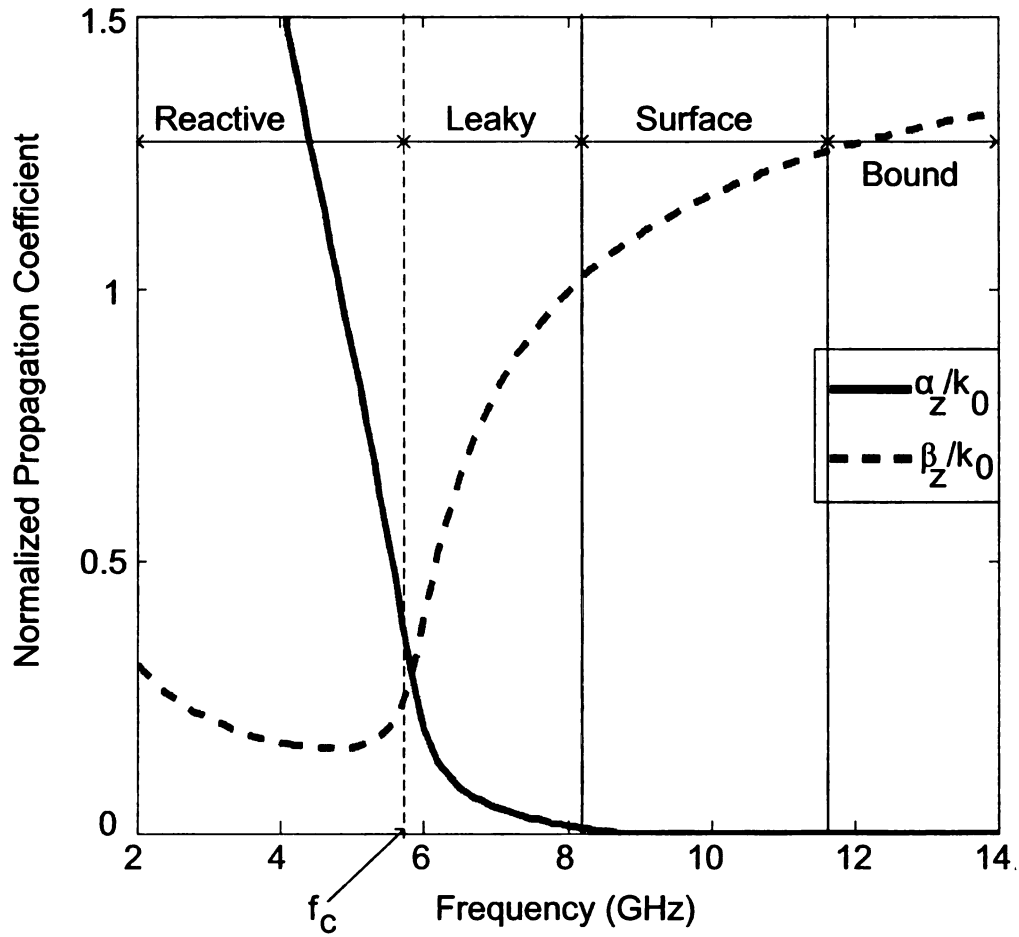


Figure 1.6. Typical dispersion characteristics of the hybrid leaky-wave EH_{10} mode (after [24]).

1.4 Radiation characteristics of a TLW antenna

It is very revealing to find the radiation pattern of the TLW antenna assuming that the aperture fields are traveling waves. The radiation field of the TLW antenna may be found by two different methods. The first uses the Fourier transform of the aperture field and the stationary phase method. The second method is using the equivalence principle and the vector potential. In this section, the second method is used. In order to solve for the radiation of the TLW antenna, it is assumed that the tangential components of the electric field over the aperture are known. The equivalent model [28] that will produce the same electric and magnetic fields radiated by the aperture is shown in Figure 1.7. For convenience, the TLW antenna shown on Figure 1.7 (a) is a 90° rotated version of Figure 1.4 in order to have the antenna's aperture on the $x - y$ plane. Figure 1.7 (c) corresponds to a magnetic current radiating in free space. If the equivalent currents are known, the vector magnetic potential may be found using

$$\vec{F}(\vec{r}) = \frac{\epsilon}{4\pi} \frac{e^{-jk r}}{r} \oint_{S'} \vec{M}(\vec{r}') e^{jk \hat{r} \cdot \vec{r}'} dS', \quad (1.5)$$

The magnetic current is given by

$$\vec{M} = -2\hat{z} \times \hat{y} E_0 e^{-jk_x x}. \quad (1.6)$$

Therefore, (1.5) becomes

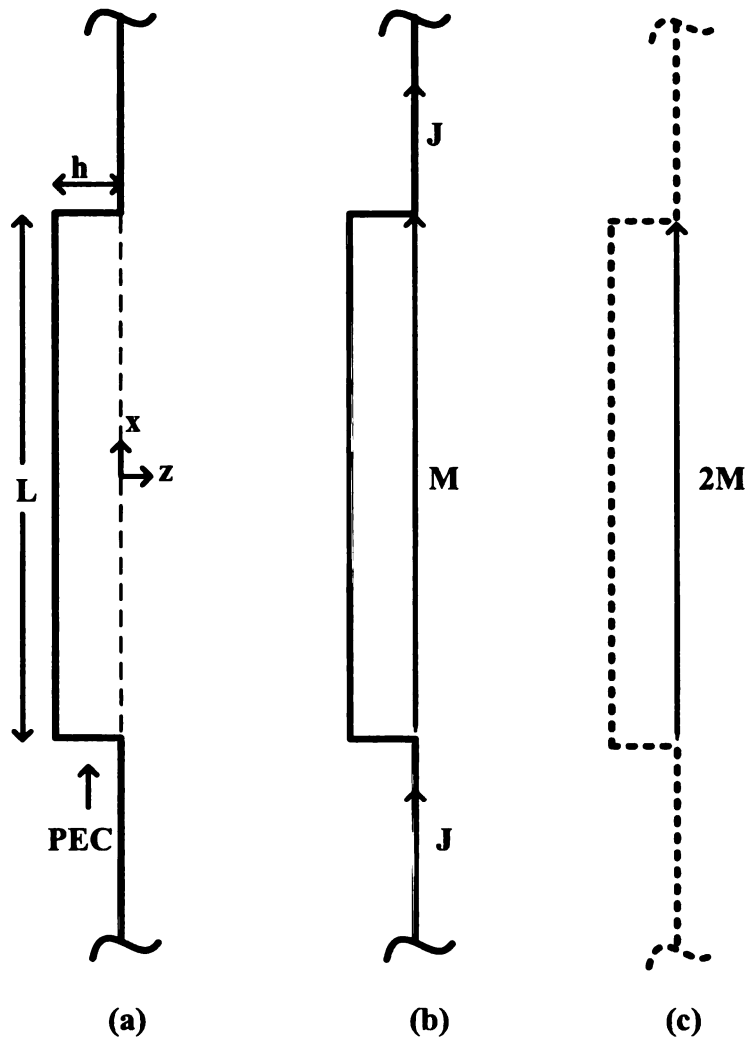


Figure 1.7. Equivalence models for the trough leaky wave antenna mounted on an infinite flat electric ground plane.

$$\vec{F}(\vec{r}) = \hat{x} \frac{\epsilon E_0 e^{-jkr}}{2\pi r} \oint_{S'} e^{-jk_x x} e^{jk \hat{r} \cdot \vec{r}'} dS', \quad (1.7)$$

where $\hat{r} = \hat{x} \sin \theta \cos \phi + \hat{y} \sin \theta \sin \phi + \hat{z} \cos \theta$, $\vec{r}' = x' \hat{x} + y' \hat{y}$, and the prime and unprime coordinates denote source and observation points respectively.

For the aperture shown on Figure 1.7, it is found that

$$\vec{F}(\vec{r}) = \hat{x} \frac{\epsilon E_0 e^{-jkr}}{2\pi r} \int_{-w/2}^{w/2} \int_{-L/2}^{L/2} e^{-j(k_x - k \sin \theta \cos \phi) x'} e^{-jk y' \sin \theta \sin \phi} dx' dy'. \quad (1.8)$$

After the integration over the aperture is performed, (1.8) becomes

$$\vec{F}(\vec{r}) = \hat{x} \frac{2\epsilon E_0 e^{-jkr}}{\pi r} \left\{ \frac{\sin [(k_x - k \sin \theta \cos \phi) L/2]}{(k_x - k \sin \theta \cos \phi)} \frac{\sin [kw/2 \sin \theta \sin \phi]}{k \sin \theta \sin \phi} \right\}. \quad (1.9)$$

The far-zone radiation field of an aperture antenna is given by [29]

$$\vec{E} \approx \frac{jk}{\epsilon} \hat{r} \times \vec{F}(\vec{r}) \quad (1.10)$$

Hence, the resulting θ and ϕ components of the electric field are given by

$$E_\theta = \frac{2jkE_0 e^{-jkr}}{\pi r} \left\{ \frac{\sin [(k_x - k \sin \theta \cos \phi) L/2]}{(k_x - k \sin \theta \cos \phi)} \frac{\sin [kw/2 \sin \theta \sin \phi]}{k \sin \theta \sin \phi} \right\} \sin \phi, \quad (1.11)$$

and

$$E_{\phi} = \frac{2jkE_0}{\pi} \frac{e^{-jkr}}{r} \left\{ \frac{\sin [(k_x - k \sin \theta \cos \phi) L/2]}{(k_x - k \sin \theta \cos \phi)} \frac{\sin [kw/2 \sin \theta \sin \phi]}{k \sin \theta \sin \phi} \right\} \cos \theta \cos \phi. \quad (1.12)$$

In the E-plane $\phi = \pi/2$, the θ component corresponds to a sinc function centered at $\theta = 0$. For this antenna this pattern is not of significant interest.

In the H-plane $\phi = 0$, (1.12) becomes

$$E_{\phi} = \frac{2jkE_0}{\pi} \frac{e^{-jkr}}{r} \left\{ \frac{\sin [(k_x - k \sin \theta) L/2]}{(k_x - k \sin \theta)} \right\} \cos \theta, \quad (1.13)$$

where $k_x = \beta_x - j\alpha_x$.

The radiation intensity in a given direction is defined as “the power radiated from an antenna per unit solid angle” [30]. The radiation intensity is related to the far-zone electric field of an antenna by [31]

$$U(\theta, \phi) = \frac{1}{2\eta} \left[|E_{\theta}(\theta, \phi)|^2 + |E_{\phi}(\theta, \phi)|^2 \right] \quad (1.14)$$

where η is the intrinsic impedance of the medium.

The normalized radiation pattern is found using

$$\begin{aligned}
U_{\theta}(\theta, \phi) &= \frac{|E_{\theta}(\theta, \phi)|^2}{\max\left[|E_{\theta}(\theta, \phi)|^2\right]}, \\
U_{\phi}(\theta, \phi) &= \frac{|E_{\phi}(\theta, \phi)|^2}{\max\left[|E_{\phi}(\theta, \phi)|^2\right]}.
\end{aligned} \tag{1.15}$$

Using the TRM, it is possible to compute k_x , (please see Chapter 2). The wavenumber k_x depends on frequency, antenna dimensions, and material inside the trough. As a function of frequency, the leaky wave antenna main lobe steers from broadside to endfire. The radiation pattern for TLW antenna is shown on Figure 1.8. This pattern corresponds to a single forward traveling wave. In reality, a finite length antenna has backward traveling waves that are reflected from the antenna termination.

In (1.13), the maximum of the radiation pattern occurs when $(k_x - k \sin \theta) = 0$, so that the angle of maximum radiation (θ_m) is determined to be

$$\frac{\beta_x}{k_0} \approx \sin \theta_m. \tag{1.16}$$

(1.16) is a fundamental relation in leaky-wave antennas [9].

Other fundamental relations in leaky wave antennas involve the effective aperture length (L) and the beamwidth ($\Delta\theta$). The effective aperture length of a leaky wave antenna is related to α_x . If α_x is small, the effective aperture length is large, since attenuation as the wave is guided along the length of the antenna is gradual. Accordingly, the far field radiation pattern has a narrow beamwidth and larger di-

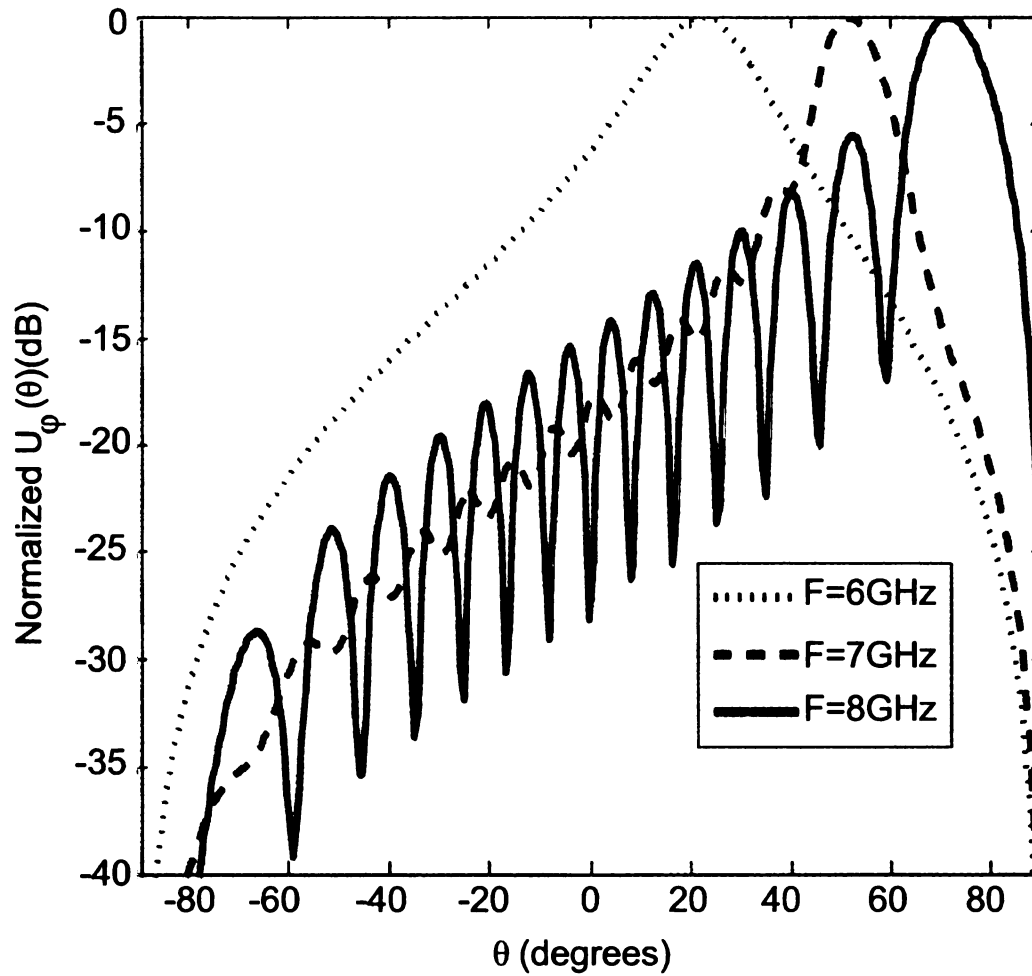


Figure 1.8. H-plane amplitude pattern for a forward traveling wave distribution aperture mounted on an infinite ground plane.

rectivity. On the other hand, if α_x is large, the effective aperture is short and the field radiation pattern has a wide beamwidth and consequently less directivity. The relationship between the antenna length (L) and the beamwidth is given by

$$\Delta\theta \approx \frac{\lambda_0}{L \cos \theta_m}. \quad (1.17)$$

The antenna length is usually selected for a given value of α_x such that

$$\frac{P(L)}{P(0)} = e^{[-4\pi(\alpha_x/k_0)(L/\lambda_0)]} \quad (1.18)$$

where $P(L)$ is the power remaining in the leaky mode at the antenna termination and $P(0)$ is the power input.

Therefore, the percentage of power radiated is given by

$$\% \text{Power radiated} = 100 \left[1 - e^{[-4\pi(\alpha_x/k_0)(L/\lambda_0)]} \right] \quad (1.19)$$

Most leaky wave antennas are designed to radiate 90% or more of the input power. The remaining 10% is absorbed by a matched load. For a 90% radiation power, the antenna length (1.19) becomes

$$\frac{L}{\lambda_0} \approx \frac{0.183k}{\alpha_x} \quad (1.20)$$

Since α_x is a function of frequency, the radiation efficiency changes as the beam is frequency scanned. This 90% criterion is usually applied to the middle of the operational bandwidth.

The characterization of the attenuation and phase coefficients allows for an effective design procedure. Note that these relations do not give sufficient information for determining either the feeding or termination requirements of the antenna; for this, full-wave methods are useful [17], [18], [19].

CHAPTER 2

ANALITICAL SOLUTION FOR THE TLW ANTENNA

2.1 Transverse resonance method

The TRM [21] allows rapid computation of the complex propagation constant that is fundamental for the analysis of leaky wave antennas; it was developed extensively by Lee [7]. In the TRM, the cross section of the TLW antenna (Figure 2.1 (a)) is represented as a transmission line (Figure 2.1 (b)) operating at resonance. The boundary conditions at the antenna's dielectric-air interface are

$$\left(\vec{E}^{ext} - \vec{E}^{int}\right)\Big|_{x=0} \times \hat{x} = 0, \quad (2.1)$$

$$\hat{x} \times \left(\vec{H}^{ext} - \vec{H}^{int}\right)\Big|_{x=0} = \vec{J}, \quad (2.2)$$

where \vec{E}^{ext} (\vec{H}^{ext}) and \vec{E}^{int} (\vec{H}^{int}) are the electric (magnetic) external and internal fields respectively.

Assuming a source free interface, a TRM relation is obtained from the continuity of the tangential components of the electric and magnetic field at $x = 0$. This is given by

$$E_y^{ext}(x = 0^+, y, z) = E_y^{int}(x = 0^-, y, z), \quad (2.3)$$

$$E_z^{ext}(x = 0^+, y, z) = E_z^{int}(x = 0^-, y, z), \quad (2.4)$$

$$H_y^{ext}(x = 0^+, y, z) = H_y^{int}(x = 0^-, y, z), \quad (2.5)$$

$$H_z^{ext}(x = 0^+, y, z) = H_z^{int}(x = 0^-, y, z). \quad (2.6)$$

The directional wave impedance is defined as the ratio between the electric field component and the corresponding orthogonal magnetic field component. The wave impedance in the positive x direction is

$$Z_x^+ = \frac{E_y^{ext}(x = 0, y, z)}{H_z^{ext}(x = 0, y, z)} = -\frac{E_z^{ext}(x = 0, y, z)}{H_y^{ext}(x = 0, y, z)}. \quad (2.7)$$

Similarly, the wave impedance in the negative x direction is written as

$$Z_x^- = -\frac{E_y^{int}(x = 0, y, z)}{H_z^{int}(x = 0, y, z)} = \frac{E_z^{int}(x = 0, y, z)}{H_y^{int}(x = 0, y, z)}. \quad (2.8)$$

Substituting (2.4) and (2.5) into (2.7) gives

$$Z_x^+ = -\frac{E_z^{int}(x = 0, y, z)}{H_y^{int}(x = 0, y, z)}. \quad (2.9)$$

The right hand side of (2.9) is equal to $-Z_x^-$ given by (2.8). Thus, the TRM relation is obtained

$$Z_x^+ + Z_x^- = 0. \quad (2.10)$$

It is customary to write (2.10) using the notation given in Figure 2.2

$$\overleftarrow{Z}(x) + \overrightarrow{Z}(x) = 0, \quad (2.11)$$

where the impedance looking to the left is denoted by $\overleftarrow{Z}(x)$ and the impedance looking to the right is denoted by $\overrightarrow{Z}(x)$. Note that in Figure 2.2, the shorting wall is explicitly shown and the transverse wavenumber k_x depends on the material inside the trough. Furthermore, the open edge impedance is unknown but assumed to be complex-valued. In Figure 2.2, h denotes the distance from the shorting wall. Equation 2.11 can be re-cast in terms of transverse reflection coefficients. The reflection coefficient looking to the left, $\overleftarrow{\Gamma}(x)$, (i.e., toward the shorting wall) is written as

$$\overleftarrow{\Gamma}(x) = \frac{\overleftarrow{Z}(x) - Z_0}{\overleftarrow{Z}(x) + Z_0}. \quad (2.12)$$

where Z_0 is the characteristic impedance of the equivalent transmission line.

Likewise, the reflection coefficient looking to the right, $\overrightarrow{\Gamma}(x)$, (i.e., toward the open edge of the antenna) is given by

$$\overrightarrow{\Gamma}(x) = \frac{\overrightarrow{Z}(x) - Z_0}{\overrightarrow{Z}(x) + Z_0}. \quad (2.13)$$

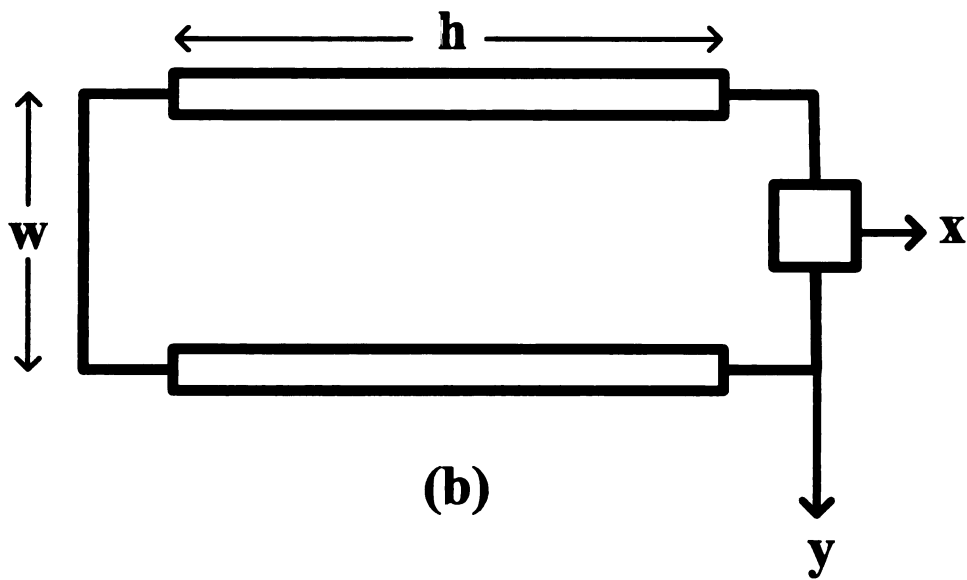
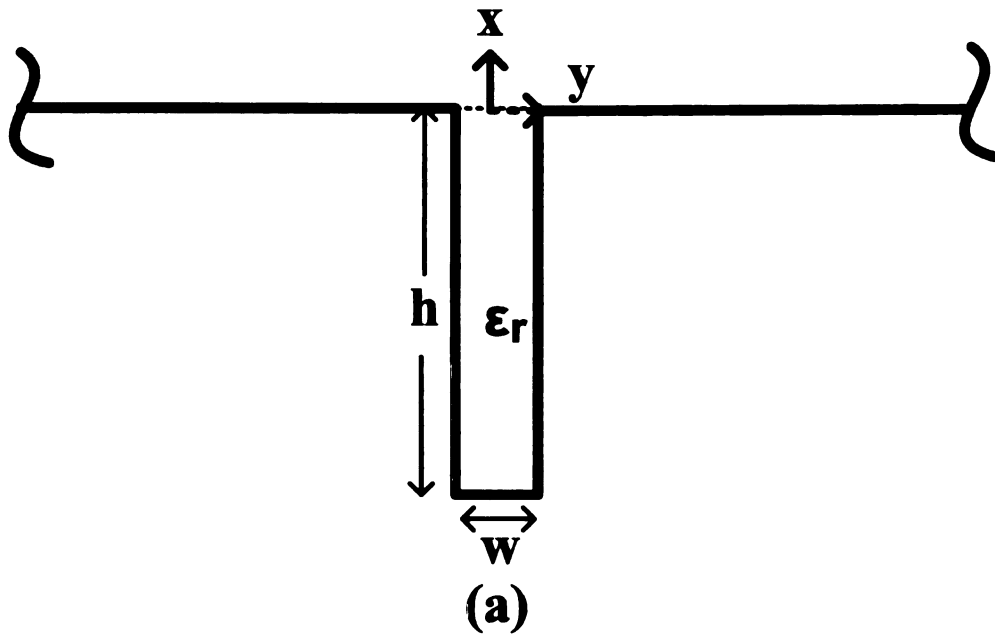


Figure 2.1. Transmission line model of the transverse cross-section of the TLW antenna.

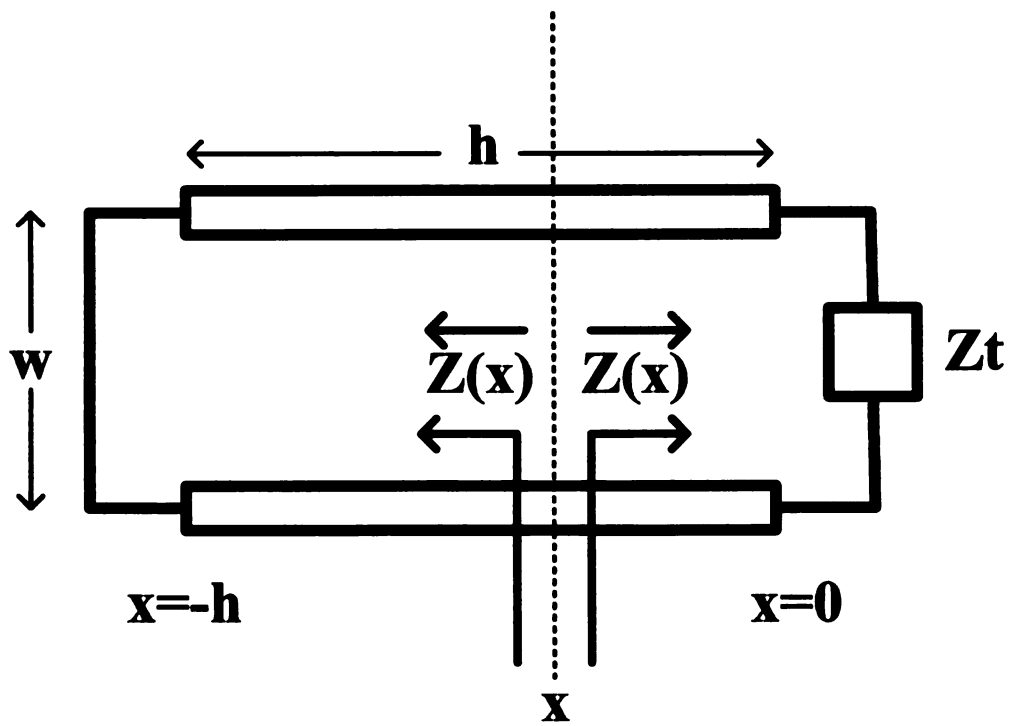


Figure 2.2. Transmission line used to illustrate the TRM.

Solving equations (2.12) and (2.13) for $\overleftarrow{Z}(x)$ and $\overrightarrow{Z}(x)$ respectively gives

$$\overleftarrow{Z}(x) = Z_0 \frac{1 + \overleftarrow{\Gamma}(x)}{1 - \overleftarrow{\Gamma}(x)}, \quad (2.14)$$

$$\overrightarrow{Z}(x) = Z_0 \frac{1 + \overrightarrow{\Gamma}(x)}{1 - \overrightarrow{\Gamma}(x)}. \quad (2.15)$$

Substituting (2.14) and (2.15) into (2.11) yields the desired TRM relation in terms of the reflection coefficients

$$\overleftarrow{\Gamma}(x) \cdot \overrightarrow{\Gamma}(x) = 1. \quad (2.16)$$

The unknown transverse impedance, Z_t , (Figure 2.2) is characterized by the reflection coefficient and the load to the left side as a short circuit. This reflection coefficient is calculated using the approximation for thin substrates provided in [32]. The reflection coefficient looking to the left at $x = -h$ is given by

$$\overleftarrow{\Gamma}(x = -h) = \frac{V^-(x = -h)}{V^+(x = -h)} = \frac{Z_L - Z_0}{Z_L + Z_0}. \quad (2.17)$$

where $Z_L = 0$ for a short circuited terminated line. Thus, $\overleftarrow{\Gamma}(x = -h) = -1$.

From the theory of traveling waves on lossless transmission lines (Figure 2.3), the voltage wave amplitudes at $x = -h$ are related to those at $x = 0$ by the expression

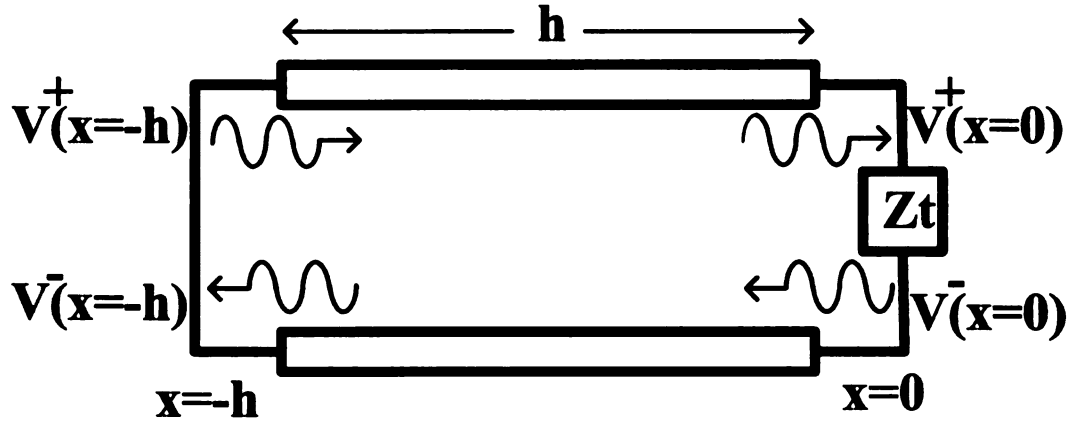


Figure 2.3. Shifting reference planes in the transmission line.

$$V^-(x = 0) = V^-(x = -h) e^{-jkxh}, \quad (2.18)$$

$$V^+(x = 0) = V^+(x = -h) e^{jkxh}. \quad (2.19)$$

The reflection coefficient looking to the left at $x = 0$ is defined by the expression

$$\overleftarrow{\Gamma}(x = 0) = \frac{V^-(x = 0)}{V^+(x = 0)}. \quad (2.20)$$

Therefore, dividing (2.18) by (2.19), and using (2.20) and (2.17), the desired reflection coefficient is obtained

$$\overleftarrow{\Gamma}(x=0) = -e^{-j2k_x h}. \quad (2.21)$$

According to [7], the reflection coefficient looking to the right is found by

$$\overrightarrow{\Gamma}(x=0) = e^{j\chi}, \quad (2.22)$$

where χ is a complex expression that incorporates the effect of the open radiating edge. It is given in [32].

Substituting (2.21) and (2.22) into (2.16), the following transcendental equation is obtained:

$$e^{-j2k_x h} e^{j\chi} = -1, \quad (2.23)$$

where, after recognizing $-1 = e^{\pm jn\pi}$, $n = 1, 3, 5, \dots$, (2.23) can be recast as

$$e^{-j2k_x h} e^{j\chi} = e^{\pm jn\pi}, n = 1, 3, 5... \quad (2.24)$$

The left-hand side of (2.24) is a complex value function in the form

$$w(z) = e^z \quad (2.25)$$

where z is a complex variable, $z = re^{j\theta} = x + jy$.

Since this function is single-valued [13], it is not necessary to consider any Riemann sheet. A further explanation of this is given on Appendix A.1. Therefore, the trascen-

dental equation becomes

$$\chi - 2k_x h = \pm n\pi, n = 1, 3, 5, \dots \quad (2.26)$$

For the hybrid leaky-wave EH_{10} mode shown in Figure 1.3, $n = 1$, and so (2.26) may be re-written as

$$\chi - 2k_x h + \pi = 0, \quad (2.27)$$

where χ is given on Appendix B.

The propagation constants inside and outside the trough are related by

$$k^2 = \epsilon_r k_0^2 = k_x^2 + k_z^2, \quad \text{for } x < 0, \quad (2.28)$$

$$k_0^2 = k_{0x}^2 + k_z^2, \quad k_0 = \omega \sqrt{\epsilon_0 \mu_0}, \quad \text{for } x > 0. \quad (2.29)$$

Therefore, the axial propagation constant k_z is related to the transverse propagation constant k_x by

$$k_z = \pm \sqrt{k_0^2 - k_x^2}. \quad (2.30)$$

The square root in (2.30) is a double-valued function (appendix A.2). The positive and negative signs correspond to two branch cuts. Only one of these branches is the correct to represent outgoing waves vanishing at infinity. The complex plane

representation of (2.30) is shown on Figure 2.4. Singular points occur along the real axis at the branch points $k_x = \pm k_0$.

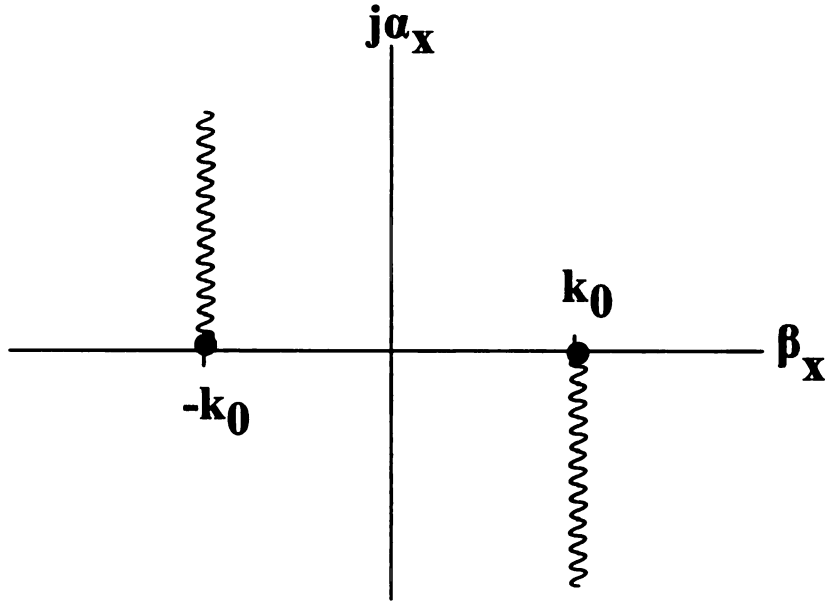


Figure 2.4. Complex plane representation of $k_z = \pm\sqrt{k_0^2 - k_x^2}$.

As an example, it is assumed a TLW antenna with $w = 0.0787\text{cm}$, $h = 0.75\text{cm}$ and $\epsilon_r = 2.33$. Using TRM the propagation constant is computed and shown on Figure 2.5. Same as microstrip leaky wave antennas [33], the operational band for TLW antennas is approximately defined from the frequencies in which $\alpha_z/k_0 = \beta_z/k_0$ and $\beta_z/k_0 = 1$. This regime is known as the leaky or fast region because the phase velocity is faster than the speed of light, i.e. $v_p > c$. This is the spectrum of interest

in leaky wave antennas design because it is favorable for radiation. The radiation takes place along the structure at some angle θ . The surface or slow wave region is located between $\beta_z/k_0 > 1$ and $\beta_z/k_0 < \sqrt{\epsilon_r}$. This region takes this name because $v_p < c$ and radiation may take place at discontinuities or at the termination of the structure.

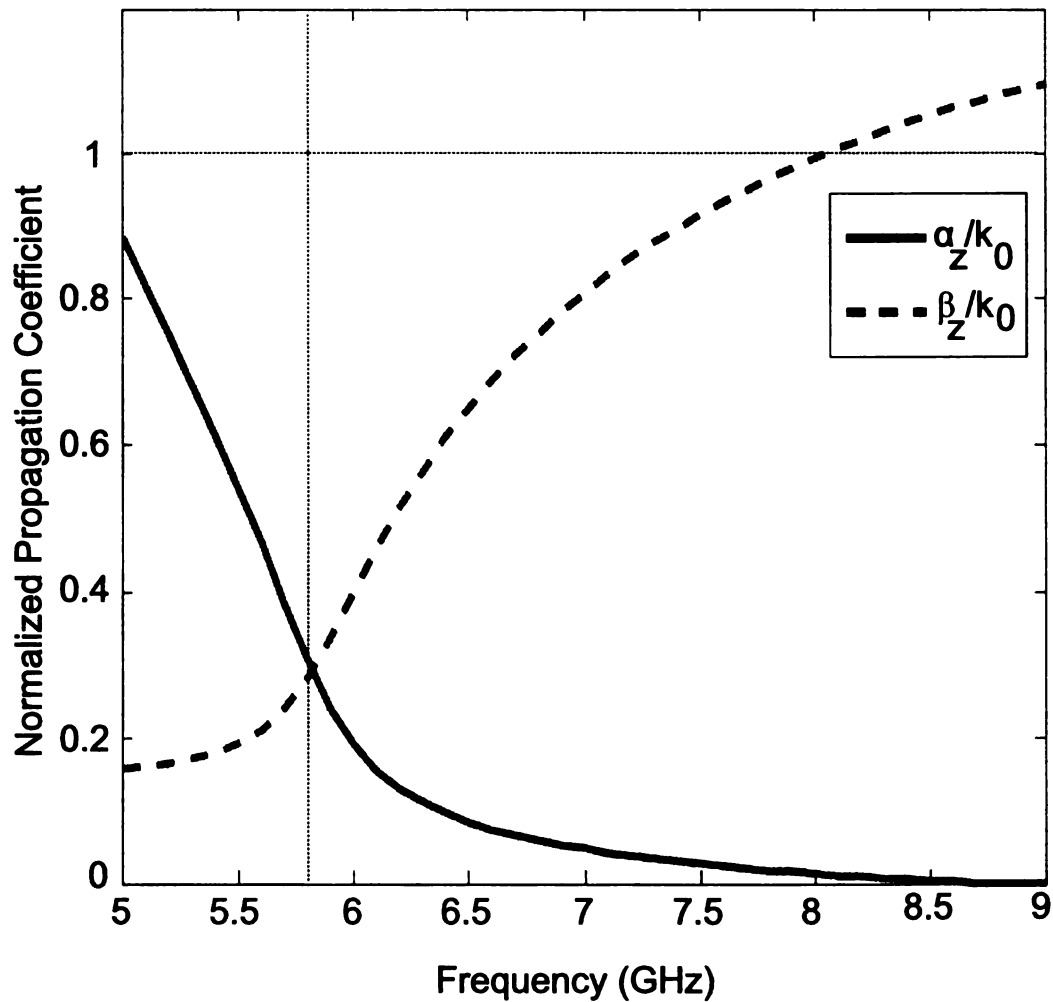


Figure 2.5. Propagation constant for a TLW antenna filled with RT/Duroid 5880.

One of the advantages of the TLW antenna with respect to microstrip leaky wave antennas is that it does not need a dielectric to support the conductor strip over the ground plane. Therefore, an appealing design is a TLW antenna filled with air. The parameters for this design are $w = 0.0787\text{cm}$, $h = 1\text{cm}$ and $\epsilon_r = 1.0$. Figure 2.6 shows a comparison of the propagation constants of the TLW antenna filled with RT/Duroid 5880 and that one filled with air. From these figure, it is clear that the operational band for the air-filled TLW antenna is much larger than the one for the RT/Duroid 5880-filled TLW antenna.

One disadvantage of the TRM is that it does not provide sufficient information for determining either the feeding or termination requirements of the antenna; the FE-BI method accounts for these important features [17].

2.2 TLW antenna driving point impedance

Knowing the propagation constant in a TLW antenna, it is possible to estimate its driving point impedance. The approach that is followed is similar to [34].

For the dielectric-filled TLW antenna shown on Figure 2.1(a), it is necessary to consider hybrid modes in order to satisfy boundary conditions between the interface of air and dielectric. However, it is possible to compute the driving point impedance for the first higher order mode using the mode $TM_{n=0}^y$.

The field components for the $TM_{n=0}^y$ mode are given by [35]

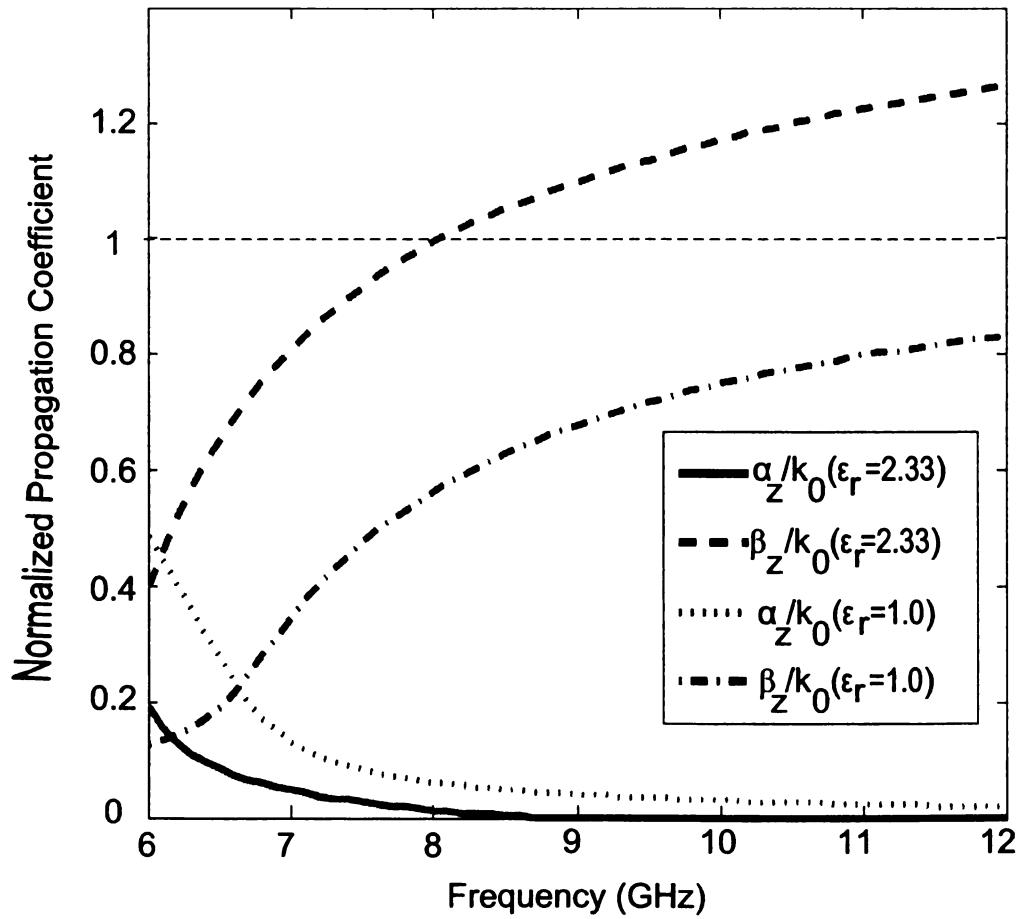


Figure 2.6. Propagation constants for a TLW antenna filled with RT/Duroid 5880 and a TLW antenna filled with air.

$$\begin{aligned}
E_x &= -j \frac{1}{\omega \mu \epsilon} \frac{\partial^2 \psi_y}{\partial x \partial y} & H_x &= -\frac{1}{\mu} \frac{\partial \psi_y}{\partial z} \\
E_y &= -j \frac{1}{\omega \mu \epsilon} \left(\frac{\partial_y^2}{\partial y^2} + k^2 \right) \psi_y & H_y &= 0 \\
E_z &= -j \frac{1}{\omega \mu \epsilon} \frac{\partial^2 \psi_y}{\partial y \partial z} & H_z &= \frac{1}{\mu} \frac{\partial \psi_y}{\partial x},
\end{aligned} \tag{2.31}$$

where the scalar potential function ψ_y has the form

$$\psi_y = C \sin [k_x (x + h)] (\cos k_y y) e^{-j k_z z} \tag{2.32}$$

where C is a constant.

In order to satisfy boundary conditions at $y = \pm w/2$ and at $x = -h$ (Figure 2.1(a)),

$k_y = 2\pi n/w$. For the first higher order mode $n = 0$, hence (2.32) becomes

$$\psi_y = C \sin [k_x (x + h)] e^{-j k_z z}. \tag{2.33}$$

Thus according to (2.31), the field component E_y and H_x are

$$E_y = -j \frac{1}{\omega \mu \epsilon} k^2 C \sin [k_x (x + h)] e^{-j k_z z}, \tag{2.34}$$

and

$$H_x = jk_z C \sin [k_x (x + h)] e^{-jk_z z}. \quad (2.35)$$

In Figure 2.1(a), the voltage between the parallel plates at $y = -1/2$ and $y = 1/2$ is given by

$$V = - \int_{-w/2}^{w/2} E_y dy = \frac{wjk^2 C}{\omega\mu\epsilon} \sin [k_x (x + h)] e^{-jk_z z}. \quad (2.36)$$

It can be assumed a current density \vec{J}_s flowing in the plate located at $y = 1/2$, the electric current has the form

$$I = \int_{-h}^0 \vec{J}_s \cdot \hat{z} dx, \quad (2.37)$$

but $\vec{J}_s = -\hat{y} \times \vec{H}$, hence (2.37) becomes

$$I = \int_{-h}^0 H_x dx. \quad (2.38)$$

Substituting (2.35) into (2.38) and performing the integral, it is found that

$$I = \frac{jk_z C}{\mu k_x} (1 - \cos k_x h) e^{-jk_z z}. \quad (2.39)$$

Using Ohm's law, (2.36), and (2.39), the first higher order mode driving point **impedance** of the infinitely long TLW antenna is given by

$$Z_{dp} = \frac{wk_x k^2 \sin [k_x (x + h)]}{\omega\epsilon k_z (1 - \cos k_x h)}. \quad (2.40)$$

In order to assess the effectiveness of this method, the driving point impedance is computed using (2.40). The input parameters are: $w = 0.0787\text{cm}$, $h = 0.75\text{cm}$, and $\epsilon_r = 2.33$. The wave number k_z is computed using TRM and k_x is obtained from the relation $k_x = \sqrt{k^2 - k_z^2}$, where $k = k_0 = \omega\sqrt{\mu_0\epsilon_0}$. The driving point impedance result is shown on Figure 2.7 and its corresponding VSWR assuming a 50Ω termination, is shown on Figure 2.8. In addition, the same computations are performed for the air-filled TLW antenna ($w = 0.0787\text{cm}$, $h = 1.0\text{cm}$, and $\epsilon_r = 1.0$). These results are shown in Figure 2.9 and Figure 2.10, respectively.

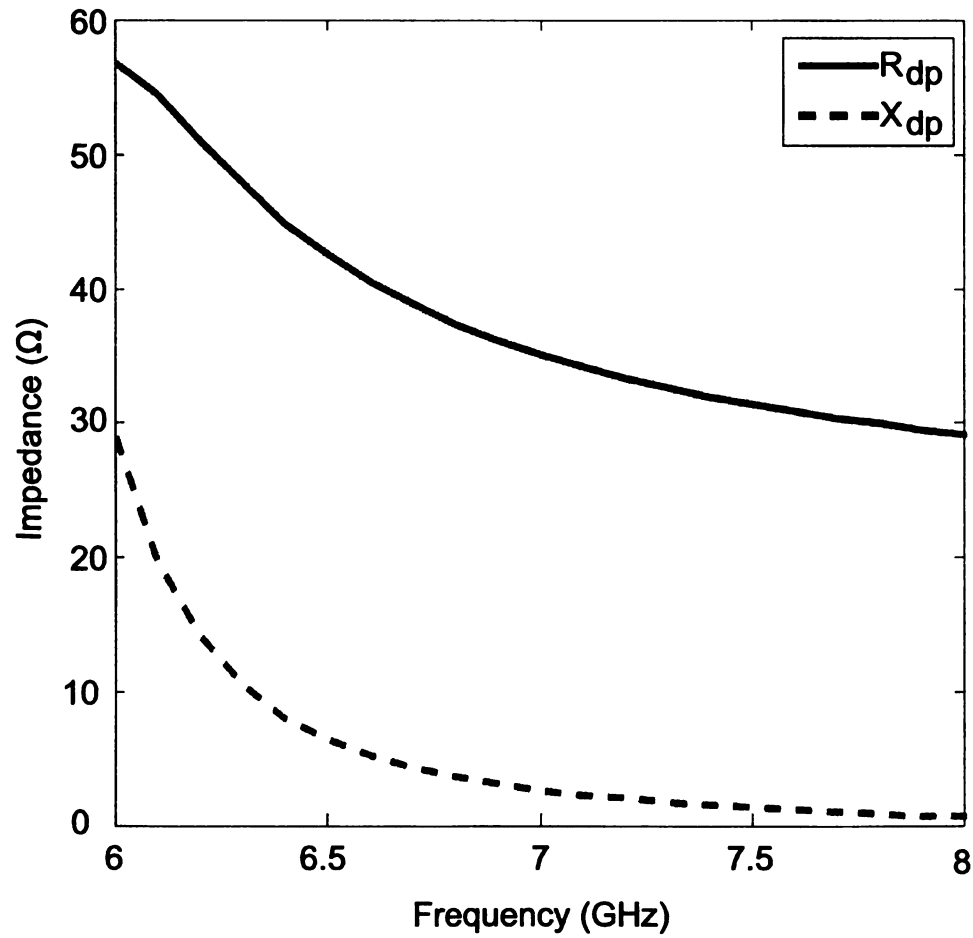


Figure 2.7. Real and imaginary part of the driving point impedance for an infinitely long TLW antenna (RT/Duroid 5880-filled).

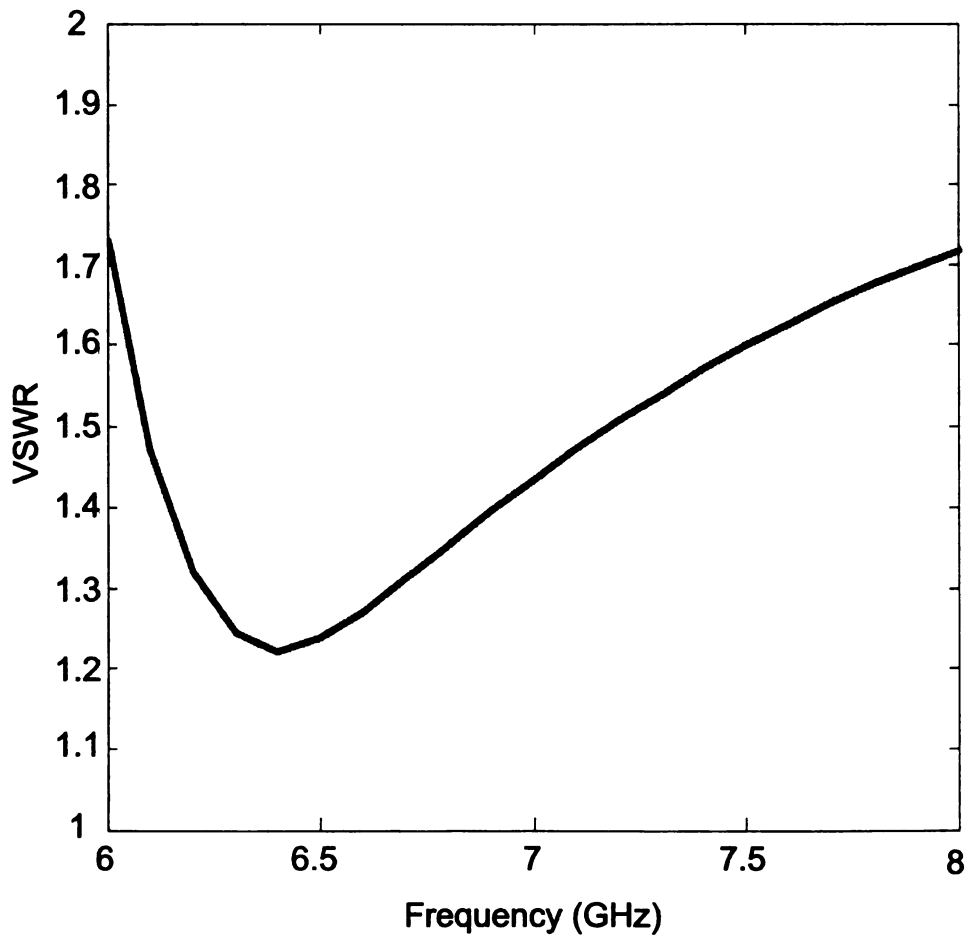


Figure 2.8. VSWR for an infinitely long TLW antenna (RT/Duroid 5880-filled).

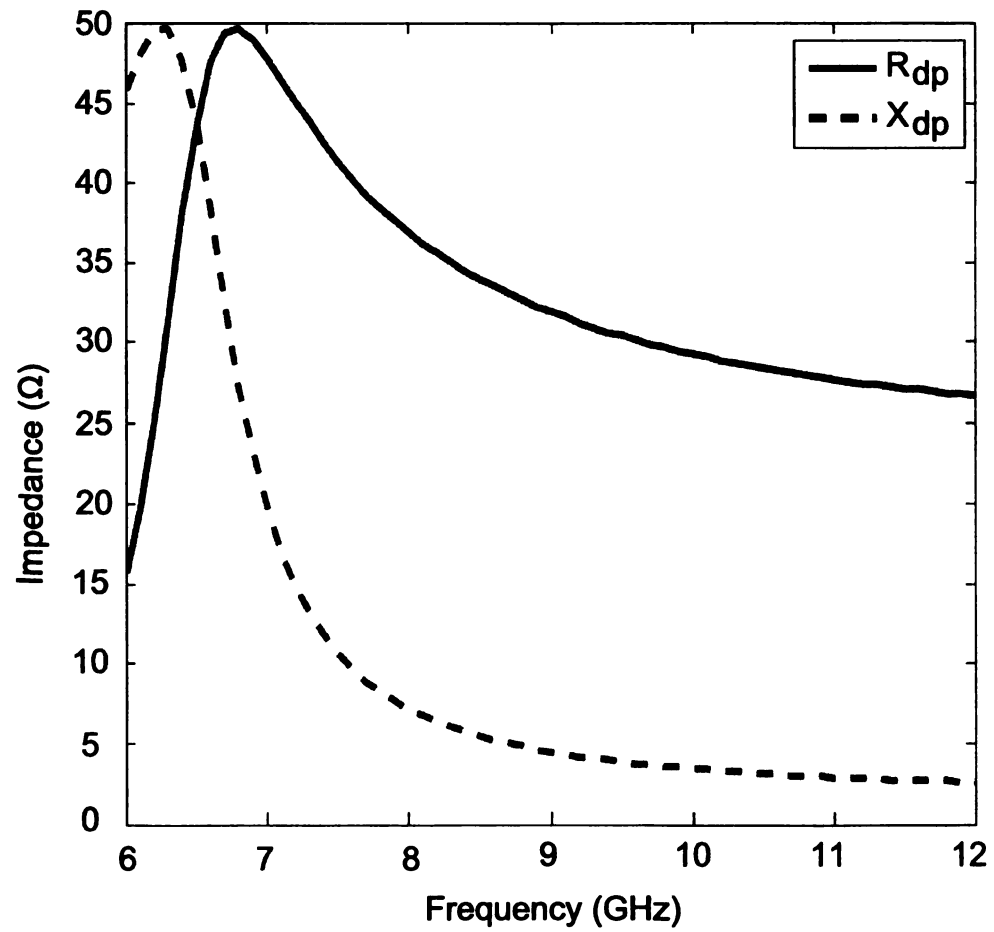


Figure 2.9. Real and imaginary part of the driving point impedance for an infinitely long TLW antenna (air-filled).

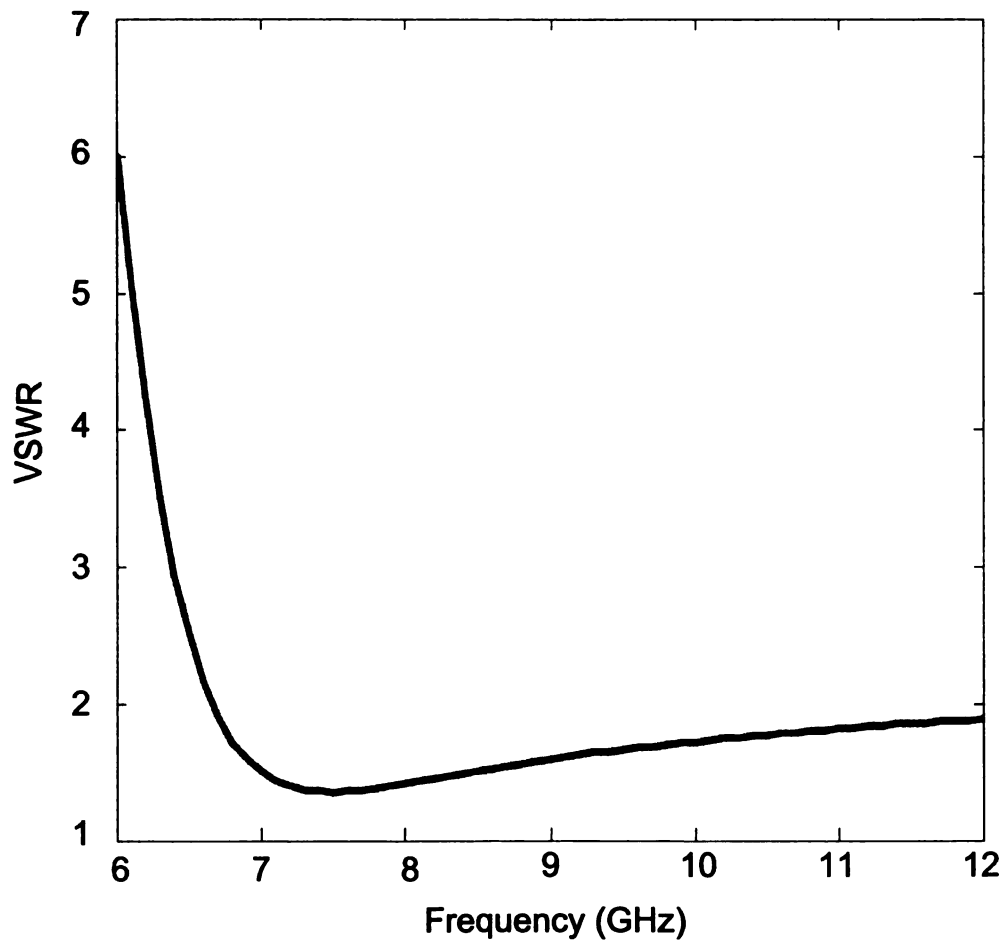


Figure 2.10. VSWR for an infinitely long TLW antenna (air-filled).

CHAPTER 3

NUMERICAL SOLUTION FOR THE TLW ANTENNA

3.1 Finite element boundary integral method

The finite element-boundary integral (FE-BI) method combines the finite element and boundary integral formulations in a hybrid technique that uses the best features of the finite element method (geometric and material flexibility) and a boundary integral (minimal extent mesh closure condition). This hybrid technique is very attractive for modeling three-dimensional cavity backed apertures if the aperture lies in a metallic **plane** since the order of the resulting linear system is minimal. In this work, the cavity **is** discretized using tetrahedral elements and the aperture of the cavity is discretized **using** triangular elements such that the tetrahedral faces lying in the aperture are **congruent** with the triangles, thus ensuring proper continuity of fields from the interior **to** exterior regions. The general geometry is illustrated in Figure 3.1, it is assumed **for this** work that the cavity is filled with a homogeneous material having a relative **permittivity** ϵ_r and a relative permeability μ_r . In general, the FE-BI method can **readily** accommodate inhomogeneous cavity filling materials. The FE-BI method in **electromagnetics** has been around 30+ years and considered in many books (e.g, [17], [22], etc.).

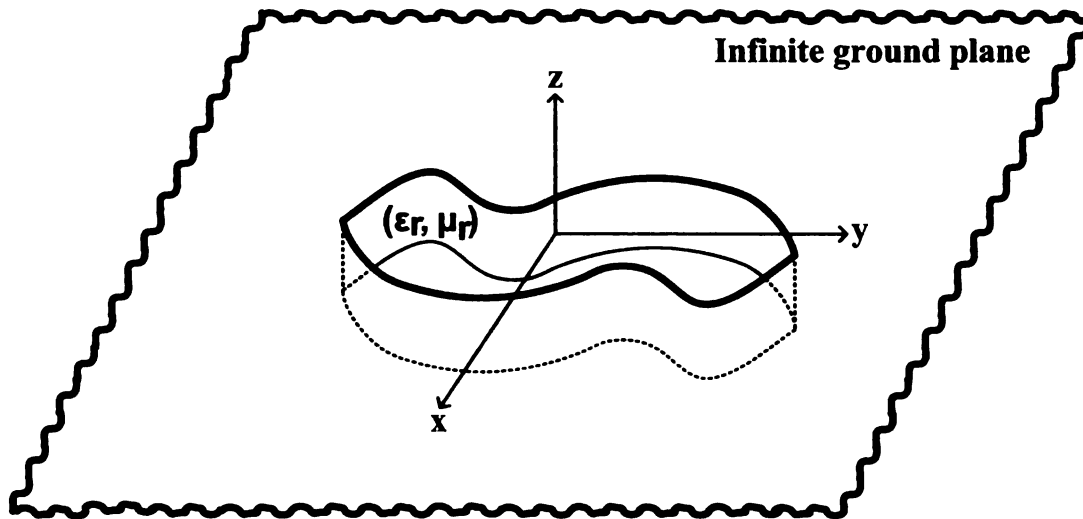


Figure 3.1. Geometry of a three-dimensional cavity-backed aperture in an infinite ground plane.

3.2 Finite element formulation

The fields \vec{E}^{int} and \vec{H}^{int} in the interior of the cavity shown on Figure 3.1 obey Maxwell equations

$$\nabla \times \vec{H}^{int} = j\omega\epsilon\vec{E}^{int} + \vec{J} \quad (3.1)$$

$$\nabla \times \vec{E}^{int} = -j\omega\mu\vec{H}^{int}. \quad (3.2)$$

Equations (3.1) and (3.2) are the well-known Ampère-Maxwell's law and Faraday's law, respectively. ϵ is the absolute permittivity, μ the absolute permeability inside the cavity, and \vec{J} is an excitation within the cavity. These two equations may be combined

together to yield a single second-order vector equation in terms of the electric field. The advantage of using the electric field over the magnetic field formulation is that the boundary conditions on a perfect electric conductor surface are easily satisfied as will be shown later in this chapter. The FE-BI method is used to numerically approximate the solution of the vector wave equation, in particular a linear system of equations is obtained via Galerkin's method. Taking the curl of (3.2) and using (3.1), the following vector wave equation is obtained

$$\nabla \times \nabla \times \vec{E}^{int} - \omega^2 \mu \epsilon \vec{E}^{int} = -j\omega \mu \vec{J} \quad (3.3)$$

Equation (3.3) is usually expressed in a more convenient form using the relation between the absolute and relative properties of the material, this is

$$\epsilon_r = \frac{\epsilon}{\epsilon_0} \quad (3.4)$$

where $\epsilon_0 = 8.854 \times 10^{-12}$ farad per meter,

$$\mu_r = \frac{\mu}{\mu_0} \quad (3.5)$$

where $\mu_0 = 4\pi \times 10^{-7}$ henry per meter.

Therefore, the vector wave equation (3.3) becomes

$$\frac{1}{\mu_r} \nabla \times \nabla \times \vec{E}^{int} - k_0^2 \epsilon_r \vec{E}^{int} = -jk_0 Z_0 \vec{J}, \quad (3.6)$$

where $k_0 = \omega \sqrt{\mu_0 \epsilon_0}$ is the free-space wave number, $Z_0 = \sqrt{\mu_0 / \epsilon_0}$ is the intrinsic

impedance of free-space, and ε_r and μ_r are the relative permittivity and permeability respectively inside the cavity.

A weighted residual [17] is formed taking an inner product between the vector wave equation (3.6) and a vector subdomain basis function (\vec{W}_i) . The objective is to minimize the difference between the approximated solution and the physical reality.

The inner product [17] over the domain Ω of two vector functions is defined as

$$\langle \vec{a}, \vec{b} \rangle = \int_{\Omega} \vec{a} \cdot \vec{b} d\Omega \quad (3.7)$$

where Ω denotes a volume, surface or contour.

Taking the inner product of (3.6) and a vector subdomain basis function, \vec{W}_i , an integro-differential equation is obtained.

$$\frac{1}{\mu_r} \int_V \vec{W}_i \cdot \{ \nabla \times \nabla \times \vec{E}^{int} - k_0^2 \varepsilon_r \vec{E}^{int} \} dV = -jk_0 Z_0 \int_V \vec{W}_i \cdot \vec{J} dV \quad (3.8)$$

where V denotes the volume of the cavity on Figure 3.1.

The right hand side of (3.8) corresponds to the interior excitation sources and can be expressed as

$$f_i^{int} = -jk_0 Z_0 \int_V \vec{W}_i \cdot \vec{J} dV. \quad (3.9)$$

Substituting (3.9) into (3.8), the electric formulation becomes

$$\frac{1}{\mu_r} \int_V \vec{W}_i \cdot \left\{ \nabla \times \nabla \times \vec{E}^{int} - k_0^2 \epsilon_r \vec{E}^{int} \right\} dV = f_i^{int}. \quad (3.10)$$

Equation (3.10) contains second-order derivatives of the unknown electric field. To realize a symmetric operator –in the spirit of reciprocity– one of the derivatives is transferred from the unknown electric field onto the vector basis function using the first vector Green’s Theorem [36]

$$\int_V \left[(\nabla \times \vec{F}_1) \cdot (\nabla \times \vec{F}_2) - \vec{F}_1 \cdot \nabla \times \nabla \times \vec{F}_2 \right] dV = \oint_S \hat{n} \cdot (\vec{F}_1 \times \nabla \times \vec{F}_2) dS. \quad (3.11)$$

Using (3.11) into (3.10), the FE-BI equation becomes,

$$\begin{aligned} & \frac{1}{\mu_r} \int_V \left\{ (\nabla \times \vec{W}_i) \cdot (\nabla \times \vec{E}^{int}) \right\} dV \\ & - k_0^2 \epsilon_r \int_V \left\{ \vec{W}_i \cdot \vec{E}^{int} \right\} dV \\ & - \frac{1}{\mu_r} \oint_S \left\{ \hat{n} \cdot (\vec{W}_i \times \nabla \times \vec{E}^{int}) \right\} dS = f_i^{int} \end{aligned} \quad (3.12)$$

where S is the closed contour bounding the volume V .

The cross product between the normal vector and the magnetic field is necessary to enforce boundary conditions. The electric field \vec{E}^{int} is related to \vec{H}^{int} by Faraday's law. Substituting (3.2) into (3.12), the functional becomes

$$\begin{aligned}
& \frac{1}{\mu_r} \int_V \left\{ (\nabla \times \vec{W}_i) \cdot (\nabla \times \vec{E}^{int}) \right\} dV \\
& - k_0^2 \epsilon_r \int_V \left\{ \vec{W}_i \cdot \vec{E}^{int} \right\} dV \\
& + j k_0 Z_0 \oint_S \left\{ \hat{n} \cdot (\vec{W}_i \times \vec{H}^{int}) \right\} dS = f_i^{int}.
\end{aligned} \tag{3.13}$$

Using the vector identity

$$\vec{A} \cdot \vec{B} \times \vec{C} = -\vec{B} \cdot \vec{A} \times \vec{C}, \tag{3.14}$$

(3.13) can be written as

$$\begin{aligned}
& \frac{1}{\mu_r} \int_V \left\{ (\nabla \times \vec{W}_i) \cdot (\nabla \times \vec{E}^{int}) \right\} dV \\
& - k_0^2 \epsilon_r \int_V \left\{ \vec{W}_i \cdot \vec{E}^{int} \right\} dV \\
& - j k_0 Z_0 \oint_S \left\{ \vec{W}_i \cdot (\hat{n} \times \vec{H}^{int}) \right\} dS = f_i^{int}.
\end{aligned} \tag{3.15}$$

Equation (3.15) is known as the weak form of the wave equation. One important characteristic of this equation is that the electric field and the testing function have the same number of derivatives, if Galerkin's method is used, a symmetric linear system of equations is obtained for isotropic materials.

3.3 Boundary integral formulation

For the exterior region ($z > 0$ in Figure 3.1), the external fields \vec{E} and \vec{H} also obey Maxwell's equations

$$\nabla \times \vec{H}^{ext}(\vec{r}) = j\omega\epsilon_0 \vec{E}^{ext}(\vec{r}) + \vec{J}^{ext}(\vec{r}) \quad (3.16)$$

$$\nabla \times \vec{E}^{ext}(\vec{r}) = -j\omega\mu_0 \vec{H}^{ext}(\vec{r}). \quad (3.17)$$

Taking the curl of (3.16) and using (3.17), a vector wave equation in terms of the magnetic field is obtained:

$$\nabla \times \nabla \times \vec{H}^{ext}(\vec{r}) - k_0^2 \vec{H}^{ext}(\vec{r}) = \nabla \times \vec{J}^{ext}(\vec{r}). \quad (3.18)$$

In order to find the radiated field, the dyadic Green function $\overline{\overline{G}}_e$ is used [36]. $\overline{\overline{G}}_e$ is a solution of the dyadic differential equation

$$\nabla \times \nabla \times \overline{\overline{G}}_e(\vec{r}, \vec{r}') - k_0^2 \overline{\overline{G}}_e(\vec{r}, \vec{r}') = \overline{\overline{I}} \delta(\vec{r} - \vec{r}'), \quad (3.19)$$

where

$$\bar{\bar{I}} = \hat{x}\hat{x} + \hat{y}\hat{y} + \hat{z}\hat{z} \quad (3.20)$$

is the Idem factor and $\delta(\vec{r} - \vec{r}')$ denotes the Dirac delta function.

In order to find the integral solution for (3.18) the second vector-dyadic Green's theorem is used:

$$\begin{aligned} \int_V \left[\vec{P} \cdot \nabla \times \nabla \times \bar{\bar{Q}} - (\nabla \times \nabla \times \vec{P}) \cdot \bar{\bar{Q}} \right] dV = \\ - \oint_S \hat{n} \cdot \left[\vec{P} \times \nabla \times \bar{\bar{Q}} + (\nabla \times \vec{P}) \times \bar{\bar{Q}} \right] dS, \end{aligned} \quad (3.21)$$

letting $\vec{P} = \vec{H}^{ext}(\vec{r})$ and $\bar{\bar{Q}} = \bar{\bar{G}}_e(\vec{r}, \vec{r}')$ on (3.21) yields the expression

$$\begin{aligned} \int_V \left\{ \left[\vec{H}^{ext}(\vec{r}) \cdot \nabla \times \nabla \times \bar{\bar{G}}_e(\vec{r}, \vec{r}') - (\nabla \times \nabla \times \vec{H}^{ext}(\vec{r})) \cdot \bar{\bar{G}}_e(\vec{r}, \vec{r}') \right] \right\} dV = \\ - \oint_S \left\{ \hat{n} \cdot \left[\vec{H}^{ext}(\vec{r}) \times \nabla \times \bar{\bar{G}}_e(\vec{r}, \vec{r}') + (\nabla \times \vec{H}^{ext}(\vec{r})) \times \bar{\bar{G}}_e(\vec{r}, \vec{r}') \right] \right\} dS. \end{aligned} \quad (3.22)$$

Substituting the double curl terms $\nabla \times \nabla \times \bar{\bar{G}}_e$ and $\nabla \times \nabla \times \vec{H}^{ext}$ from (3.19) and (3.18) into (3.22), the above equation can be converted to

$$\begin{aligned}
& \int_V \left\{ \vec{H}^{ext}(\vec{r}) \cdot \left[k_0^2 \vec{G}_e(\vec{r}, \vec{r}') + \vec{I} \delta(\vec{r} - \vec{r}') \right] - \right. \\
& \left. \left[k_0^2 \vec{H}^{ext}(\vec{r}) + \nabla \times \vec{J}^{ext}(\vec{r}) \right] \cdot \vec{G}_e(\vec{r}, \vec{r}') \right\} dV = \\
& - \oint_S \hat{n} \cdot \left\{ \vec{H}^{ext}(\vec{r}) \times \nabla \times \vec{G}_e(\vec{r}, \vec{r}') + \right. \\
& \left. \left(\nabla \times \vec{H}^{ext}(\vec{r}) \right) \times \vec{G}_e(\vec{r}, \vec{r}') \right\} dS. \tag{3.23}
\end{aligned}$$

The terms multiplying k_0^2 in the volume integral of (3.23) cancel each other, and

$$\int_V \left\{ \vec{H}^{ext}(\vec{r}) \cdot \vec{I} \delta(\vec{r} - \vec{r}') \right\} dV = \int_V \left\{ \vec{H}^{ext}(\vec{r}) \delta(\vec{r} - \vec{r}') \right\} dV = \vec{H}^{ext}(\vec{r}') \tag{3.24}$$

thus,

$$\begin{aligned}
\vec{H}^{ext}(\vec{r}') - \int_V \left\{ \left[\nabla \times \vec{J}^{ext}(\vec{r}) \right] \cdot \overline{\overline{G}}_e(\vec{r}, \vec{r}') \right\} dV = \\
- \oint_S \hat{n} \cdot \left\{ \vec{H}^{ext}(\vec{r}) \times \nabla \times \overline{\overline{G}}_e(\vec{r}, \vec{r}') + \right. \\
\left. \left(\nabla \times \vec{H}^{ext}(\vec{r}) \right) \times \overline{\overline{G}}_e(\vec{r}, \vec{r}') \right\} dS. \tag{3.25}
\end{aligned}$$

Using the dyadic identity

$$\vec{a} \cdot (\vec{b} \times \vec{c}) = \vec{b} \cdot (\vec{a} \times \vec{c}) = (\vec{a} \times \vec{b}) \cdot \vec{c}, \tag{3.26}$$

on the surface integral of (3.25), this whole expression becomes

$$\begin{aligned}
\vec{H}^{ext}(\vec{r}') - \int_V \left\{ \left[\nabla \times \vec{J}^{ext}(\vec{r}) \right] \cdot \overline{\overline{G}}_e(\vec{r}, \vec{r}') \right\} dV = \\
- \oint_S \left\{ \vec{H}^{ext}(\vec{r}) \cdot \left[\hat{n} \times \nabla \times \overline{\overline{G}}_e(\vec{r}, \vec{r}') \right] + \right. \\
\left. \left[\hat{n} \times \nabla \times \vec{H}^{ext}(\vec{r}) \right] \cdot \overline{\overline{G}}_e(\vec{r}, \vec{r}') \right\} dS. \tag{3.27}
\end{aligned}$$

The volume integral of (3.27) can be split in two terms applying the dyadic identity

$$\nabla \cdot (\vec{a} \times \vec{b}) = (\nabla \times \vec{a}) \cdot \vec{b} - \vec{a} \cdot \nabla \times \vec{b} \quad (3.28)$$

this is,

$$\int_V \left\{ \left[\nabla \times \vec{J}^{ext}(\vec{r}) \right] \cdot \vec{G}_e(\vec{r}, \vec{r}') \right\} dV =$$

$$\int_V \left\{ \nabla \cdot \left[\vec{J}^{ext}(\vec{r}) \times \vec{G}_e(\vec{r}, \vec{r}') \right] + \vec{J}^{ext}(\vec{r}) \cdot \nabla \times \vec{G}_e(\vec{r}, \vec{r}') \right\} dV. \quad (3.29)$$

The dyadic divergence theorem and (3.26) are applied to the first volume integral in the right hand side of (3.29) to obtain the following expression:

$$\int_V \left\{ \nabla \cdot \left[\vec{J}^{ext}(\vec{r}) \times \vec{G}_e(\vec{r}, \vec{r}') \right] \right\} dV =$$

$$\int_S \left\{ \hat{n} \cdot \left[\vec{J}^{ext}(\vec{r}) \times \vec{G}_e(\vec{r}, \vec{r}') \right] \right\} dS =$$

$$\int_S \left\{ \left[\hat{n} \times \vec{J}^{ext}(\vec{r}) \right] \cdot \vec{G}_e(\vec{r}, \vec{r}') \right\} dS. \quad (3.30)$$

Substituting (3.30) into (3.29) yields the expression

$$\begin{aligned}
& \int_V \left\{ \left[\nabla \times \bar{J}^{ext}(\vec{r}) \right] \cdot \bar{G}_e(\vec{r}, \vec{r}') \right\} dV = \\
& \int_S \left\{ \left[\hat{n} \times \bar{J}^{ext}(\vec{r}) \right] \cdot \bar{G}_e(\vec{r}, \vec{r}') \right\} dS + \\
& \int_V \left\{ \bar{J}^{ext}(\vec{r}) \cdot \nabla \times \bar{G}_e(\vec{r}, \vec{r}') \right\} dV. \tag{3.31}
\end{aligned}$$

In view of (3.31), the integral equation of (3.27) becomes

$$\begin{aligned}
\bar{H}^{ext}(\vec{r}') - \int_V \left\{ \bar{J}^{ext}(\vec{r}) \cdot \nabla \times \bar{G}_e(\vec{r}, \vec{r}') \right\} dV = \\
- \oint_S \left\{ \bar{H}^{ext}(\vec{r}) \cdot \left[\hat{n} \times \nabla \times \bar{G}_e(\vec{r}, \vec{r}') \right] \right. \\
\left. - \left[\hat{n} \times \bar{J}^{ext}(\vec{r}) \right] \cdot \bar{G}_e(\vec{r}, \vec{r}') \right. \\
\left. + \left[\hat{n} \times \nabla \times \bar{H}^{ext}(\vec{r}) \right] \cdot \bar{G}_e(\vec{r}, \vec{r}') \right\} dS. \tag{3.32}
\end{aligned}$$

Collecting terms on the right hand side of equation (3.32), this can be written as

$$\begin{aligned}
\vec{H}^{ext}(\vec{r}') - \int_V \left\{ \vec{J}^{ext}(\vec{r}) \cdot \nabla \times \vec{G}_e(\vec{r}, \vec{r}') \right\} dV = \\
- \oint_S \left\{ \vec{H}^{ext}(\vec{r}) \cdot \left[\hat{n} \times \nabla \times \vec{G}_e(\vec{r}, \vec{r}') \right] \right. \\
\left. - \hat{n} \times \left[\vec{J}^{ext}(\vec{r}) - \nabla \times \vec{H}^{ext}(\vec{r}) \right] \cdot \vec{G}_e(\vec{r}, \vec{r}') \right\} dS. \tag{3.33}
\end{aligned}$$

In view of the Ampère-Maxwell's law (3.1), the above equation can be written in the form

$$\begin{aligned}
\vec{H}^{ext}(\vec{r}') - \int_V \left\{ \vec{J}^{ext}(\vec{r}) \cdot \nabla \times \vec{G}_e(\vec{r}, \vec{r}') \right\} dV = \\
- \oint_S \left\{ \vec{H}^{ext}(\vec{r}) \cdot \left[\hat{n} \times \nabla \times \vec{G}_e(\vec{r}, \vec{r}') \right] \right. \\
\left. + j\omega\epsilon_0 \left[\hat{n} \times \vec{E}^{ext}(\vec{r}) \right] \cdot \vec{G}_e(\vec{r}, \vec{r}') \right\} dS. \tag{3.34}
\end{aligned}$$

For the cavity-backed aperture case (Figure 3.1) the volume V is bounded interiorly by the entire xy -plane and exteriorly by a hemispherical surface S_∞ at infinity. If $\vec{H}^{ext}(\vec{r})$ satisfies the radiation condition, this is,

$$\lim_{\vec{r} \rightarrow \infty} \vec{r} \left[\nabla \times \vec{H}^{ext}(\vec{r}) + jk_0 \vec{r} \times \vec{H}^{ext}(\vec{r}) \right] = 0, \quad (3.35)$$

and if $\overline{\overline{G}}_e$ is chosen to satisfy the same condition, the portion of the surface integral over the hemispherical is equal to zero; only the contribution from xy -plane needs to be considered. Therefore, equation (3.34) can be written as

$$\begin{aligned} \vec{H}^{ext}(\vec{r}') - \int_V \left\{ \vec{j}^{ext}(\vec{r}) \cdot \nabla \times \overline{\overline{G}}_e(\vec{r}, \vec{r}') \right\} dV = \\ - \int_{xy\text{-plane}} \left\{ \vec{H}^{ext}(\vec{r}) \cdot \left[\hat{n} \times \nabla \times \overline{\overline{G}}_e(\vec{r}, \vec{r}') \right] \right. \\ \left. + j\omega\epsilon_0 \left[\hat{n} \times \vec{E}^{ext}(\vec{r}) \right] \cdot \overline{\overline{G}}_e(\vec{r}, \vec{r}') \right\} dS. \end{aligned} \quad (3.36)$$

The tangential electric field $\hat{n} \times \vec{E}^{ext}(\vec{r})$ vanishes at the ground plane except at the cavity aperture. In addition, $\overline{\overline{G}}_e$ is chosen to satisfy the dyadic Neumann boundary condition on the xy -plane; namely,

$$\hat{n} \times \nabla \times \overline{\overline{G}}_{e2} = 0 \quad (3.37)$$

where $\overline{\overline{G}}_{e2}$ is the electric dyadic Green function of the second kind. Therefore, (3.36) reduces to

$$\begin{aligned} \vec{H}^{ext}(\vec{r}') - \int_V \left\{ \vec{J}^{ext}(\vec{r}) \cdot \nabla \times \overline{\overline{G}}_{e2}(\vec{r}, \vec{r}') \right\} dV = \\ -j\omega\epsilon_0 \int_{S_a} \left\{ \left[\hat{n} \times \vec{E}^{ext}(\vec{r}) \right] \cdot \overline{\overline{G}}_{e2}(\vec{r}, \vec{r}') \right\} dS. \end{aligned} \quad (3.38)$$

It is convenient to cast (3.38) in the standard form using \vec{r} as the position vector for a field point and \vec{r}' as that for a point inside a source. Interchanging the primed and unprimed coordinate systems, the integral expression (3.38) becomes

$$\begin{aligned} \vec{H}^{ext}(\vec{r}) = \int_V \left\{ \vec{J}^{ext}(\vec{r}') \cdot \nabla' \times \overline{\overline{G}}_{e2}(\vec{r}', \vec{r}) \right\} dV' \\ -j\omega\epsilon_0 \int_{S_a} \left\{ \left[\hat{n}' \times \vec{E}^{ext}(\vec{r}') \right] \cdot \overline{\overline{G}}_{e2}(\vec{r}', \vec{r}) \right\} dS'. \end{aligned} \quad (3.39)$$

In view of the dyadic identity

$$\vec{a} \cdot \overline{\overline{b}} = \left(\overline{\overline{b}} \right)^T \cdot \vec{a}, \quad (3.40)$$

where $\left(\overline{\overline{b}} \right)^T$ is the transpose of the dyadic $\overline{\overline{b}}$; the integral equation (3.39) becomes

$$\begin{aligned} \vec{H}^{ext}(\vec{r}) &= \int_V \left\{ \left[\nabla' \times \overline{\overline{G}}_{e2}(\vec{r}', \vec{r}) \right]^T \cdot \vec{J}^{ext}(\vec{r}') \right\} dV' \\ &\quad - j\omega\epsilon_0 \int_{S_a} \left\{ \left[\overline{\overline{G}}_{e2}(\vec{r}', \vec{r}) \right]^T \cdot \left[\hat{n}' \times \vec{E}^{ext}(\vec{r}') \right] \right\} dS'. \end{aligned} \quad (3.41)$$

In addition, using the symmetrical relationships of the dyadic Green functions [36]; namely,

$$\left[\nabla' \times \overline{\overline{G}}_{e2}(\vec{r}', \vec{r}) \right]^T = \nabla \times \overline{\overline{G}}_{e1}(\vec{r}, \vec{r}'), \quad (3.42)$$

$$\left[\overline{\overline{G}}_{e2}(\vec{r}', \vec{r}) \right]^T = \overline{\overline{G}}_{e2}(\vec{r}, \vec{r}'), \quad (3.43)$$

the integral equation (3.41) can be written in the form

$$\begin{aligned} \vec{H}^{ext}(\vec{r}) &= \int_V \left\{ \left[\nabla \times \overline{\overline{G}}_{e1}(\vec{r}, \vec{r}') \right] \cdot \vec{J}^{ext}(\vec{r}') \right\} dV' \\ &\quad - j\omega\epsilon_0 \int_{S_a} \left\{ \overline{\overline{G}}_{e2}(\vec{r}, \vec{r}') \cdot \left[\hat{n}' \times \vec{E}^{ext}(\vec{r}') \right] \right\} dS' \end{aligned} \quad (3.44)$$

The dyadic electric Green function of first kind $\left(\overline{\overline{G}}_{e1} \right)$ is given by

$$\bar{\bar{G}}_{e1}(\vec{r}, \vec{r}') = \bar{\bar{G}}_{e0}(\vec{r}, \vec{r}') - \bar{\bar{G}}_{e0}(\vec{r}, \vec{r}_i') + 2\hat{z}\hat{z}G_0(\vec{r}, \vec{r}_i') \quad (3.45)$$

where

$$\bar{\bar{G}}_{e0}(\vec{r}, \vec{r}') = \left(\bar{\bar{I}} - \frac{\nabla\nabla'}{k_0^2} \right) G_0(\vec{r}, \vec{r}'), \quad (3.46)$$

$$G_0(\vec{r}, \vec{r}') = \frac{e^{-jk_0|\vec{r}-\vec{r}'|}}{4\pi|\vec{r}-\vec{r}'|}, \quad (3.47)$$

and $\vec{r}_i' = x'\hat{x} + y'\hat{y} - z'\hat{z}$ is the image position of $\vec{r}' = x'\hat{x} + y'\hat{y} + z'\hat{z}$.

Equation (3.45) is known as the half-space electric dyadic Green function of the first kind and satisfies (3.19), the radiation condition (3.35), and the Neumann boundary condition (3.37).

Substituting (3.45) into (3.44) yields

$$\begin{aligned} \vec{H}^{ext}(\vec{r}) = & \int_V \left\{ \left[\nabla \times \bar{\bar{G}}_{e0}(\vec{r}, \vec{r}') \right] \cdot \vec{J}^{ext}(\vec{r}') \right\} dV' \\ & - \int_V \left\{ \left[\nabla \times \left(\bar{\bar{G}}_{e0}(\vec{r}, \vec{r}_i') - 2\hat{z}\hat{z}G_0(\vec{r}, \vec{r}_i') \right) \right] \cdot \vec{J}^{ext}(\vec{r}') \right\} dV' \\ & - j\omega\epsilon_0 \int_{S_a} \left\{ \bar{\bar{G}}_{e2}(\vec{r}, \vec{r}') \cdot \left[\hat{n}' \times \vec{E}^{ext}(\vec{r}') \right] \right\} dS'. \end{aligned} \quad (3.48)$$

The first integral on the right hand side of (3.48) is the field radiated by $\vec{J}^{ext}(\vec{r}')$

in free space, this field is denoted as \vec{H}^{inc} . The second integral is the field reflected on the ground plane and it is denoted as \vec{H}^{ref} . These two fields are known and are maintained by $\vec{J}(\vec{r}')$. The third integral is the secondary field radiated by the aperture, it is denoted as \vec{H}^{sec} and needs to be determined. Therefore, equation (3.48) can be written as

$$\vec{H}^{ext} = \vec{H}^{inc} + \vec{H}^{ref} + \vec{H}^{sec}. \quad (3.49)$$

For radiation problems, $\vec{H}^{inc} = 0$ and therefore $\vec{H}^{ref} = 0$; however these fields are retained in this analysis for completeness sake.

Since the intrinsic admittance of free space is given by $Y_0 = \sqrt{\epsilon_0/\mu_0}$, it is convenient to write the secondary field as

$$\vec{H}^{sec} = -jk_0 Y_0 \int_{S_a} \left\{ \overline{\overline{G}}_{e2}(\vec{r}, \vec{r}') \cdot [\hat{n}' \times \vec{E}^{ext}(\vec{r}')] \right\} dS'. \quad (3.50)$$

The Green function $\left(\overline{\overline{G}}_{e2}\right)$ evaluated on the plane of the conductor is twice the free space Green function

$$\overline{\overline{G}}_{e2}(\vec{r}, \vec{r}') = - \left(\overline{\overline{I}} + \frac{\nabla\nabla}{k_0^2} \right) \left[\frac{e^{-jk_0 R}}{2\pi R} \right] \quad (3.51)$$

where $R = |\vec{r} - \vec{r}'|$.

Letting z to approach to zero and taking the tangential component of (3.49) the desired magnetic field integral equation is obtained

$$\hat{n} \times \vec{H}^{ext}(\vec{r}) = \left[\hat{n} \times \vec{H}^{inc} + \hat{n} \times \vec{H}^{ref} \right]$$

$$-jk_0 Y_0 \int_{S_a} \left\{ \left[\hat{n} \times \overline{\overline{G}}_{e2}(\vec{r}, \vec{r}') \right] \cdot \left[\hat{n}' \times \vec{E}^{ext}(\vec{r}') \right] \right\} dS'. \quad (3.52)$$

Using (3.26) the argument on the surface integral of equation (3.52) can be rewritten as

$$\hat{n} \times \vec{H}^{ext}(\vec{r}) = \left[\hat{n} \times \vec{H}^{inc} + \hat{n} \times \vec{H}^{ref} \right]$$

$$-jk_0 Y_0 \int_{S_a} \left\{ \left[\hat{n} \times \overline{\overline{G}}_{e2}(\vec{r}, \vec{r}') \right] \times \hat{n}' \cdot \vec{E}^{ext}(\vec{r}') \right\} dS'. \quad (3.53)$$

With the idea of relating the tangential components of the external magnetic field and the internal magnetic field the inner product between (3.53) and \vec{W}_i is carried out.

$$\begin{aligned}
& \int_{S_a} \left\{ \vec{W}_i \cdot \left[\hat{n} \times \vec{H}^{ext}(\vec{r}) \right] \right\} dS = \\
& \int_{S_a} \left\{ \vec{W}_i \cdot \left[\hat{n} \times \vec{H}^{inc} + \hat{n} \times \vec{H}^{ref} \right] \right\} dS \\
& -jk_0 Y_0 \int \int_{S_a} \left\{ \vec{W}_i \cdot \left[\hat{n} \times \overline{\overline{G}}_{e2}(\vec{r}, \vec{r}') \times \hat{n}' \right] \cdot \vec{E}^{ext}(\vec{r}') \right\} dS' dS. \quad (3.54)
\end{aligned}$$

The exterior excitation field is composed by \vec{H}^{inc} and \vec{H}^{ref} this is,

$$f_i^{ext} = \int_{S_a} \left\{ \vec{W}_i \cdot \left[\hat{n} \times \vec{H}^{inc} + \hat{n} \times \vec{H}^{ref} \right] \right\} dS. \quad (3.55)$$

Replacing (3.55) in (3.54), the boundary integral expression becomes

$$\begin{aligned}
& \int_{S_a} \left\{ \vec{W}_i \cdot \left[\hat{n} \times \vec{H}^{ext}(\vec{r}) \right] \right\} dS + \\
& jk_0 Y_0 \int \int_{S_a} \left\{ \vec{W}_i \cdot \left[\hat{n} \times \overline{\overline{G}}_{e2}(\vec{r}, \vec{r}') \times \hat{n}' \right] \cdot \vec{E}^{ext}(\vec{r}') \right\} dS' dS = f_i^{ext}. \quad (3.56)
\end{aligned}$$

The boundary conditions at the aperture of the cavity, this is at $z = 0$, are given by

$$\hat{z} \times \left(\vec{H}^{ext} - \vec{H}^{int} \right)_{z=0} = 0, \quad (3.57)$$

$$\hat{z} \times \left(\vec{E}^{ext} - \vec{E}^{int} \right)_{z=0} = 0. \quad (3.58)$$

In order to couple (3.15) and (3.56) the continuity condition of the tangential component of the magnetic field (3.57) is enforced at the aperture; hence the FE-BI equation takes the form

$$\begin{aligned} & \frac{1}{\mu_r} \int_V \left\{ \left(\nabla \times \vec{W}_i \right) \cdot \left(\nabla \times \vec{E}^{int} \right) \right\} dV \\ & - k_0^2 \epsilon_r \int_V \left\{ \vec{W}_i \cdot \vec{E}^{int} \right\} dV \\ & - k_0^2 \int \int_{S_a} \left\{ \vec{W}_i \cdot \left[\hat{n} \times \overline{\overline{G}}_{e2} \left(\vec{r}, \vec{r}' \right) \times \hat{n}' \right] \cdot \vec{E}^{ext} \left(\vec{r}' \right) \right\} dS' dS \\ & = f_i^{int} + j k_0 Z_0 f_i^{ext}. \end{aligned} \quad (3.59)$$

In order to enforce the continuity condition of the tangential component of the electric field (3.58), the interior and exterior electric fields are expanded with the same subdomain-vector-basis function this is,

$$\vec{E}^{int} = \vec{E}^{ext} = \sum_{j=1}^N E_j \vec{W}_j, \quad (3.60)$$

where N is the total number of edge-unknowns in the element.

In this procedure, Galerkin's method is utilized, this is, the expansion basis function (\vec{W}_j) are the same as the testing basis function (\vec{W}_i).

When the field expansion (3.60) is substituted into (3.59) elemental matrix is obtained

$$\begin{aligned}
& \sum_{j=1}^N E_j \left\{ \frac{1}{\mu_r} \int_V \{ (\nabla \times \vec{W}_i) \cdot (\nabla \times \vec{W}_j) \} dV \right. \\
& \qquad \qquad \qquad \left. - k_0^2 \epsilon_r \int_V \{ \vec{W}_i \cdot \vec{W}_j \} dV \right\} \\
& - \sum_{j=1}^N E_j \left\{ k_0^2 \int \int_{S_a} \{ \vec{W}_i \cdot (\hat{z} \times \overline{\overline{G}}_{e2} \times \hat{z}') \cdot \vec{W}_j \} dS' dS \right\} \\
& \qquad \qquad \qquad = f_i^{int} + jk_0 Z_0 f_i^{ext}. \qquad (3.61)
\end{aligned}$$

Assuming that the cavity is discretized using tetrahedrons, and the tetrahedron's edges follow a global numeration; a linear system of equations can be obtained from (3.61). This linear system of equations is summarized in a matrix-vector notation given by

$$[\mathbf{A}] \{\mathbf{E}\} = \{\mathbf{b}\}, \qquad (3.62)$$

where $\{\mathbf{E}\}$ is the unknown coefficient vector, $\{\mathbf{b}\}$ is the excitation vector, and $[\mathbf{A}]$ is a matrix which is composed of two parts:

$$[\mathbf{A}] = \begin{bmatrix} A_{bb}^{FE} & A_{bi}^{FE} \\ A_{ib}^{FE} & A_{ii}^{FE} \end{bmatrix} + \begin{bmatrix} A_{bb}^{BI} & 0 \\ 0 & 0 \end{bmatrix} \quad (3.63)$$

The first submatrix is the finite element (FE) portion and its entries are given by

$$A_{i,j}^{FE} = \frac{1}{\mu r} \int_V \left\{ (\nabla \times \vec{W}_i) \cdot (\nabla \times \vec{W}_j) \right\} dV - k_0^2 \epsilon_r \int_V \left\{ \vec{W}_i \cdot \vec{W}_j \right\} dV, \quad (3.64)$$

and the second is the boundary integral (BI) submatrix with the generic term

$$A_{i,j}^{BI} = -k_0^2 \int \int_{S_a} \left\{ \vec{W}_i \cdot \left(\hat{z} \times \overline{\overline{G}}_{e2} \times \hat{z}' \right) \cdot \vec{W}_j \right\} dS' dS. \quad (3.65)$$

3.4 Antenna feed and load

In order to compute the antenna input impedance and radiation pattern, it is assumed that there is not any external source. Therefore, f_i^{ext} in (3.61) is equal to zero. In addition, assuming an infinitesimally thin current filament in the \hat{y} direction for this work, f_i^{int} (3.9) becomes

$$f_i^{int} = -jk_0 Z_0 I_0 l_i, \quad (3.66)$$

where l_i is the length of the edge where the feed is located.

In a similar way, an impedance load of $Z_L [\Omega]$ can be modeled as an infinitely thin pin. Assuming a pin of length l and coincident with the i th edge, the conductivity must be $\sigma = l/Z_L$ but $\vec{J} = \sigma \vec{E}$; therefore, the load contribution to the global matrix

\mathbf{A} is given by [22]

$$a_{i,i} = \frac{jk_0 Z_0 l_i}{Z_L} \iint \{ \vec{W}_i \cdot \vec{W}_i \} dx dy = \frac{jk_0 Z_0 l_i^2}{Z_L}. \quad (3.67)$$

Notice that (3.67) contributes to the main diagonal of the matrix at the location of the unknown associated with the load position.

3.5 FE matrix entries using tetrahedrons

Tetrahedrons have the versatility to conform to many shapes. In addition, their corresponding vector basis functions satisfies the divergence-free condition which is sufficient to avoid fictitious charge within the element. The convention for the local node and edge numbering for each tetrahedron in this dissertation is shown in Figure 3.2.

Each of the six edges is represented by a vector basis function that has the form [17]

$$\vec{W}_i = (L_{i1} \nabla L_{i2} - L_{i2} \nabla L_{i1}) l_i, \quad (3.68)$$

where l_i is the length of edge i , ($i = 1, 2, \dots, 6$), and L_{i1} and L_{i2} are the scalar-basis functions of nodes 1 and 2 associated to edge i . L_{i1} is defined as

$$L_{i1} = \frac{1}{6Ve} (a_{i1}^e + b_{i1}^e x + c_{i1}^e y + d_{i1}^e z). \quad (3.69)$$

L_{i2} has a similar expression to (3.69). The gradient of the node-basis function L_{i1} , is constant and normal to edge i . The vector-basis function \vec{W}_i has important properties

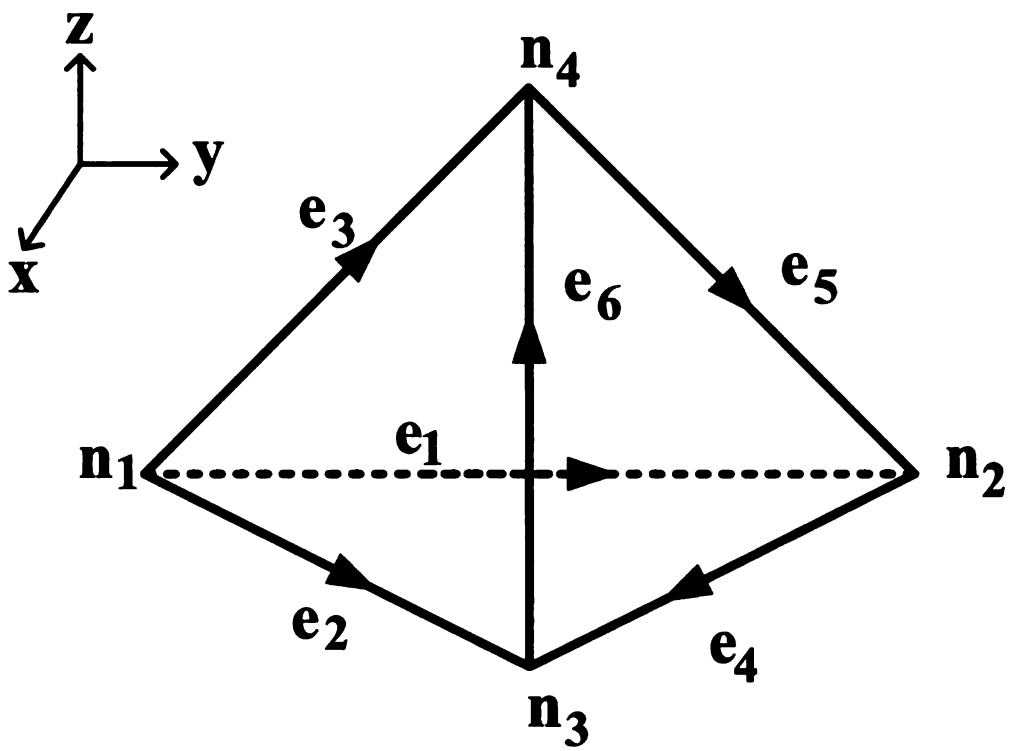


Figure 3.2. Tetrahedron element and local edge-node numeration.

as well. It has a constant tangential component along the edge i and linear normal components along all the edges (CT/LN). The divergency of \vec{W}_i is zero and its curl is not zero. In addition, vector-basis function \vec{W}_i satisfies the continuity of the tangential field across the edges of each element.

The constants a_i^e, b_i^e, c_i^e , and d_i^e in (3.69) are found as follow: Let ϕ^e be a first-order-polynomial function. Within the tetrahedron, ϕ^e is approximated by

$$\phi^e(x, y, z) = a^e + b^e x + c^e y + d^e z, \quad (3.70)$$

where a^e, b^e, c^e , and d^e are unknown coefficients.

Enforcing (3.70) at the four tetrahedron nodes the following system of equations is obtained

$$\phi_1^e(x, y, z) = a^e + b^e x_1 + c^e y_1 + d^e z_1$$

$$\phi_2^e(x, y, z) = a^e + b^e x_2 + c^e y_2 + d^e z_2$$

$$\phi_3^e(x, y, z) = a^e + b^e x_3 + c^e y_3 + d^e z_3$$

$$\phi_4^e(x, y, z) = a^e + b^e x_4 + c^e y_4 + d^e z_4 \quad (3.71)$$

Each unknown coefficient is expressed in terms of the global coordinates x, y , and z

of the four nodes

$$a^e = \frac{1}{6V^e} \begin{vmatrix} \phi_1^e & x_1 & y_1 & z_1 \\ \phi_2^e & x_2 & y_2 & z_2 \\ \phi_3^e & x_3 & y_3 & z_3 \\ \phi_4^e & x_4 & y_4 & z_4 \end{vmatrix} = \frac{1}{6V^e} (a_1^e \phi_1^e + a_2^e \phi_2^e + a_3^e \phi_3^e + a_4^e \phi_4^e) \quad (3.72)$$

$$b^e = \frac{1}{6V^e} \begin{vmatrix} 1 & \phi_1^e & y_1 & z_1 \\ 1 & \phi_2^e & y_2 & z_2 \\ 1 & \phi_3^e & y_3 & z_3 \\ 1 & \phi_4^e & y_4 & z_4 \end{vmatrix} = \frac{1}{6V^e} (b_1^e \phi_1^e + b_2^e \phi_2^e + b_3^e \phi_3^e + b_4^e \phi_4^e) \quad (3.73)$$

$$c^e = \frac{1}{6V^e} \begin{vmatrix} 1 & x_1 & \phi_1^e & z_1 \\ 1 & x_2 & \phi_2^e & z_2 \\ 1 & x_3 & \phi_3^e & z_3 \\ 1 & x_4 & \phi_4^e & z_4 \end{vmatrix} = \frac{1}{6V^e} (c_1^e \phi_1^e + c_2^e \phi_2^e + c_3^e \phi_3^e + c_4^e \phi_4^e) \quad (3.74)$$

$$d^e = \frac{1}{6V^e} \begin{vmatrix} 1 & x_1 & y_1 & \phi_1^e \\ 1 & x_2 & y_2 & \phi_2^e \\ 1 & x_3 & y_3 & \phi_3^e \\ 1 & x_4 & y_4 & \phi_4^e \end{vmatrix} = \frac{1}{6V^e} (d_1^e \phi_1^e + d_2^e \phi_2^e + d_3^e \phi_3^e + d_4^e \phi_4^e) \quad (3.75)$$

where V^e is the volume of the tetrahedron which is calculated as

$$V^e = \frac{1}{6} \begin{vmatrix} 1 & x_1 & y_1 & z_1 \\ 1 & x_2 & y_2 & z_2 \\ 1 & x_3 & y_3 & z_3 \\ 1 & x_4 & y_4 & z_4 \end{vmatrix} \quad (3.76)$$

or expanding the determinant, equation (3.76) takes the form

$$V^e = \frac{1}{6} \left\{ (x_1 - x_4) [(y_2 - y_4)(z_3 - z_4) - (y_3 - y_4)(z_2 - z_4)] + \right. \\ (y_1 - y_4) [(z_2 - z_4)(x_3 - x_4) - (z_3 - z_4)(x_2 - x_4)] + \\ \left. (z_1 - z_4) [(x_2 - x_4)(y_3 - y_4) - (x_3 - x_4)(y_2 - y_4)] \right\} \quad (3.77)$$

From (3.72)-(3.75), the coefficients a^e, b^e, c^e , and d^e are expressed in terms of the global coordinates of the four tetrahedron's nodes as

$$a_1^e = x_2^e (y_3^e z_4^e - y_4^e z_3^e) + y_2^e (z_3^e x_4^e - z_4^e x_3^e) + z_2^e (x_3^e y_4^e - y_3^e x_4^e) \quad (3.78)$$

$$a_2^e = x_1^e (y_4^e z_3^e - y_3^e z_4^e) + y_1^e (z_4^e x_3^e - z_3^e x_4^e) + z_1^e (x_4^e y_3^e - y_4^e x_3^e) \quad (3.79)$$

$$a_3^e = x_1^e (y_2^e z_4^e - y_4^e z_2^e) + y_1^e (z_2^e x_4^e - z_4^e x_2^e) + z_1^e (x_2^e y_4^e - y_2^e x_4^e) \quad (3.80)$$

$$a_4^e = x_1^e (y_3^e z_2^e - y_2^e z_3^e) + y_1^e (z_3^e x_2^e - z_2^e x_3^e) + z_1^e (x_3^e y_2^e - y_3^e x_2^e) \quad (3.81)$$

$$b_1^e = (y_4^e z_3^e - y_3^e z_4^e) + y_2^e (z_4^e - z_3^e) + z_2^e (y_3^e - y_4^e) \quad (3.82)$$

$$b_2^e = (y_3^e z_4^e - y_4^e z_3^e) + y_1^e (z_3^e - z_4^e) + z_1^e (y_4^e - y_3^e) \quad (3.83)$$

$$b_3^e = (y_4^e z_2^e - y_2^e z_4^e) + y_1^e (z_4^e - z_2^e) + z_1^e (y_2^e - y_4^e) \quad (3.84)$$

$$b_4^e = (y_2^e z_3^e - y_3^e z_2^e) + y_1^e (z_2^e - z_3^e) + z_1^e (y_3^e - y_2^e) \quad (3.85)$$

$$c_1^e = (z_4^e x_3^e - x_4^e z_3^e) + x_2^e (z_3^e - z_4^e) + z_2^e (x_4^e - x_3^e) \quad (3.86)$$

$$c_2^e = (z_3^e x_4^e - x_3^e z_4^e) + x_1^e (z_4^e - z_3^e) + z_1^e (x_3^e - x_4^e) \quad (3.87)$$

$$c_3^e = (x_2^e z_4^e - z_2^e x_4^e) + x_1^e (z_2^e - z_4^e) + z_1^e (x_4^e - x_2^e) \quad (3.88)$$

$$c_4^e = (z_2^e x_3^e - z_3^e x_2^e) + x_1^e (z_3^e - z_2^e) + z_1^e (x_2^e - x_3^e) \quad (3.89)$$

$$d_1^e = (y_3^e x_4^e - x_3^e y_4^e) + x_2^e (y_4^e - y_3^e) + y_2^e (x_3^e - x_4^e) \quad (3.90)$$

$$d_2^e = (x_3^e y_4^e - x_4^e y_3^e) + x_1^e (y_3^e - y_4^e) + y_1^e (x_4^e - x_3^e) \quad (3.91)$$

$$d_3^e = (y_2^e x_4^e - x_2^e y_4^e) + x_1^e (y_4^e - z_2^e) + y_1^e (x_2^e - x_4^e) \quad (3.92)$$

$$d_4^e = (x_2^e y_3^e - y_2^e x_3^e) + x_1^e (y_2^e - y_3^e) + y_1^e (x_3^e - x_2^e) \quad (3.93)$$

Continuing with the procedure followed in [22], (3.64) is divided in two elemental matrices given by

$$E_{i,j}^e = \frac{1}{\mu_r} \int_{\Omega_e} (\nabla \times \vec{W}_i) \cdot (\nabla \times \vec{W}_j) dV, \quad (3.94)$$

and

$$F_{i,j}^e = \varepsilon_r \int_{\Omega_e} \vec{W}_i \cdot \vec{W}_j dV \quad (3.95)$$

where

$$A_{i,j}^{FE} = E_{i,j}^e - k_0^2 F_{i,j}^e. \quad (3.96)$$

Using the vector basis function (3.68) the curl term becomes

$$\nabla \times \vec{W}_i = \frac{2l_i}{(6Ve)^2} [\hat{x} (c_{i1}d_{i2} - c_{i2}d_{i1}) + \hat{y} (d_{i1}b_{i2} - b_{i1}d_{i2}) + \hat{z} (b_{i1}c_{i2} - c_{i1}b_{i2})], \quad (3.97)$$

as before the sub indexes $i1$ and $i2$ correspond to the node 1 and 2 of edge i respectively. This local connection is given on Table 3.1 as shown in Figure 3.2.

Since (3.97) is constant, it can come out of the integrand on (3.94), therefore, this expression becomes

Table 3.1. Tetrahedron edge-node local conection.

Edge	N1	N2
1	1	2
2	1	3
3	1	4
4	2	3
5	4	2
6	3	4

$$E_{i,j}^e = \frac{4l_i l_j V^e}{\mu_r (6V^e)^4} \left[(c_{i1}^e d_{i2}^e - d_{i1}^e c_{i2}^e) (c_{j1}^e d_{j2}^e - d_{j1}^e c_{j2}^e) + \right. \\ \left. (d_{i1}^e b_{i2}^e - b_{i1}^e d_{i2}^e) (d_{j1}^e b_{j2}^e - b_{j1}^e d_{j2}^e) + (b_{i1}^e c_{i2}^e - c_{i1}^e b_{i2}^e) (b_{j1}^e c_{j2}^e - c_{j1}^e b_{j2}^e) \right] \quad (3.98)$$

In order to evaluate (3.95), (3.68) is expanded as

$$\vec{W}_i = \frac{l_i}{6V^e} \{ (L_{i1} b_{i2}^e - L_{i2} b_{i1}^e) \hat{x} + (L_{i1} c_{i2}^e - L_{i2} c_{i1}^e) \hat{y} + (L_{i1} d_{i2}^e - L_{i2} d_{i1}^e) \hat{z} \}. \quad (3.99)$$

If equation (3.99) is replaced in (3.95), the next expression is obtained

$$\begin{aligned}
F_{i,j}^e = \frac{\varepsilon r^l l_j}{(6Ve)^2} & \left\{ \int_{\Omega_e} (L_{i1} b_{i2}^e - L_{i2} b_{i1}^e) (L_{j1} b_{j2}^e - L_{j2} b_{j1}^e) dV + \right. \\
& \int_{\Omega_e} (L_{i1} c_{i2}^e - L_{i2} c_{i1}^e) (L_{j1} c_{j2}^e - L_{j2} c_{j1}^e) dV + \\
& \left. \int_{\Omega_e} (L_{i1} d_{i2}^e - L_{i2} d_{i1}^e) (L_{j1} d_{j2}^e - L_{j2} d_{j1}^e) dV \right\}. \quad (3.100)
\end{aligned}$$

Each one of the integrands on (3.100) are evaluated using the following general formula obtained from [38]

$$\int_{\Omega_e} (L_1)^k (L_2)^l (L_3)^m (L_4)^n dV = 6V^e \frac{k!l!m!n!}{(k+l+m+n+3)!}. \quad (3.101)$$

3.6 BI matrix entries using triangles

Before equation (3.65) can be discretized, some vector and dyadic manipulation need be carried out [39]. Substituting (3.51) into (3.65) yields

$$A_{i,j}^{BI} = k_0^2 \int_{S_a} \int_{S'_a} \left\{ \vec{W}_i \cdot \left[\hat{z} \times \left(\bar{I} + \frac{\nabla \nabla}{k_0^2} \right) \left(\frac{e^{-jk_0 R}}{2\pi R} \right) \times \hat{z} \right] \cdot \vec{W}_j \right\} dS' dS. \quad (3.102)$$

Equation (3.102) is split in two parts given in the next two expressions

$$I_{i,j}^e = \frac{1}{2\pi} \int_{S_a} \int_{S'_a} \left\{ [\vec{W}_i \cdot (\hat{z} \times \bar{I} \times \hat{z}) \cdot \vec{W}_j] \left(\frac{e^{-jk_0 R}}{R} \right) \right\} dS' dS, \quad (3.103)$$

and

$$H_{i,j}^e = \frac{1}{2\pi} \int_{S_a} \int_{S'_a} \left\{ \vec{W}_i \cdot \left[\hat{z} \times \nabla \nabla \left(\frac{e^{-jk_0 R}}{R} \right) \times \hat{z} \right] \cdot \vec{W}_j \right\} dS' dS, \quad (3.104)$$

where $A_{i,j}^{BI} = k_0^2 I_{i,j}^e + H_{i,j}^e$.

Replacing (3.20) into (3.103) and evaluating the first vector-dyad cross product, $I_{i,j}^e$ takes the form

$$I_{i,j}^e = \frac{1}{2\pi} \int_{S_a} \int_{S'_a} \left\{ [\vec{W}_i \cdot ((\hat{y}\hat{x} - \hat{x}\hat{y}) \times \hat{z}) \cdot \vec{W}_j] \left(\frac{e^{-jk_0 R}}{R} \right) \right\} dS' dS. \quad (3.105)$$

If the dyad-vector cross product is evaluated on (3.105), this becomes

$$I_{i,j}^e = \frac{-1}{2\pi} \int_{S_a} \int_{S'_a} \left\{ (\vec{W}_i \cdot \vec{W}_j) \left(\frac{e^{-jk_0 R}}{R} \right) \right\} dS' dS. \quad (3.106)$$

Equation (3.104) has a third order singularity that can be reduced if the derivatives are transferred to the basis function. With this in mind, it is found that

$$\vec{W}_i \cdot \hat{z} \times \nabla \nabla \left(\frac{e^{-jk_0 R}}{R} \right) = - (\hat{z} \times \vec{W}_i) \cdot \nabla \nabla \left(\frac{e^{-jk_0 R}}{R} \right), \quad (3.107)$$

thus, equation (3.104) is written as

$$H_{i,j}^e = \frac{-1}{2\pi} \int_{S_a} \int_{S'_a} \left\{ (\hat{z} \times \vec{W}_i) \cdot \nabla \nabla \left(\frac{e^{-jk_0 R}}{R} \right) \cdot (\hat{z} \times \vec{W}_j) \right\} dS' dS, \quad (3.108)$$

and further, since

$$\nabla \nabla \left(\frac{e^{-jk_0 R}}{R} \right) = -\nabla \nabla' \left(\frac{e^{-jk_0 R}}{R} \right) \quad (3.109)$$

equation (3.108) becomes

$$H_{i,j}^e = \frac{1}{2\pi} \int_{S_a} \int_{S'_a} \left\{ (\hat{z} \times \vec{W}_i) \cdot \nabla \nabla' \left(\frac{e^{-jk_0 R}}{R} \right) \cdot (\hat{z} \times \vec{W}_j) \right\} dS' dS. \quad (3.110)$$

The unprime gradient can be taken out of the integrand with respect to prime coordinates, therefore (3.110) gives

$$H_{i,j}^e = \frac{1}{2\pi} \int_{S_a} \left\{ (\hat{z} \times \vec{W}_i) \cdot \nabla \left[\int_{S'_a} \nabla' \left(\frac{e^{-jk_0 R}}{R} \right) \cdot (\hat{z} \times \vec{W}_j) dS' \right] \right\} dS, \quad (3.111)$$

from the vector identity,

$$\vec{A} \cdot \nabla w = \nabla \cdot (w \vec{A}) - w \nabla \cdot \vec{A} \quad (3.112)$$

the inner integral of (3.111) is recasted as

$$\begin{aligned}
& \int_{S'_a} \left\{ \nabla' \left(\frac{e^{-jk_0 R}}{R} \right) \cdot (\hat{z} \times \vec{W}_j) \right\} dS' = \\
& \int_{S'_a} \left\{ \nabla' \cdot \left[\left(\frac{e^{-jk_0 R}}{R} \right) (\hat{z} \times \vec{W}_j) \right] \right\} dS' - \\
& \int_{S'_a} \left\{ \left(\frac{e^{-jk_0 R}}{R} \right) \nabla' \cdot (\hat{z} \times \vec{W}_j) \right\} dS'. \tag{3.113}
\end{aligned}$$

Applying the divergence theorem to the first integral in the right hand side of (3.113) yields

$$\begin{aligned}
& \int_{S'_a} \left\{ \nabla' \cdot \left[\left(\frac{e^{-jk_0 R}}{R} \right) (\hat{z} \times \vec{W}_j) \right] \right\} dS' = \\
& \oint_{C'} \left\{ \left(\frac{e^{-jk_0 R}}{R} \right) (\hat{z} \times \vec{W}_j) \cdot \hat{m} \right\} dl' \tag{3.114}
\end{aligned}$$

where C' bounds S'_a , i.e. the perimeter of the triangle element and the unit vector \hat{m} is tangential to S'_a . The closed contour integral vanishes because of the properties of basis function used to expand the fields. The proof of this statement is given in Appendix C.1. Therefore (3.113) becomes

$$\int_{S'_a} \left\{ \nabla' \left(\frac{e^{-jk_0 R}}{R} \right) \cdot (\hat{z} \times \vec{W}_j) \right\} dS' =$$

$$\int_{S'_a} \left\{ \left(\frac{e^{-jk_0 R}}{R} \right) \nabla' \cdot (\hat{z} \times \vec{W}_j) \right\} dS'. \quad (3.115)$$

Thus, using (3.115) and reorganizing some terms, equation (3.111) takes the form

$$H_{i,j}^e = \frac{1}{2\pi} \int_{S_a} \int_{S'_a} \left\{ (\hat{z} \times \vec{W}_i) \cdot \nabla \left(\frac{e^{-jk_0 R}}{R} \right) \nabla' \cdot (\hat{z} \times \vec{W}_j) \right\} dS' dS. \quad (3.116)$$

Using similar arguments to obtain (3.113) and the divergence theorem, equation (3.116) is written as

$$H_{i,j}^e = \frac{1}{2\pi} \int_{S_a} \int_{S'_a} \left\{ \nabla \cdot (\hat{z} \times \vec{W}_i) \nabla' \cdot (\hat{z} \times \vec{W}_j) \left(\frac{e^{-jk_0 R}}{R} \right) \right\} dS' dS \quad (3.117)$$

whose kernel singularity is two orders lower than equation (3.104) kernel.

For the exterior basis function, it is assumed a triangular mesh covering the aperture. Let $\hat{z} \times \vec{E}(x', y') = -\vec{M}$, where $\vec{E}(x', y')$ is the electric field in the aperture; using Rao, Wilton, and Glisson (RWG) basis function [40], the magnetic surface current on the aperture \vec{M} is expanded as

$$\vec{M} = \sum_i M_i \vec{f}_i(\vec{r}) \quad (3.118)$$

where

$$\vec{f}_i(\vec{r}) = \begin{cases} \frac{l_i}{2A_i^+} \vec{\rho}_i^+ & \vec{r} \text{ in } T_i^+ \\ \frac{l_i}{2A_i^-} \vec{\rho}_i^- & \vec{r} \text{ in } T_i^- \\ 0 & \text{otherwise} \end{cases} \quad (3.119)$$

and l_i is the length of i^{th} edge that is shared by triangles T_i^+ and T_i^- . A_i^\pm is the area of T_i^\pm ; the vector $\vec{\rho}_i^+$ is directed away from the free vertex of T_i^+ and $\vec{\rho}_i^-$ is directed towards the free vertex of T_i^- as it is shown on Figure 3.3. It is important to notice that each basis function is associated with an interior edge, shared by two triangles, everywhere else, this basis function vanishes.

RWG basis function is attractive to model surface current within triangular regions because it only has a component that is normal to the i^{th} edge (Figure 3.3) and there are not normal components to the remaining edges. In addition, the component of current normal to the i^{th} is constant and continuous across the edge, i.e., the normal component of $\vec{\rho}_i^\pm$ along the edge i is just the height of triangle T_i^\pm which is $2A_i^\pm/l_n$. This factor normalizes $\vec{f}_i(\vec{r})$ and its flux density normal to the edge i is one. Current continuity is thus preserved and all the edges of T_i^+ and T_i^- are free of line charges. Using Gauss' divergence theorem, it can be proved that the basis function (3.119) are free of charge accumulation on each triangle. The detailed proof can be found on Appendix C.2.

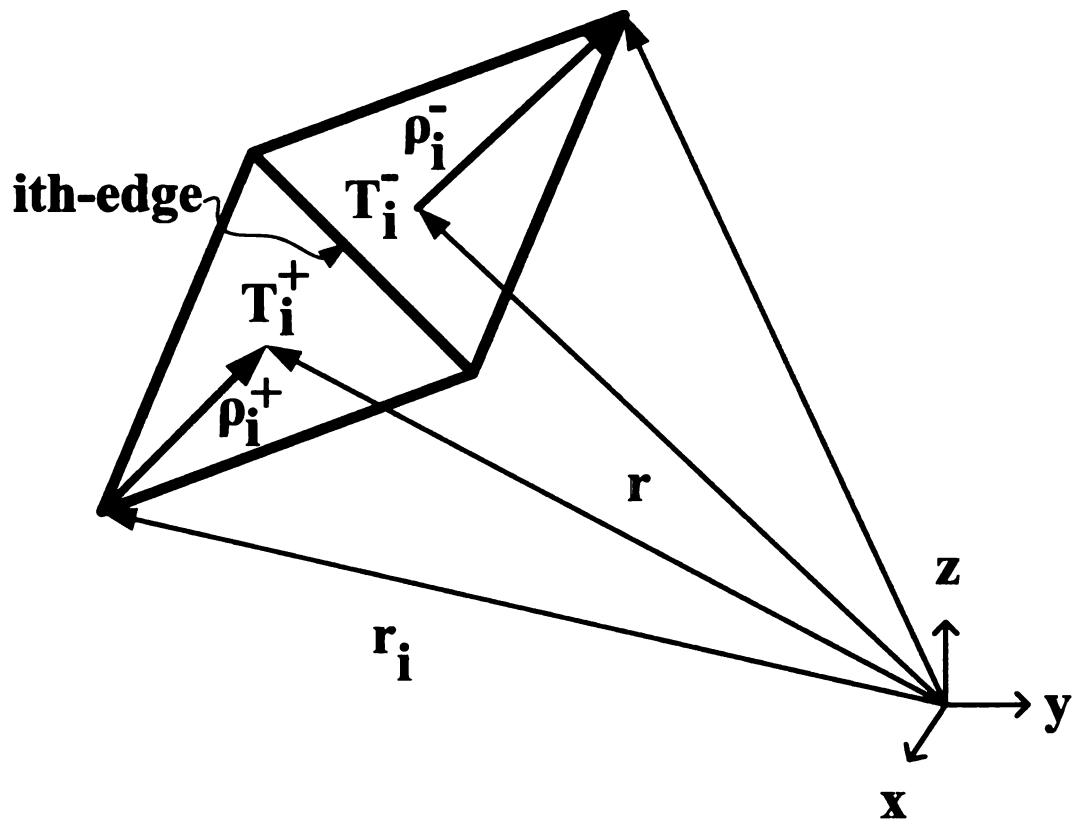


Figure 3.3. Two triangles sharing an edge and their geometrical parameters.

Equating (3.118) with the unknown electric field coefficients (E_i)

$$\hat{z} \times \sum_i E_i \vec{W}_i = - \sum_i M_i \vec{f}_i, \quad (3.120)$$

and noticing that $\vec{\rho}_n^\pm = \pm (\vec{r} - \vec{r}_i)$, the RWG basis function becomes

$$\vec{W}_i = \frac{l_i s_i}{2A_i^\pm} [(x - x_i) \hat{y} - (y - y_i) \hat{x}], \quad (3.121)$$

and further

$$\nabla \cdot (\hat{z} \times \vec{W}_i) = \frac{-l_i s_i}{2A_i^\pm}. \quad (3.122)$$

Substituting (3.121) into (3.106) yields

$$I_{i,j}^e = \frac{-l_i l_j s_i s_j}{8\pi A_i^\pm A_j^\pm} \int_{S_a} \int_{S'_a} \left\{ [(x - x_i)(x' - x_j) + (y - y_i)(y' - y_j)] \frac{e^{-jk_0 R}}{R} \right\} dS' dS. \quad (3.123)$$

In addition, after using (3.122), equation (3.117) takes the form

$$H_{i,j}^e = \frac{l_i l_j s_i s_j}{2\pi A_i^\pm A_j^\pm} \int_{S_a} \int_{S'_a} \left\{ \frac{e^{-jk_0 R}}{R} \right\} dS' dS \quad (3.124)$$

where

$$s_i = \begin{cases} +1 & \vec{r} \text{ in } T_i^+ \\ -1 & \vec{r} \text{ in } T_i^- \end{cases} \quad (3.125)$$

and

$$s_j = \begin{cases} +1 & \vec{r} \text{ in } T_j^+ \\ -1 & \vec{r} \text{ in } T_j^- \end{cases} \quad (3.126)$$

3.6.1 Numerical integration of BI equations

The integrals in equations (3.123) and (3.124) do not have closed form and must be evaluated numerically. The most efficient way to evaluate them is using the Gaussian quadrature rule for triangles. The normalized area coordinates [38] are defined as follows

$$\zeta_1 = \frac{A_1}{A_q}, \quad \zeta_2 = \frac{A_2}{A_q}, \quad \zeta_3 = \frac{A_3}{A_q}, \quad (3.127)$$

where ζ_i ($i = 1, \dots, 3$) are known as simplex triangular coordinates and satisfy the following constraint $\zeta_1 + \zeta_2 + \zeta_3 = 1$. The areas A_1 , A_2 , A_3 and A_q are shown on Figure 3.4.

The transformation from Cartesian to normalized area coordinates is written as

$$\vec{r}_i = \zeta_1 \vec{r}_1 + \zeta_2 \vec{r}_2 + \zeta_3 \vec{r}_3 \quad (3.128)$$

where \vec{r}_i is a position vector from the origin to the i^{th} vertex of triangle T^q as it is shown on Figure 3.4.

Using Gaussian quadrature rule [42], the surface integral over the triangle T^q of a function $G(\vec{r})$ is given by

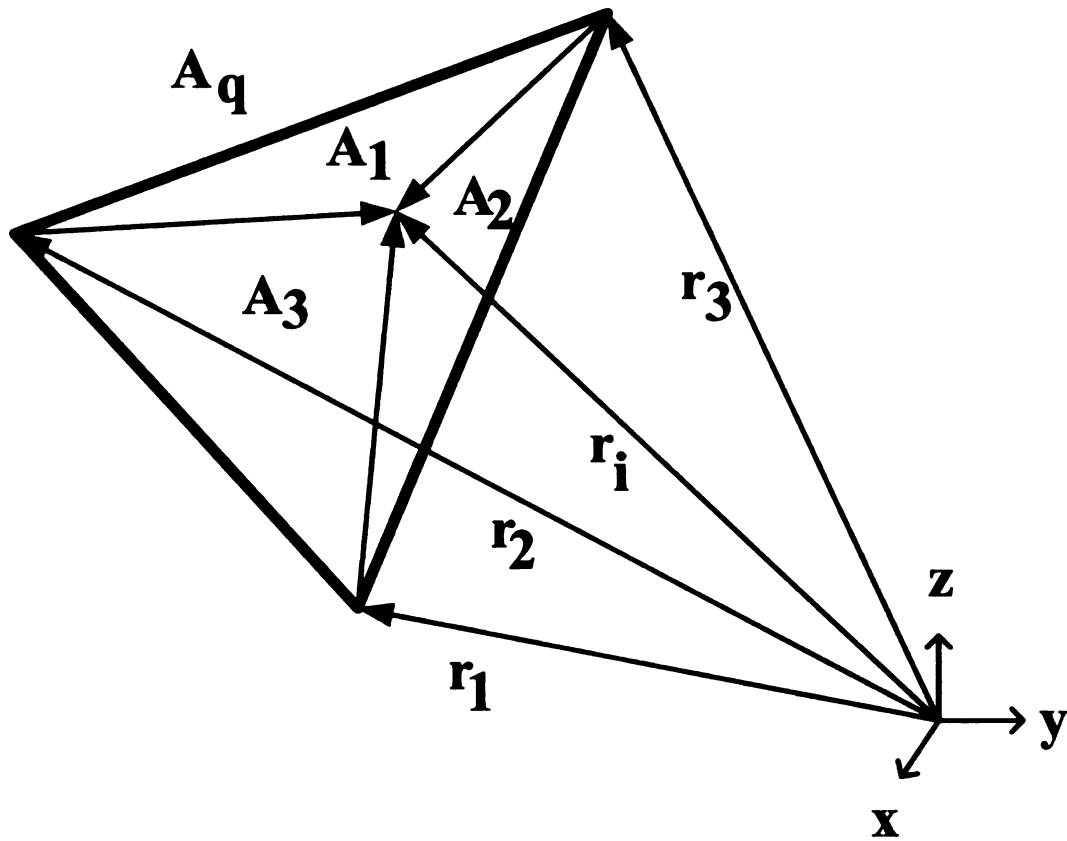


Figure 3.4. Local coordinates for triangle T^q .

$$\int_{T^q} G(\vec{r}) dS = 2A^q \int_0^1 \int_0^{1-\zeta_2} G[\zeta_1 \vec{r}_1 + \zeta_2 \vec{r}_2 + \zeta_3 \vec{r}_3] d\zeta_1 d\zeta_2$$

$$\approx A^q \sum_{i=1}^n W_i G[\zeta_1^i \vec{r}_1 + \zeta_2^i \vec{r}_2 + \zeta_3^i \vec{r}_3]. \quad (3.129)$$

In this, n is the number of integration points over the triangle, ζ_j^i are the triangular coordinates, and W_i are integration weights. These parameters are given in Table 3.2 where $\alpha_1 = 0.0597158717$, $\beta_1 = 0.4701420641$, $\alpha_2 = 0.7974279853$, and $\beta_2 = 0.1012865073$.

For the case of (3.123) and (3.124), the integrals are evaluated over a source triangle (T^p) and observation triangle (T^q) instead of edge-by-edge. After computing the integrals for each triangle, the edge contribution are calculated and accumulated in the appropriated BI matrix position. This is a full matrix and because of (3.123) and (3.124) form, it is symmetric. Therefore, it is only necessary to compute the upper (or lower) triangle of the matrix.

3.6.2 BI self term evaluation

When the observation and the source triangle coalesce, the singularities in the kernels of (3.123) and (3.124) must be isolated and evaluated analytically. Equations (3.123) and (3.124) may be rewritten in a more convenient form expressing global as local coordinates using the expression

Table 3.2. Triangular coordinates and integration weights [38].

Number of points	$\zeta_1^i, \zeta_2^i, \zeta_3^i$	W_i	
1	1/3,1/3,1/3	1	
4	1/3,1/3,1/3	-27/48	
	0.6,0.2,0.2	25/48	
	0.2,0.6,0.2		
7	0.2,0.2,0.6	0.2250000000	
	1/3,1/3,1/3		
	$\alpha_1, \beta_1, \beta_1$		0.1323941527
	$\beta_1, \alpha_1, \beta_1$		
	$\beta_1, \beta_1, \alpha_1$		
	$\alpha_2, \beta_2, \beta_2$		0.1259391805
	$\beta_2, \alpha_2, \beta_2$		
	$\beta_2, \beta_2, \alpha_2$		

$$\left[(x - x_i)(x' - x_j) + (y - y_i)(y' - y_j) \right] = (\vec{r} - \vec{r}_i) \cdot (\vec{r}' - \vec{r}_j) = \vec{\rho}_i^+ \cdot \vec{\rho}_j^+. \quad (3.130)$$

Substituting (3.130) into (3.123) yields

$$I_{i,j}^{p,q} = \frac{-l_i l_j s_i s_j}{8\pi A^p A^q} \int_{Tp} \int_{Tq} \vec{\rho}_i^+ \cdot \vec{\rho}_j^+ \frac{e^{-jk_0 R}}{R} dS' dS \quad (3.131)$$

The inner integral of (3.131) can be written as

$$\int_{Tq} \vec{\rho}_j^+ \frac{e^{-jk_0 R}}{R} dS' = \int_{Tq} \vec{\rho}_j^+ \frac{e^{-jk_0 R} - 1}{R} dS' + \int_{Tq} \frac{\vec{\rho}' - \vec{\rho}}{R} dS' + (\vec{\rho} - \vec{\rho}_j) \int_{Tq} \frac{1}{R} dS', \quad (3.132)$$

where $\vec{\rho}$, $\vec{\rho}'$, and $\vec{\rho}_j$ are the projections of the position vectors \vec{r} , \vec{r}' , and \vec{r}_j respectively as it is shown on Figure 3.5.

The first integral in the right hand side of (3.132) is bounded and can be numerically evaluated. The last two integrals can be evaluated analytically using [41] (Appendix D). The term containing uniform source distribution, i.e.

$$\int_{Tq} \frac{1}{R} dS', \quad (3.133)$$

it is evaluated using Appendix D.1.

In addition, the term containing linearly varying source distribution, i.e.

$$\int_{Tq} \frac{\vec{\rho}' - \vec{\rho}}{R} dS', \quad (3.134)$$

it is evaluated using Appendix D.2. The same process is repeated for the outer integral of (3.132).

The scalar potential in equation (3.124) may be rewritten as

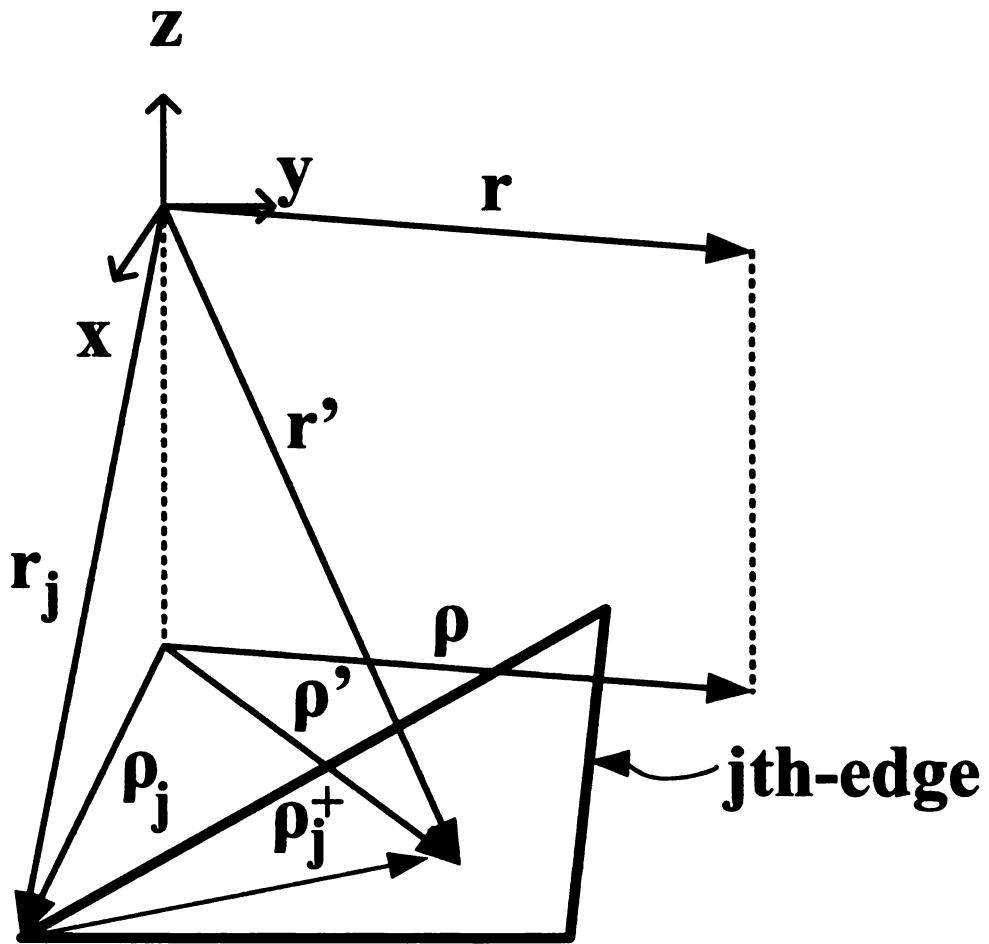


Figure 3.5. Projections of \vec{r} , \vec{r}' , and \vec{r}_j onto the plain that contains T^q .

$$H_{i,j}^{p,q} = \frac{l_i l_j s_i s_j}{2\pi A^p A^q} \int_{Tp} \int_{Tq} \left\{ \frac{e^{-jk_0 R}}{R} \right\} dS' dS. \quad (3.135)$$

The inner integral of (3.135) can be expressed as

$$\int_{Tq} \left\{ \frac{e^{-jk_0 R}}{R} \right\} dS' = \int_{Tq} \left\{ \frac{e^{-jk_0 R} - 1}{R} \right\} dS' + \int_{Tq} \left\{ \frac{1}{R} \right\} dS' \quad (3.136)$$

The first term of the right hand side of (3.136) is bounded and can be evaluated numerically, the second term can be evaluated analytically as shown in Appendix D.1.

3.7 FE-BI program structure

In the previous sections it was outlined the formulation of the FE (3.98)-(3.100) and BI (3.132)- (3.135) elemental equations. In this work, these equations are implemented in a FE-BI program written in Fortran [44]. FE-BI programs have common modules [45], [46]. These modules are the pre-processing, meshing, pre-assembly, matrix assembly, matrix solution, and post-processing.

3.7.1 Pre-processing

In this module information about the problem to be solved is collected. This includes: geometry specification, electric properties of material, type of excitation, and frequency. In this project, the geometry is an open cavity filled with a uniform dielectric and the excitation is an infinitely thin coaxial probe.

3.7.2 Meshing

Since the TLW antenna has a simple geometry, the meshing starts with the specification of a surface triangular mesh. This mesh is generated using SkyMesh [51]. Figure 3.6 shows different apertures that are investigated in this work. The rectangular, the bow-tie, and the circular are considered in order to design the most efficient TLW antenna. Of course, these surface meshes are not to scale because the TLW antenna considered in this work is several wavelengths long (i.e., 7λ) and the width is in the order of 0.1λ . Note that because of the FE-BI formulation in this work, the open aperture is discretized but the infinite ground plane does not need to be considered. The surface mesh is extruded to obtain a volumetric mesh. This extrusion process is as follows: the number of layers and their thicknesses need to be specified. The surface nodes given in the surface mesh are replicated and displaced by the thickness of each layer. This creates prisms in each layer. Then, edges are formed for each prism. Finally, tetrahedrons are created from the prisms [52]. The information that is obtained from the meshing process is organized in form of arrays. The *TetNodes* array contains the global nodes forming each tetrahedron. The *GlobalNodes* array contains the global node location on Cartesian coordinate system. The *EdgesNodes* array contains the nodes that form each edge and associated with it is its corresponding unknown number. The *TetEdges* array identifies the global edges that are associated with each tetrahedron. The *TriEdges* array contains the edges that form the aperture triangles.

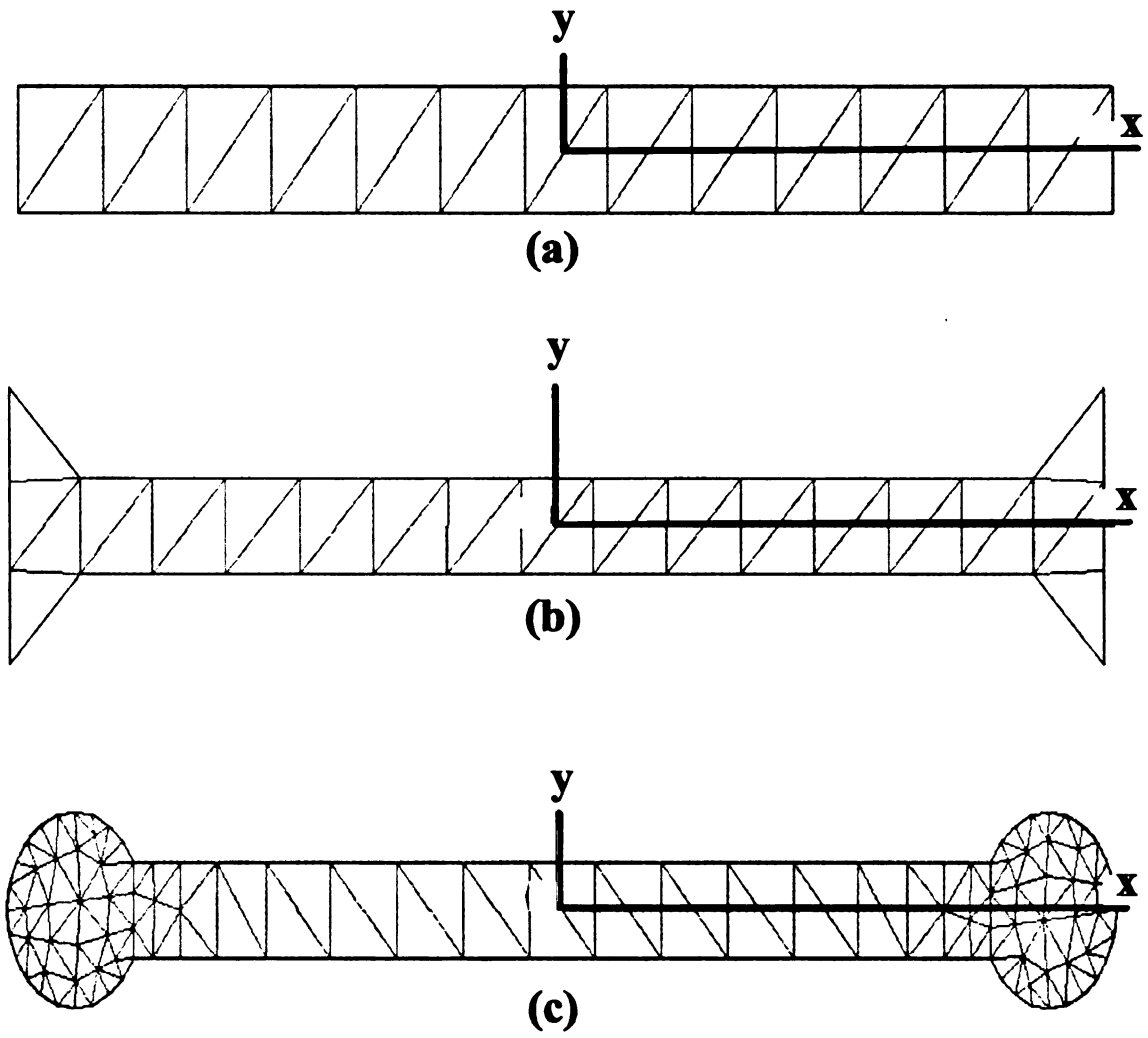


Figure 3.6. Different configurations of surfacemesh: (a)Rectangular, (b)Bow-tie, (c)Circular.

3.7.3 Pre-assembly of FE-BI matrices for the TLW antenna

Pre-assembly is used to determine the topology of the FE-BI matrix before computing its actual entries. The FE part of the matrix is sparse and the BI part is dense. As mentioned before, the cavity is discretized with tetrahedra and the aperture with triangles. Each one of the edges that form these elements is an unknown if it is not on the metallic boundary of the cavity. In other words, that edge must belong to two different elements. The dimensions of the global matrix depends on the number of unknowns, for a typical TLW antenna with dimensions $7\lambda \times 0.07\lambda \times 0.4\lambda$ (where $\lambda = 3.33\text{cm}$) and discretized using 28,000 tetrahedrons, the number of unknowns is 22,700. When the number of unknowns is high, it is not practical to store directly the FE matrix and the BI matrix. For instance, for this TLW antenna, the number of non-zero elements in the FE matrix is 222,982, which means that there are 515,067.020 (99.95%) entries that are zero. Therefore, it is important to use a storage scheme such as compressed sparse row (CSR) method [17] in order to avoid storing all those zeros. In this scheme, the values of nonzero elements of the sparse matrix are stored in a vector (*values*) and their corresponding column indices in another vector (*colIndex*). The dimension of each one of these vectors is the number of nonzero elements. Also, there is another vector (*numberElemxRow*) with the number of nonzero elements per row. The dimension of this vector is the number of unknowns. In addition, since the BI matrix is symmetric, it is only necessary to compute the elements in the upper triangle of the matrix. Thus, the storage saving can be significant.

3.7.4 Matrix assembly

In this process the matrix entries are computed and stored in an orderly fashion using the CSR technique. The matrix is assembled adding the contribution due to each edge pair of interaction for each tetrahedron.

3.7.5 Matrix solution of FE-BI linear system using biconjugate gradient (BiCG) method with preconditioning

In order to solve the FE-BI linear system the BiCG method with preconditioning is used [17]. This method is easy to implement and present fast convergence for the TLW antennas simulated in this dissertation. The preconditioner used is diagonal due the simplicity of computing its inverse. The implemented pseudocode in this dissertation is given in [17] and repeated here:

Initialization:

\mathbf{x} is given

$$\mathbf{r} = \mathbf{b} - \mathbf{A}\mathbf{x}; \mathbf{p} = \mathbf{r}; tmp = \mathbf{r} \cdot \mathbf{r}$$

Repeat until ($resd \leq tol$)

$$(1) \mathbf{q} = \mathbf{A}\mathbf{p}$$

$$(2) \alpha = tmp / (\mathbf{q} \cdot \mathbf{p})$$

$$(3) \mathbf{x} = \mathbf{x} + \alpha \mathbf{p}$$

$$(4) \mathbf{r} = \mathbf{r} - \alpha \mathbf{q}$$

$$(5) \mathbf{q} = \text{inv}(\mathbf{C}) \times \mathbf{r}$$

$$(6) resd = \sqrt{|\mathbf{r} \cdot \mathbf{r}^*|}$$

$$(7) \beta = (\mathbf{r} \cdot \mathbf{q}) / tmp$$

$$(8) tmp = \beta \times tmp$$

$$(9) \mathbf{p} = \mathbf{q} + \beta \mathbf{p}$$

EndRepeat

where $\mathbf{A}\mathbf{x}$ and $\mathbf{A}\mathbf{p}$ denotes a complex matrix vector product, \mathbf{C} is the preconditioning matrix, \mathbf{q} , \mathbf{p} , \mathbf{x} and \mathbf{r} are complex vectors; α, β, tmp are complex scalars; $resd, tol$ are real scalars. An initial guess is given at the beginning of the algorithm and \mathbf{x} is the unknown solution vector.

3.7.6 Post-processing

Once the field coefficients are found from solving the linear system (3.62), different parameters can be computed such as the antenna's input impedance, reflection coefficient, voltage standing wave ratio (VSWR), and radiation pattern. In addition, the

TLW antenna's propagation constants can be calculated from these coefficients.

3.7.6.1 Input Impedance, reflection coefficient, and VSWR

The input impedance of an infinitely thin probe feed with a current I_0 and located on the i th edge is given by

$$Z_{in} = \frac{E_i l_i}{I_0}. \quad (3.137)$$

The reflection coefficient (Γ) and the VSWR (assuming a 50Ω reference impedance) can be found using

$$\Gamma = \frac{Z_{in} - 50}{Z_{in} + 50}, \quad (3.138)$$

and

$$VSWR = \frac{1 + |\Gamma|}{1 - |\Gamma|}. \quad (3.139)$$

3.7.6.2 Radiation pattern

The far-zone radiated field of an aperture antenna is given by [29]

$$\vec{E} = \lim_{\vec{r} \rightarrow \infty} \left\{ \frac{jk}{\epsilon} \hat{r} \times \vec{F}(\vec{r}) \right\} \quad (3.140)$$

where $\hat{r} = \hat{x} \sin \theta \cos \phi + \hat{y} \sin \theta \sin \phi + \hat{z} \cos \theta$.

The magnetic vector potential $\vec{F}(\vec{r})$ can be found from

$$\vec{F}(\vec{r}) = \frac{-\varepsilon e^{-jk r}}{4\pi r} \oint_{S'} (\hat{n}' \times \vec{E}(\vec{r}')) e^{-jk\hat{r} \cdot \vec{r}'} dS' \quad (3.141)$$

where $\hat{n}' = \hat{z}$ and $\vec{r}' = x'\hat{x} + y'\hat{y}$.

Using the expansion of the electric field in each triangle

$$\vec{E} = \sum_{i=1}^3 E_i \vec{W}_i \quad (3.142)$$

where the electric field coefficients E_i are now known and the vector basis function is given on (3.121). Therefore (3.141) becomes

$$\vec{F}(\vec{r}) = \frac{-\varepsilon e^{-jk r}}{4\pi r} \sum_{i=1}^3 E_i \oint_{S'} (\hat{z}' \times \vec{W}_i) e^{-jk\hat{r} \cdot \vec{r}'} dS'. \quad (3.143)$$

Performing the cross product $(\hat{z}' \times \vec{W}_i)$ and substituting this result into (3.143), it is found that

$$\vec{F}(\vec{r}) = \frac{\varepsilon e^{-jk r}}{4\pi r} \sum_{i=1}^3 E_i \frac{l_i s_i}{2A_i} \oint_{S'} [(x' - x_i)\hat{x} + (y' - y_i)\hat{y}] e^{-jk\hat{r} \cdot \vec{r}'} dS'. \quad (3.144)$$

The surface integral in (3.144) is computed using Gaussian quadrature (3.129) and summing the contribution of each triangle in the aperture.

Hence, using (3.144), the electric field (3.140) takes the form

$$\vec{E} = \frac{jk}{\epsilon} \{ -\hat{x}F_y \cos \theta + \hat{y}F_x \cos \theta + \hat{z}(F_y \sin \theta \cos \phi - F_x \sin \theta \sin \phi) \} \quad (3.145)$$

where

$$F_x(\vec{r}) = \frac{\epsilon e^{-jkr}}{4\pi r} \sum_{T_q=1}^N \sum_{i=1}^3 E_i \frac{l_i s_i}{2A_i} \oint_{T_q} (x' - x_i) e^{-jk\hat{r}\cdot\vec{r}'} dS'$$

$$F_y(\vec{r}) = \frac{\epsilon e^{-jkr}}{4\pi r} \sum_{T_q=1}^N \sum_{i=1}^3 E_i \frac{l_i s_i}{2A_i} \oint_{T_q} (y' - y_i) e^{-jk\hat{r}\cdot\vec{r}'} dS' \quad (3.146)$$

where N is the total number of triangles in the aperture.

Expressing (3.145) in spherical coordinates system, the θ and ϕ components are, respectively,

$$E_\theta = E_x \cos \theta \cos \phi + E_y \cos \theta \sin \phi - E_z \sin \theta \quad \text{and}$$

$$E_\phi = -E_x \sin \phi + E_y \cos \phi. \quad (3.147)$$

The radiation intensity $U(\theta, \phi)$ is defined in (1.14) and it is repeated here:

$$U(\theta, \phi) = \frac{1}{2Z_0} \left[|E_\theta(\theta, \phi)|^2 + |E_\phi(\theta, \phi)|^2 \right]. \quad (3.148)$$

The total radiated power is obtained by integrating the radiation intensity given by (3.148) over the entire solid angle of 4π . Thus

$$P_{rad} = \oint_{\Omega} U(\theta, \phi) d\Omega = \int_0^{2\pi} \int_0^{\pi} U(\theta, \phi) \sin \theta d\theta d\phi \quad (3.149)$$

Numerically, the total radiated power may be found using

$$P_{rad} = \left(\frac{\pi}{N}\right) \left(\frac{2\pi}{M}\right) \sum_{j=1}^M \sum_{i=1}^N U(\theta_i, \phi_j) \sin \theta_i \quad (3.150)$$

where the θ and ϕ coordinates were divided in N and M divisions respectively.

The absolute gain of an antenna in a given direction is defined as “the ratio of intensity, in a given direction, to the radiation intensity that would be obtained if the power accepted by the antenna were radiated isotropically. The radiation intensity corresponding to the isotropically radiated power is equal to the power accepted (input) by the antenna divided by 4π ” [30]. In equation form this can be expressed as

$$\text{gain} = 4\pi \frac{U(\theta, \phi)}{P_{in}} \quad (3.151)$$

where the P_{in} is given by

$$P_{in} = I_0 \cdot \{I_0\}^* \cdot \text{Real} \{Z_{in}\} \quad (3.152)$$

the operators $\{\}^*$ and $\text{Real} \{\}$ denote complex conjugate and real part, respectively.

The antenna efficiency is defined as the ratio between the radiated power and

input power:

$$\text{efficiency} = \frac{P_{rad}}{P_{in}} \quad (3.153)$$

The power absorbed by a load impedance may be computed using:

$$P_{RL} = \frac{|E_i l_i|}{2R_L} \quad (3.154)$$

where E_i is the electric field coefficient at i th edge and this edge is coincident with the location of the lumped load. l_i is the length of the i th edge and R_L is the real part of the load impedance.

3.7.6.3 Propagation constants

The propagation constants for the TLW antenna are determined using the method of least squares [43]. Given the data $\{(x_1, y_1), (x_2, y_2), \dots, (x_n, y_n)\}$, the error associated to $y = ax + b$ is

$$e(a, b) = \sum_{n=1}^N [y_n - (ax_n + b)]^2. \quad (3.155)$$

The values (a, b) that minimize the error are such that

$$\frac{\partial e}{\partial a} = 0, \quad \frac{\partial e}{\partial b} = 0. \quad (3.156)$$

Differentiating $e(a, b)$ yields

$$\frac{\partial e}{\partial a} = -2 \sum_{n=1}^N [y_n - (ax_n + b)] x_n$$

$$\frac{\partial e}{\partial b} = 2 \sum_{n=1}^N [y_n - (ax_n + b)]. \quad (3.157)$$

Using (3.156), it is found that

$$a \sum_{n=1}^N x_n^2 + b \sum_{n=1}^N x_n = \sum_{n=1}^N x_n y_n$$

$$a \sum_{n=1}^N x_n + bN = \sum_{n=1}^N y_n. \quad (3.158)$$

Solving for the slope in (3.158) this parameter becomes

$$a = \frac{N \sum_{n=1}^N x_n y_n - \sum_{n=1}^N x_n \sum_{n=1}^N y_n}{N \sum_{n=1}^N x_n^2 - \left(\sum_{n=1}^N x_n \right)^2} \quad (3.159)$$

and the independent term is given by

$$b = \frac{\sum_{n=1}^N x_n^2 \sum_{n=1}^N y_n - \sum_{n=1}^N x_n \sum_{n=1}^N x_n y_n}{N \sum_{n=1}^N x_n^2 - \left(\sum_{n=1}^N x_n \right)^2}. \quad (3.160)$$

In order to compute the propagation constants, it is assumed a TLW antenna with the aperture at $z = 0$ and the length along x . The electric field in the y direction is obtained from the values of the expansion coefficients on each edge

in the y direction. For each edge along the aperture there is a E_y , this is, $(x_1, E_{y1}), (x_2, E_{y2}), \dots (x_n, E_{yn})$. Since

$$e^{-\alpha_x k_0 x} e^{j\beta_x k_0 x} = E_y, \quad (3.161)$$

therefore,

$$-k_0 \alpha_x = \ln |E_y| \quad (3.162)$$

$$k_0 \beta_x = \text{angle}(E_y). \quad (3.163)$$

Using (3.159) α_x and β_x are estimated as

$$-k_0 \alpha_x = \frac{N \sum_{n=1}^N x_n \ln |E_{yn}| - \sum_{n=1}^N x_n \sum_{n=1}^N \ln |E_{yn}|}{N \sum_{n=1}^N x_n^2 - \left(\sum_{n=1}^N x_n \right)^2} \quad (3.164)$$

and

$$k_0 \beta_x = \frac{N \sum_{n=1}^N x_n [\text{angle}(E_{yn})] - \sum_{n=1}^N x_n \sum_{n=1}^N [\text{angle}(E_{yn})]}{N \sum_{n=1}^N x_n^2 - \left(\sum_{n=1}^N x_n \right)^2} \quad (3.165)$$

where

$$\text{angle}(E_{yn}) = \arctan \frac{\text{Im}(E_{yn})}{\text{Real}(E_{yn})}. \quad (3.166)$$

CHAPTER 4

ANTENNA DESIGN AND RESULTS

4.1 Design of the RT/Duroid 5880-filled TLW antenna

In order to find the optimum dimensions for the TLW antenna filled with RT/Duroid 5880 the TRM method is used. This method allows to specify h and w (Figure 2.1 (a)). Figure 4.1 shows the effect of three different values of h in the propagation constants while w is kept constant. If the antenna bandwidth is defined as the frequencies between $\alpha_z/k_0 = \beta_z/k_0$ and $\beta_z/k_0 = 1$, the antenna bandwidth for these three values is shown on Table 4.1. The greatest bandwidth value happens when $h = 0.75\text{cm}$ and $w = 0.0787\text{cm}$.

Table 4.1. RT/Duroid 5880-filled TLW antenna bandwidth for three different values of h .

w[cm]	h[cm]	Bandwidth[GHz]
0.0787	0.75	2.2
0.0787	0.80	1.9
0.0787	0.85	1.8

Similarly keeping h constant and varying w the behavior of the propagation constant is shown on Figure 4.2. The antenna bandwidth for these three values is shown on Table 4.2. Again, the greatest bandwidth value happens when $h = 0.75\text{cm}$ and $w = 0.0787\text{cm}$.

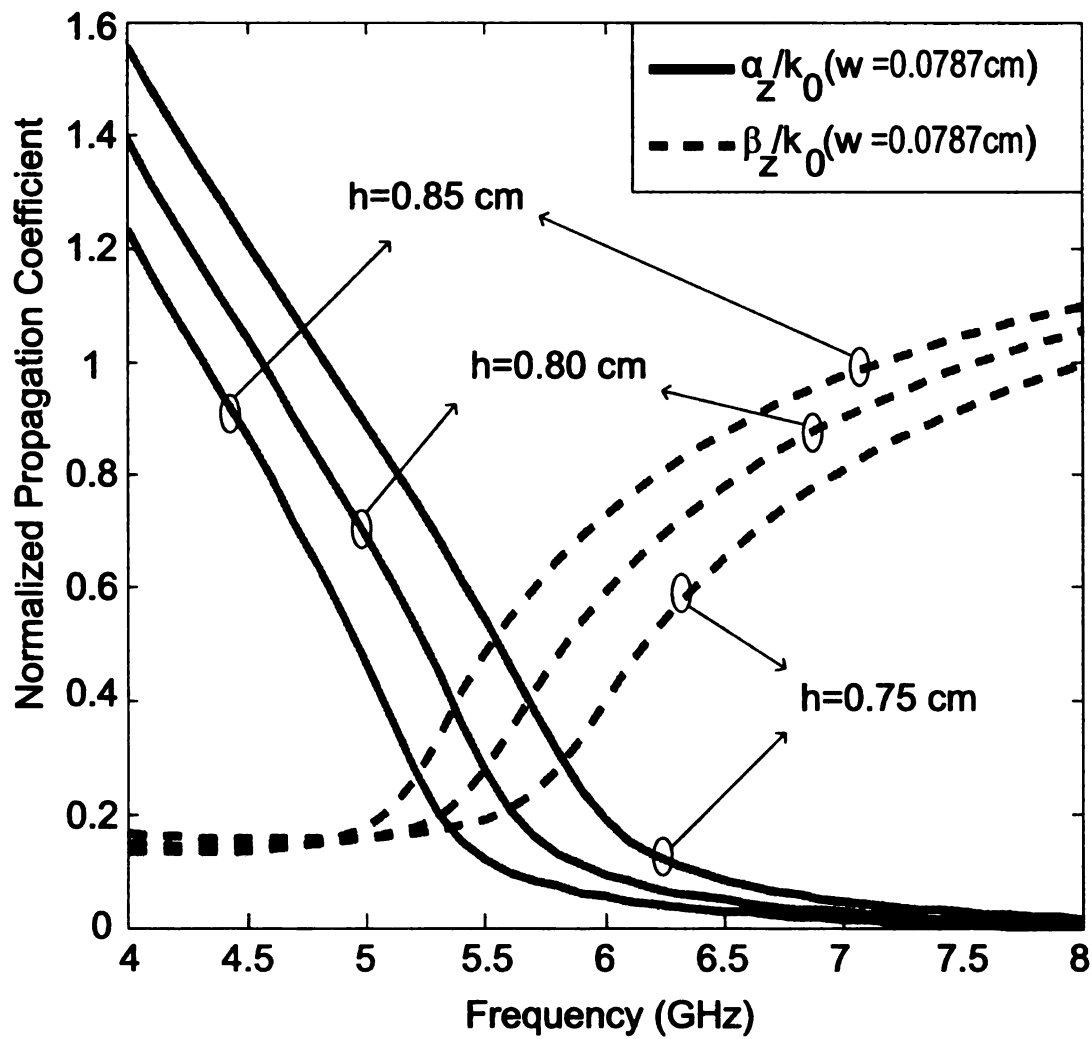


Figure 4.1. Effect of the variation of h in the propagation constants for the RT/Duroid 5880-filled TLW antenna.

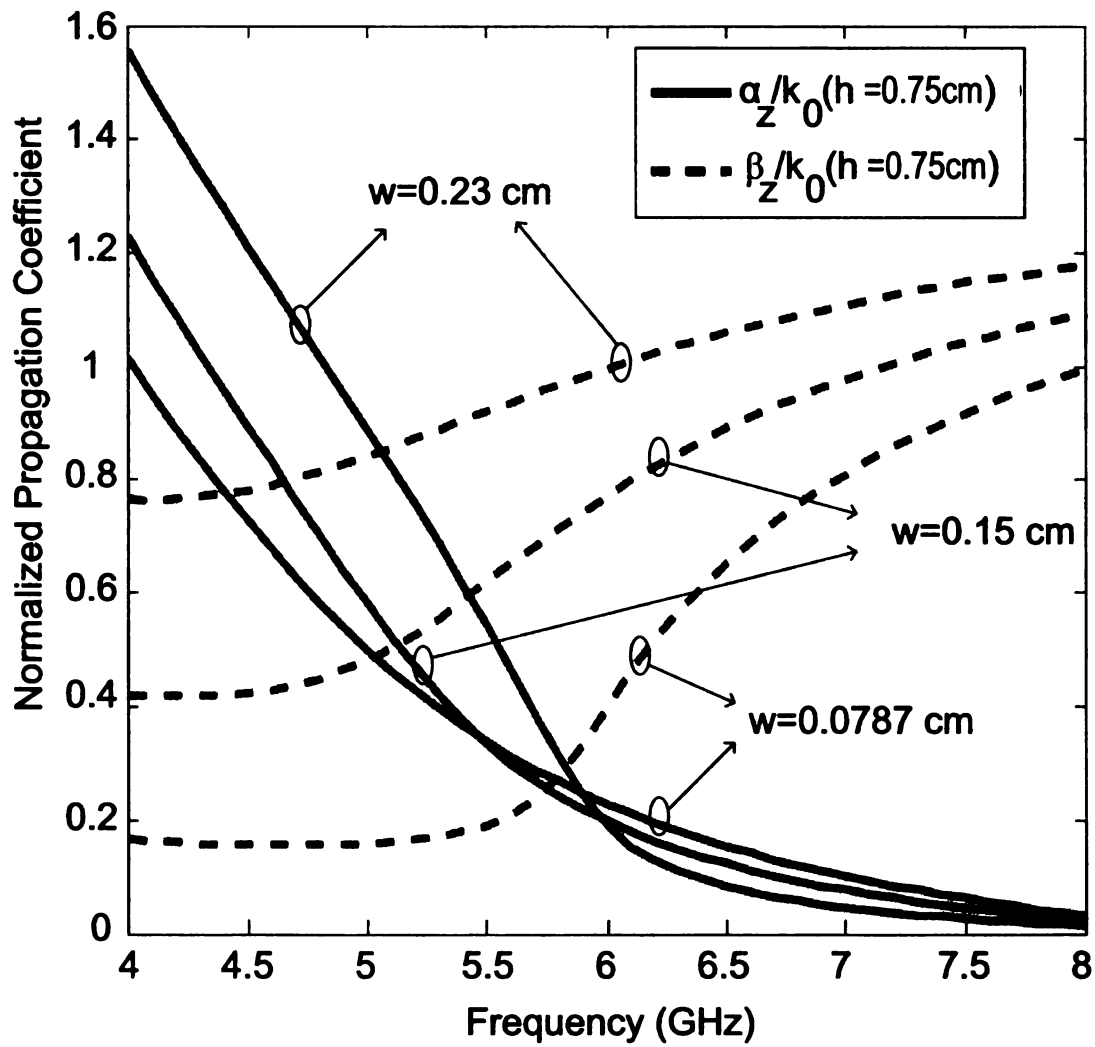


Figure 4.2. Effect of the variation of w in the propagation constants for the RT/Duroid 5880-filled TLW antenna.

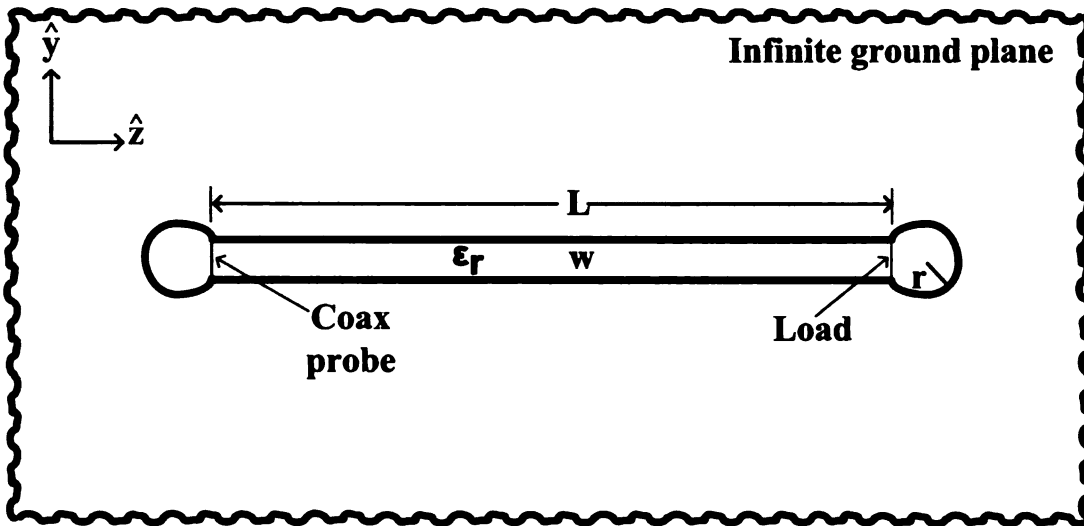
Table 4.2. RT/Duroid 5880-filled TLW antenna bandwidth for three different values of w .

w[cm]	h[cm]	Bandwidth[GHz]
0.0787	0.75	2.2
0.150	0.75	1.5
0.230	0.75	0.9

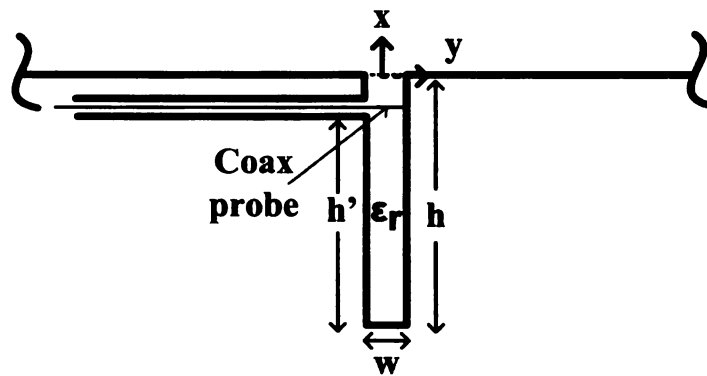
Since the TRM assumes an infinitely long antenna, in practice it is necessary to specify its length L . For this, the 90% radiated power formula, equation (1.20), is used. It is assumed that the antenna is designed for a frequency of 7 GHz. At this frequency $\alpha_z/k_0 \approx 0.03$, which means that the length is $L = 25$ cm. Finally, the terminations must be specified. There are three options considered herein: rectangular, bow-tie and circular termination (Figure 3.6). As a start point, a TLW antenna with circular shape at both ends [47] is considered (Figure 4.3). Note that this design does not require the addition of significant complexity. The design parameters are given on Table 4.3.

Table 4.3. RT/Duroid 5880-filled TLW antenna design parameters.

L[cm]	w[cm]	h[cm]	h'[cm]	r[cm]	ϵ_r	Load[Ω]
25.0	0.0787	0.75	0.60	0.3	2.33	50.0



(a)



(b)

Figure 4.3. TLW antenna with terminations and design parameters. (a)Front view. (b)Side view.

4.2 Code validation

Using the formulation given in Chapter 3, a FE-BI code is implemented in Fortran 90 [44]. This code is named *ctets*. As an initial test of the code, it is simulated the TLW antenna designed in the previous section. In order to validate the implemented code, the same design is simulated using a code provided by Dr. Kempel (*tet*). The simulation results of real and imaginary part of the input impedance are shown on Figure 4.4 and Figure 4.5 respectively. It is interesting to notice the oscillations around $F = 7.5$ GHz in the real and imaginary parts of the input impedance. This means that a backward wave traveling in opposite direction ($-z$) starts to impact significantly the antenna performance above this frequency.

The front-to-back ratio is defined as the difference between the forward and the backward lobe on a decibel basis. In leaky wave antennas this ratio is important because it is desired to optimize the radiation in the forward direction (i.e., $0^\circ < \theta < 90^\circ$). This optimization can be achieved using a termination load to reduce the reflection wave at the antenna end. In addition, a further improvement is achieved designing circular shaped baluns for the TLW antenna (Figure 4.3). The radiation pattern at $F = 8.0$ GHz is shown on Figure 4.6. The load and baluns partially reduce the reflected wave (front-to-back ratio of approximately 20 dB).

In general, the simulations shown on Figure 4.4, Figure 4.5, and Figure 4.6 validate the results provided by the code developed in this work (*ctets*). The input impedance and the radiation pattern results obtained using *tet* and *ctets* agree excellently.

The VSWR for the RT/Duroid 5880-filled TLW antenna is shown on Figure 4.7.

Defining the impedance bandwidth for a VSWR less than 2 as the percentage of the frequency difference (upper minus lower) over the center frequency of the bandwidth [48]. The simulated bandwidth for the RT/Duroid 5880-filled TLW antenna is 15.71%.

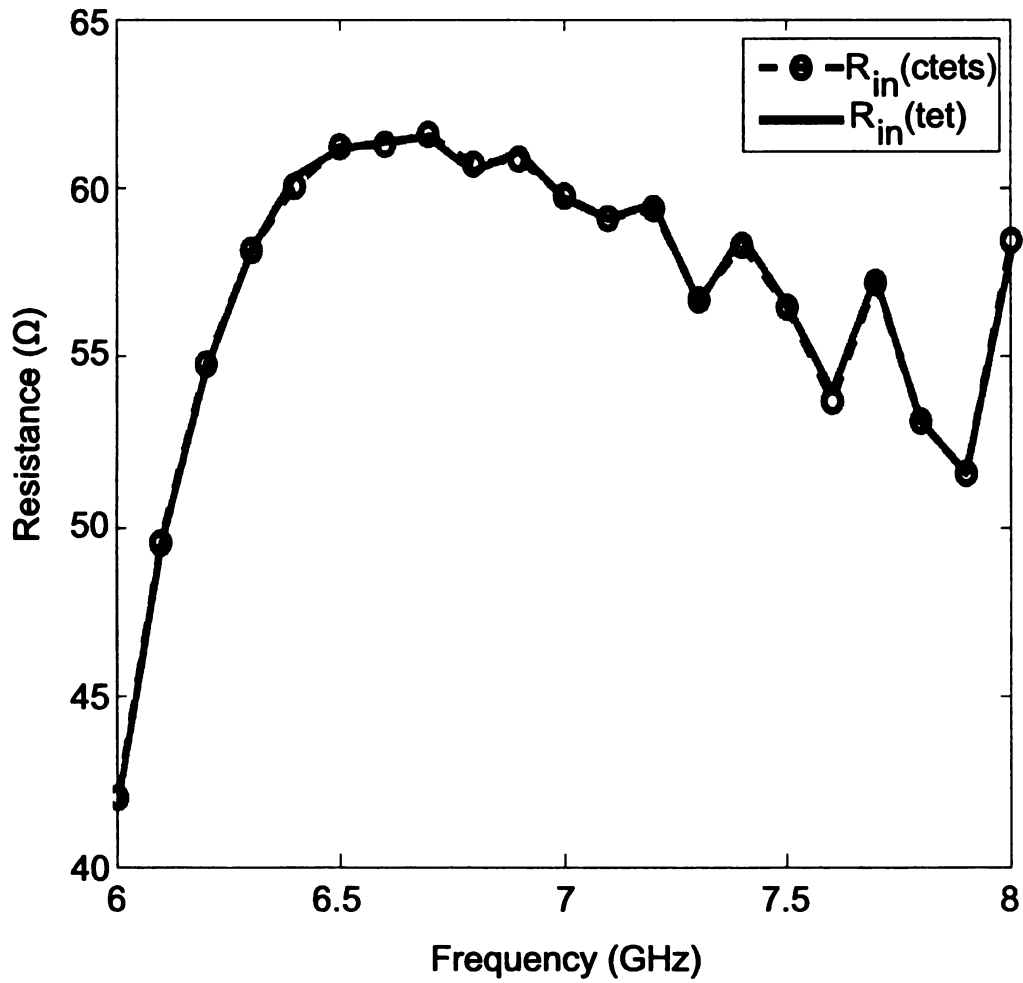


Figure 4.4. Real part of the input impedance of the RT/Duroid 5880-filled TLW antenna simulated using ctets and tet.

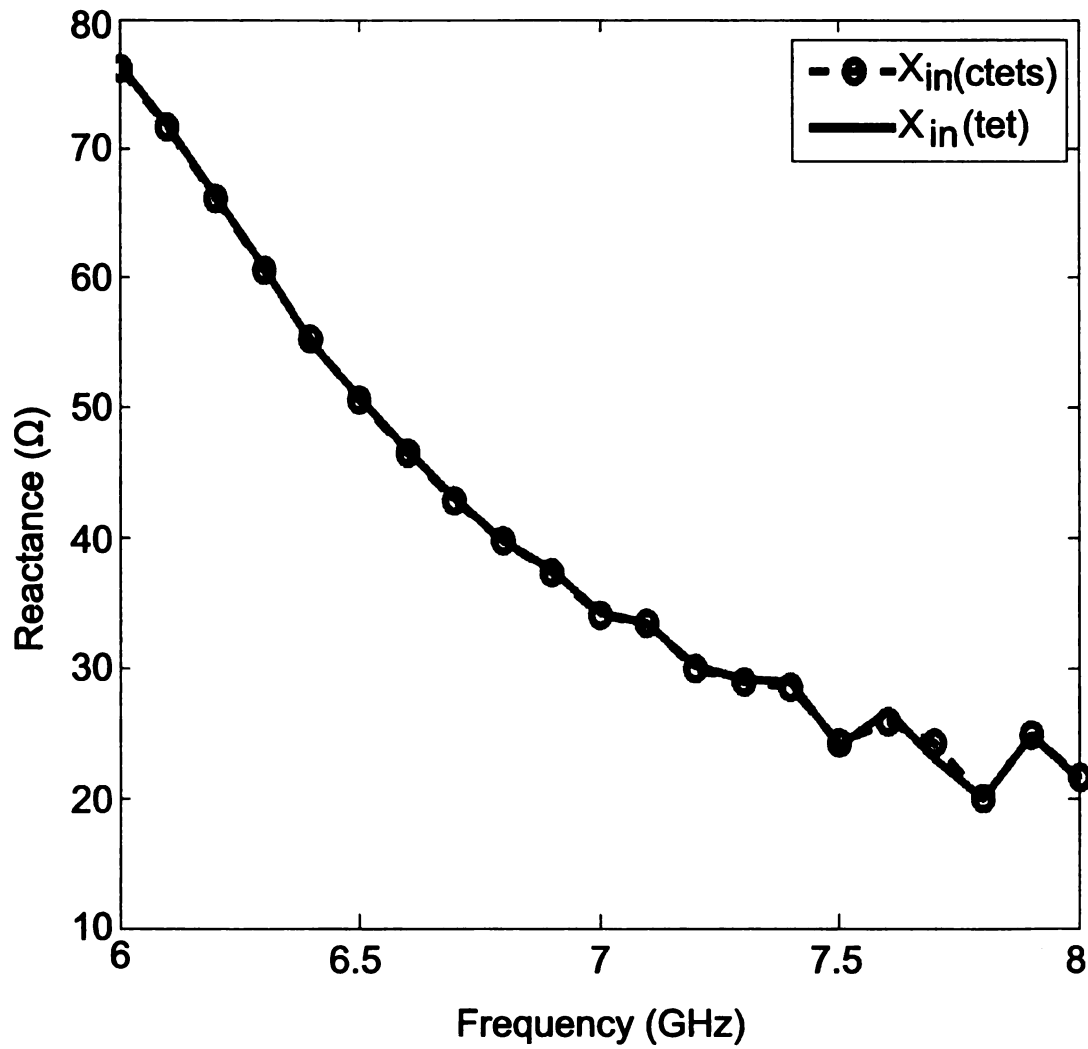


Figure 4.5. Imaginary part of the input impedance of the RT/Duroid 5880-filled TLW antenna simulated using ctets and tet.

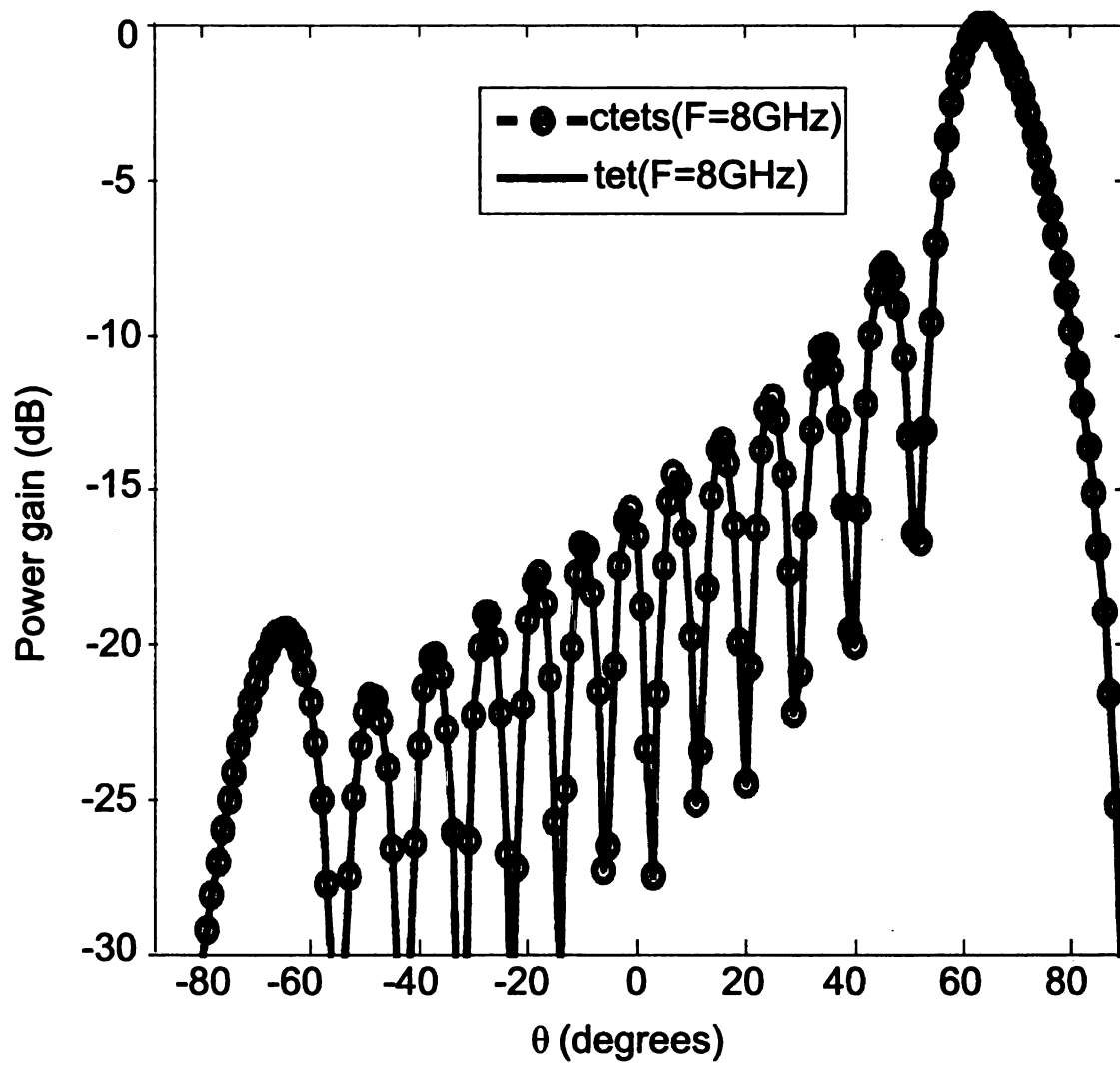


Figure 4.6. Radiation pattern at $F=8.0$ GHz of the RT/Duroid 5880-filled TLW antenna simulated using ctets and tet.

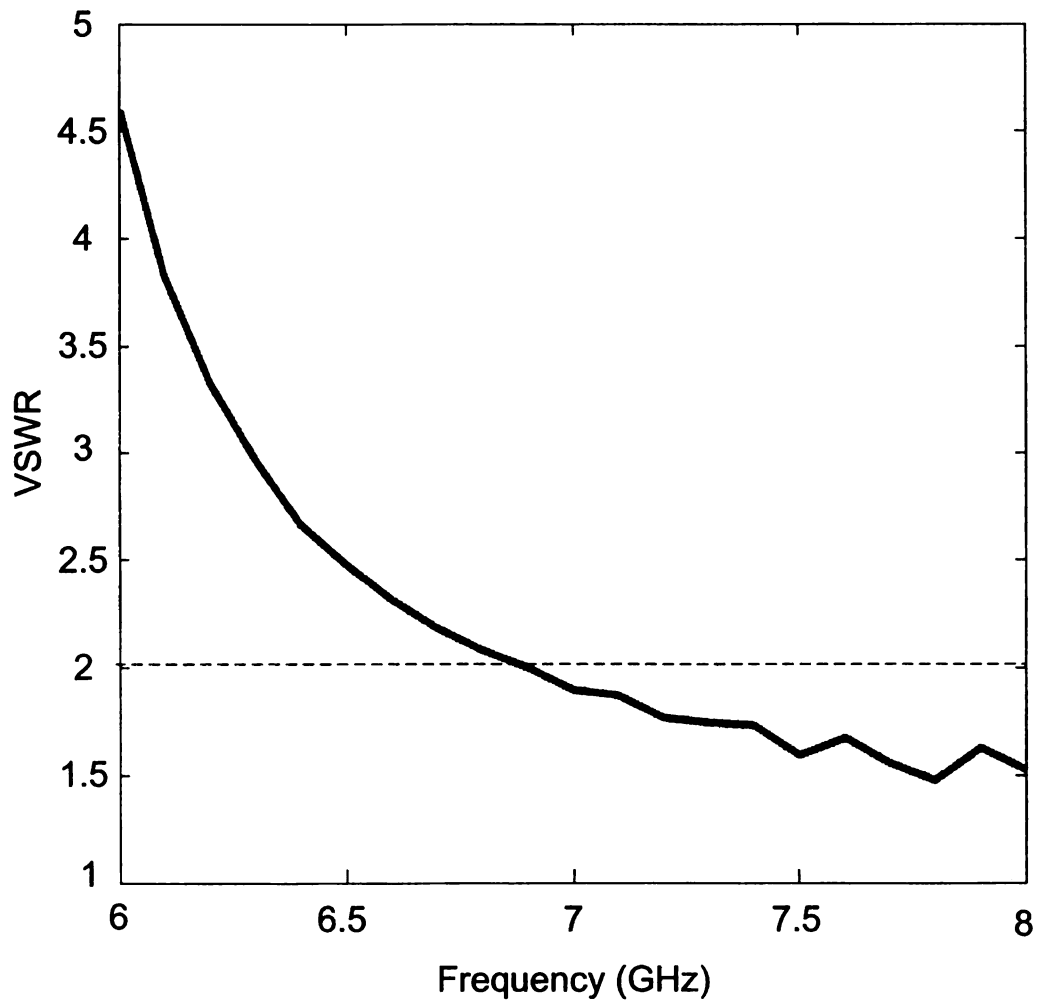


Figure 4.7. VSWR of the RT/Duroid 5880-filled TLW antenna.

Other important parameters that can be studied to evaluate the behavior of this antenna are the tangential electric field in the aperture of the trough (E_y) and the propagation constant ($k_z = \beta_z - j\alpha_z$). E_y is computed from the values of the expansion coefficients on each edge (in the y direction) along the aperture. Its magnitude is shown on Figure 4.8. At $F = 6.0$ GHz, it is evident the exponential decay of the field magnitude ($|E_y|$) with the distance. Oscillations of the field are significant at $F = 8.0$ GHz (Figure 4.8). The phase at three different frequencies ($F = 6.0$, $F = 7.0$, and $F = 8.0$) is shown on Figure 4.9, Figure 4.10, and Figure 4.11, respectively.

The propagation constant is computed using FE-BI and the least square method described on subsection 3.7.6.3, in particular equations (3.159) and (3.160) are used to compute the slope and the independent term respectively. Also, this information is shown on Figure 4.12, Figure 4.13 and the ratio of these two on Figure 4.14. The propagation constant results are compared with the ones of the TRM (Figure 4.15). Even though TRM is an approximation, the agreement with FE-BI is reasonable.

In addition, it is possible to check the accuracy of equation (1.16) given in Chapter 1. From Figure 4.15 $\beta_z/k_0 = 0.92$ at $F = 8.0$ GHz, using (1.16), the maximum radiation is at $\theta = 66^\circ$ which agrees the maximum value of the beam shown on Figure 4.6.

4.3 Air-filled TLW antenna

In Chapter 2, using the TRM it was proved that, in theory, the air-filled TLW antenna have an infinite operation bandwidth (Figure 2.6). That is, β_z/k_0 never reaches a value equal to unity. This is the reason to design and fabricate the air-filled TLW antenna in this dissertation. The design procedure is similar to that given in section

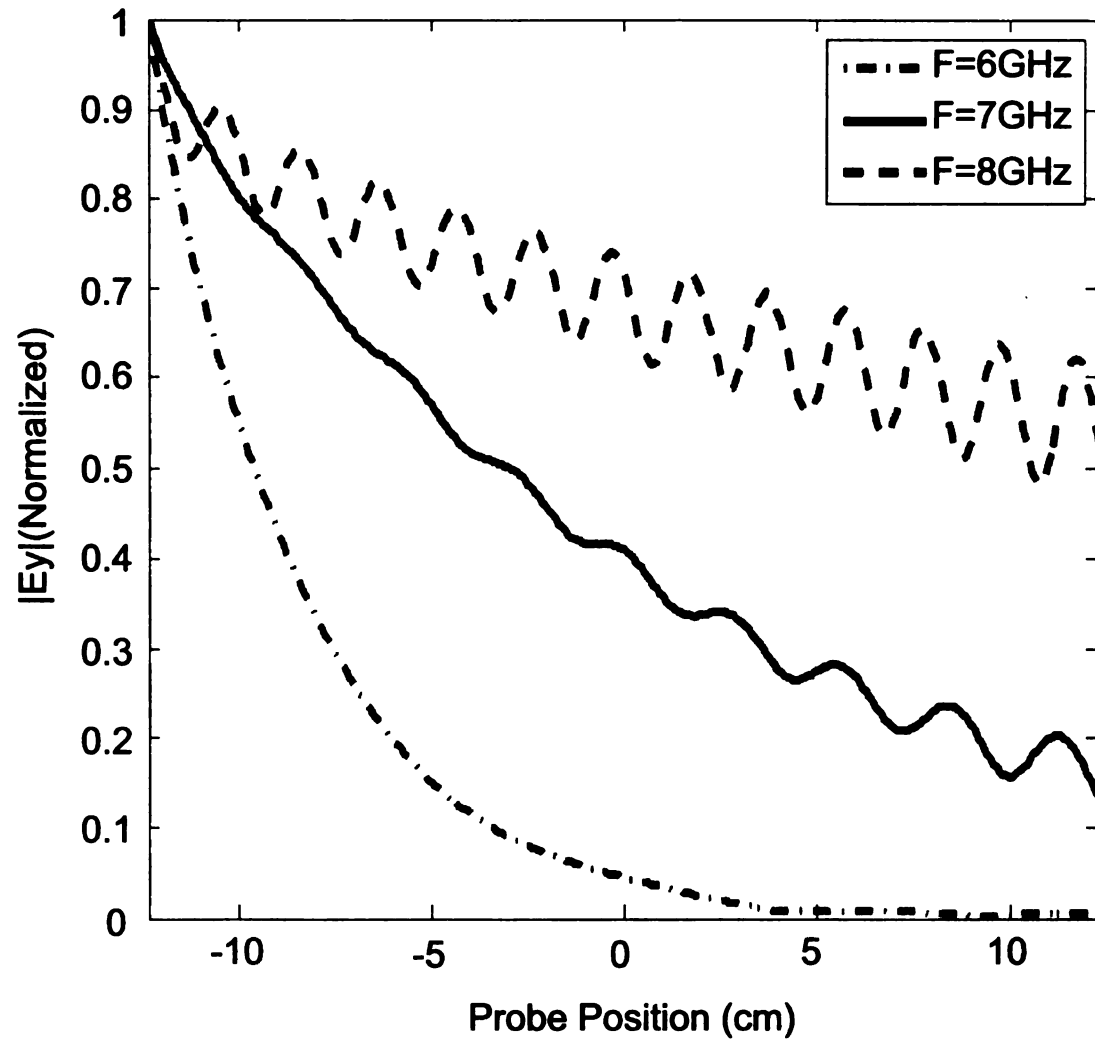


Figure 4.8. Magnitude of E_y of the RT/Duroid 5880-filled TLW antenna.

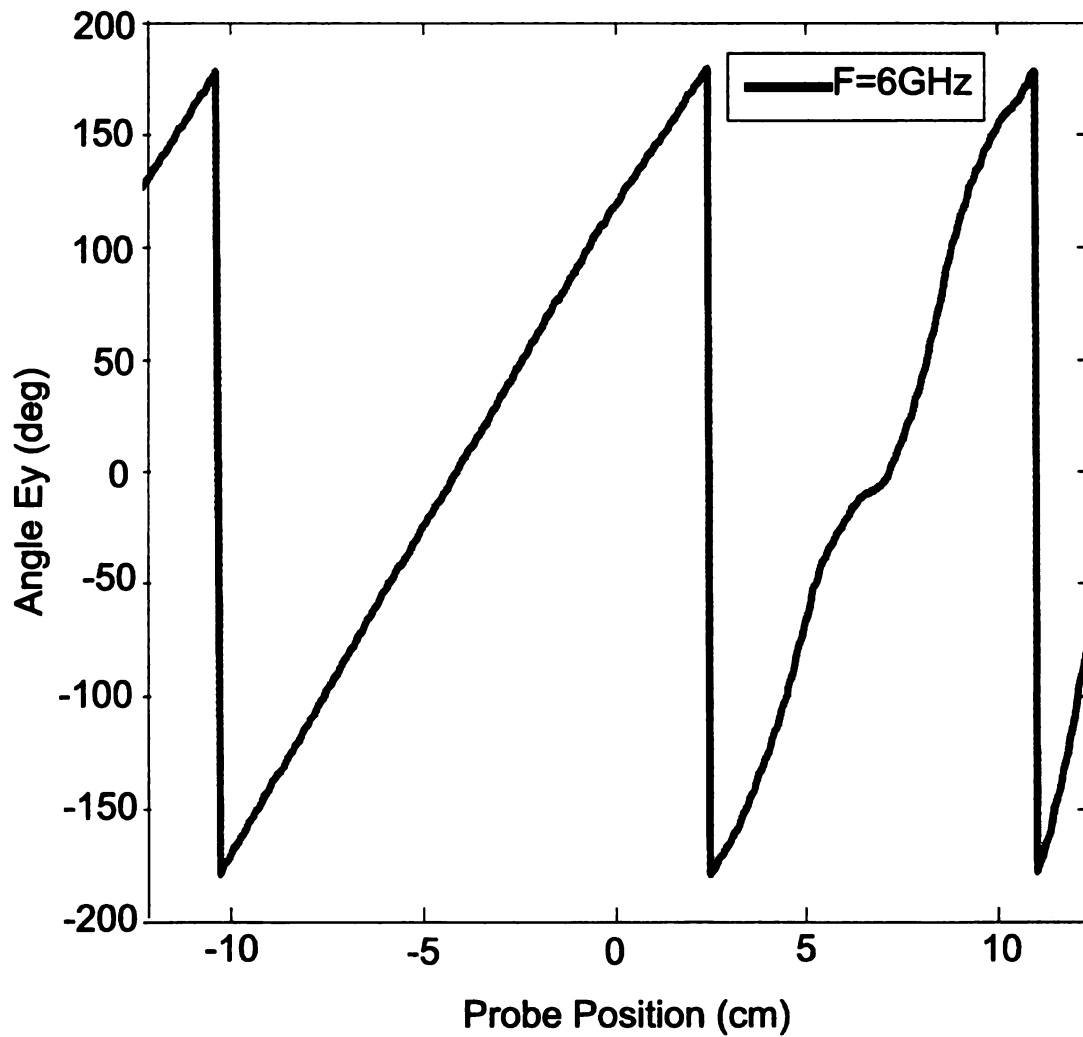


Figure 4.9. Phase of E_y at 6 GHz of the RT/Duroid 5880-filled TLW antenna.

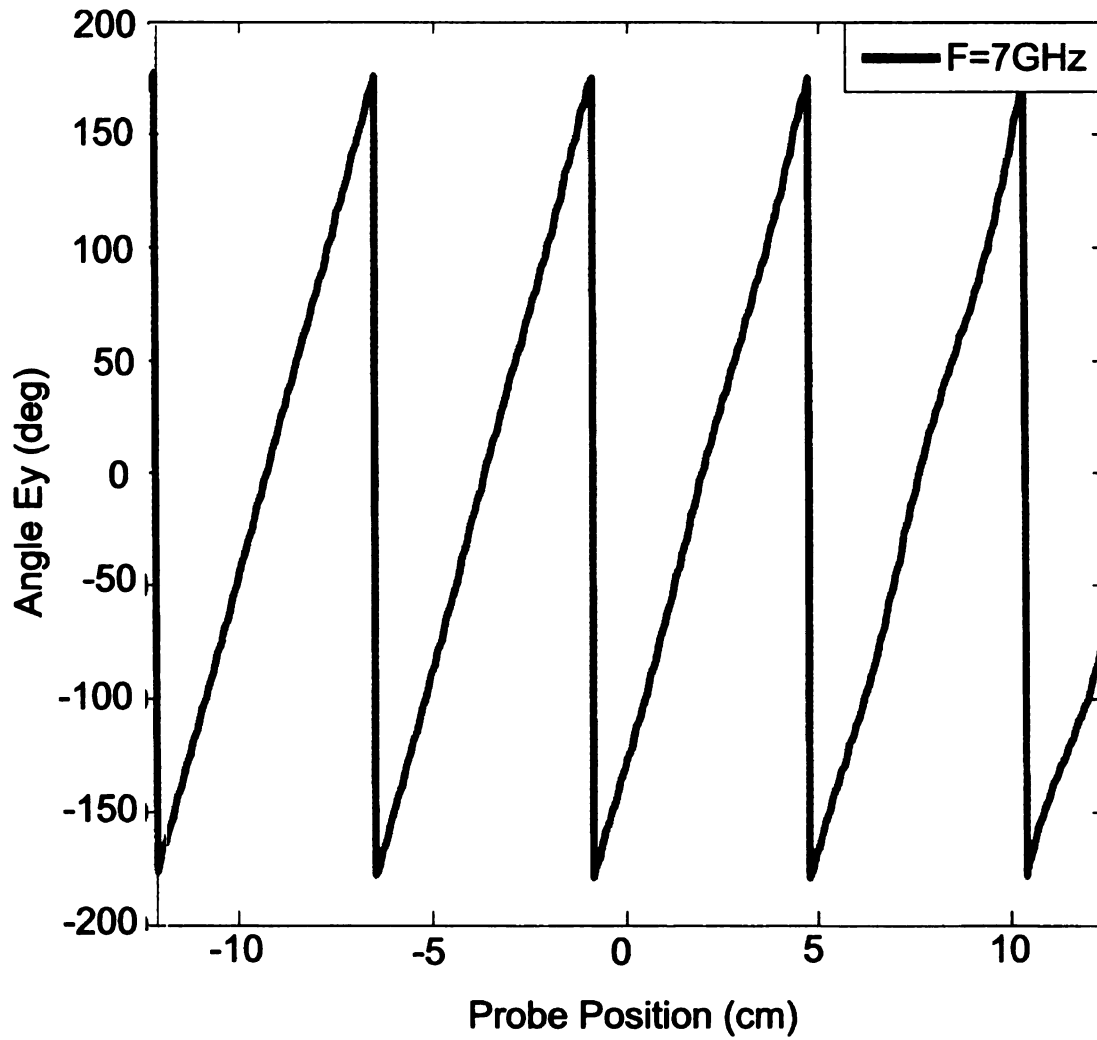


Figure 4.10. Phase of E_y at 7 GHz of the RT/Duroid 5880-filled TLW antenna.

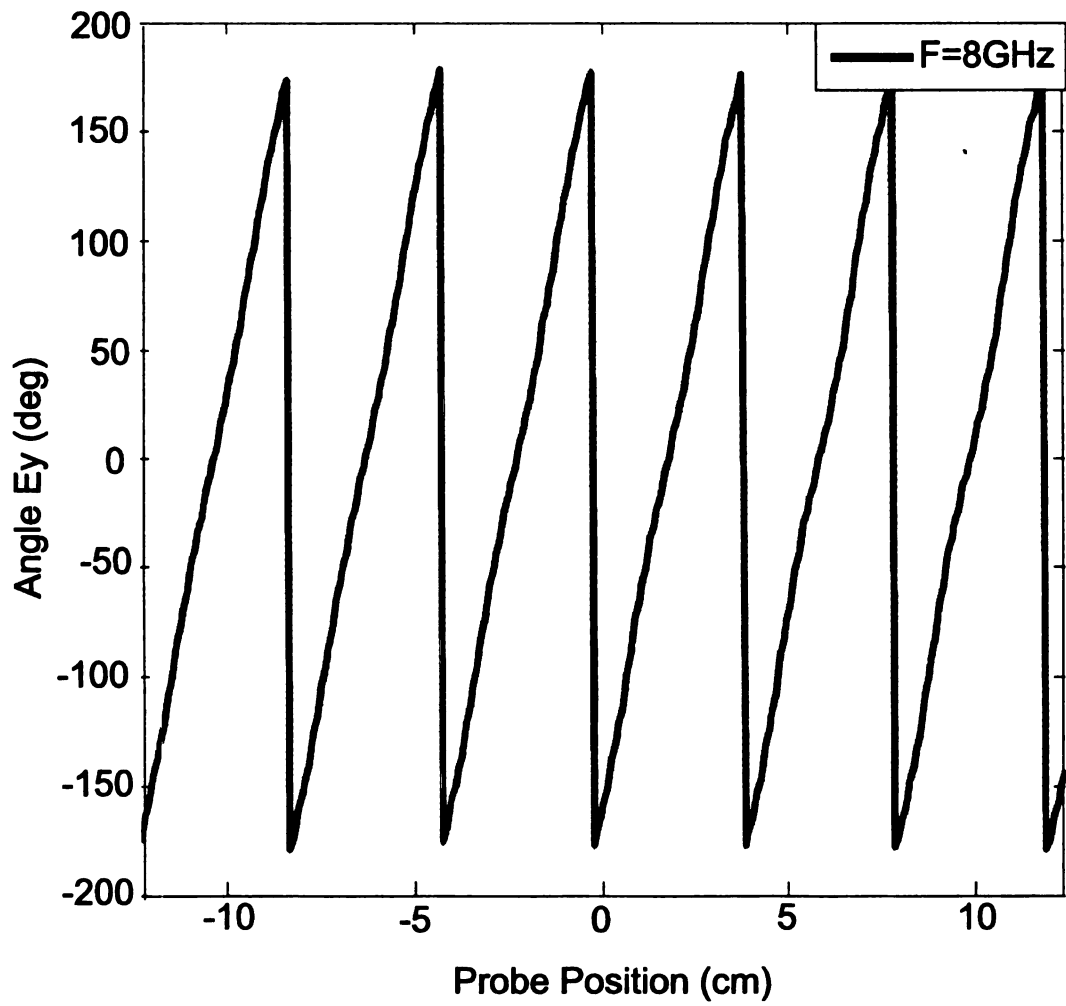


Figure 4.11. Phase of E_y at 8 GHz of the RT/Duroid 5880-filled TLW antenna.

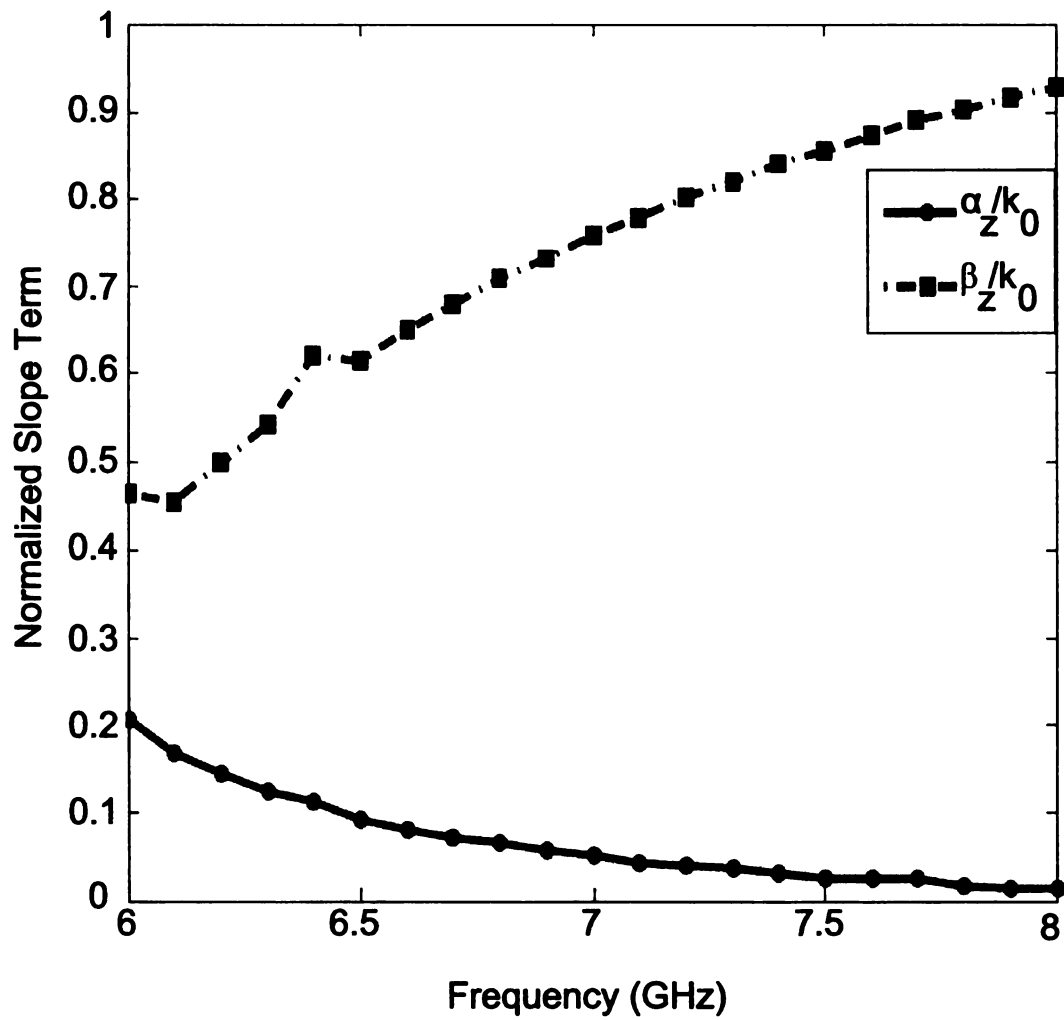


Figure 4.12. Slope term computed via FE-BI and the least square method.

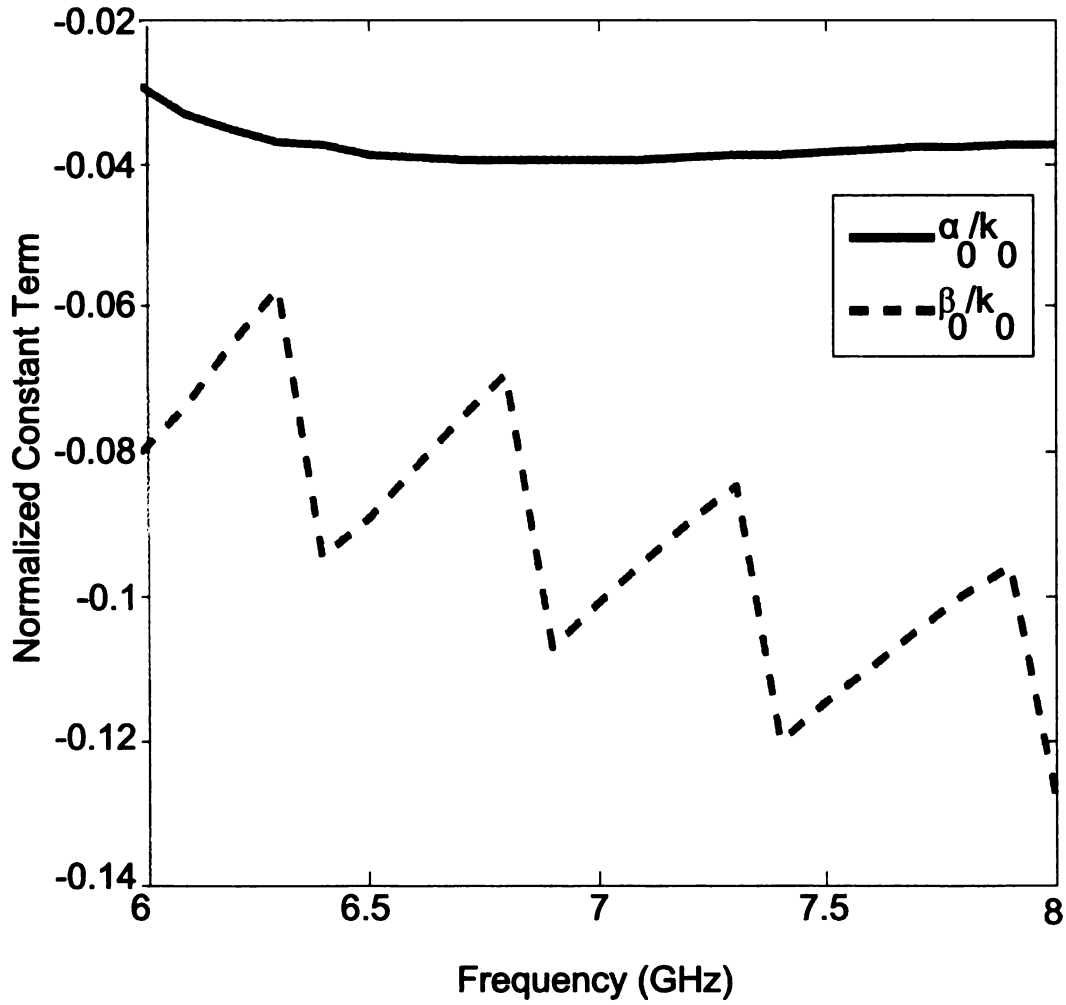


Figure 4.13. Constant term computed via FE-BI and the least square method.

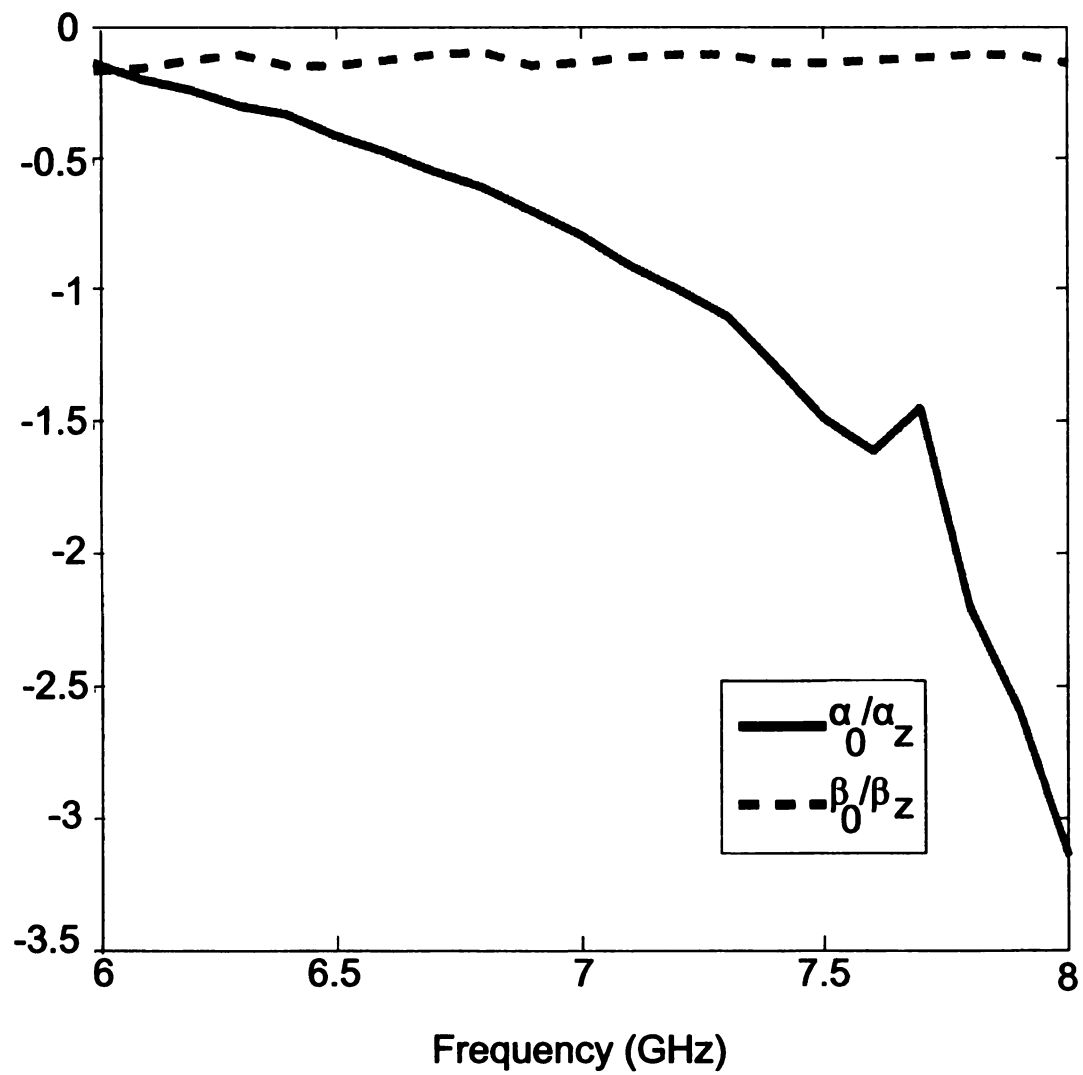


Figure 4.14. Ratio constant to slope term computed via FEBI and least square method.

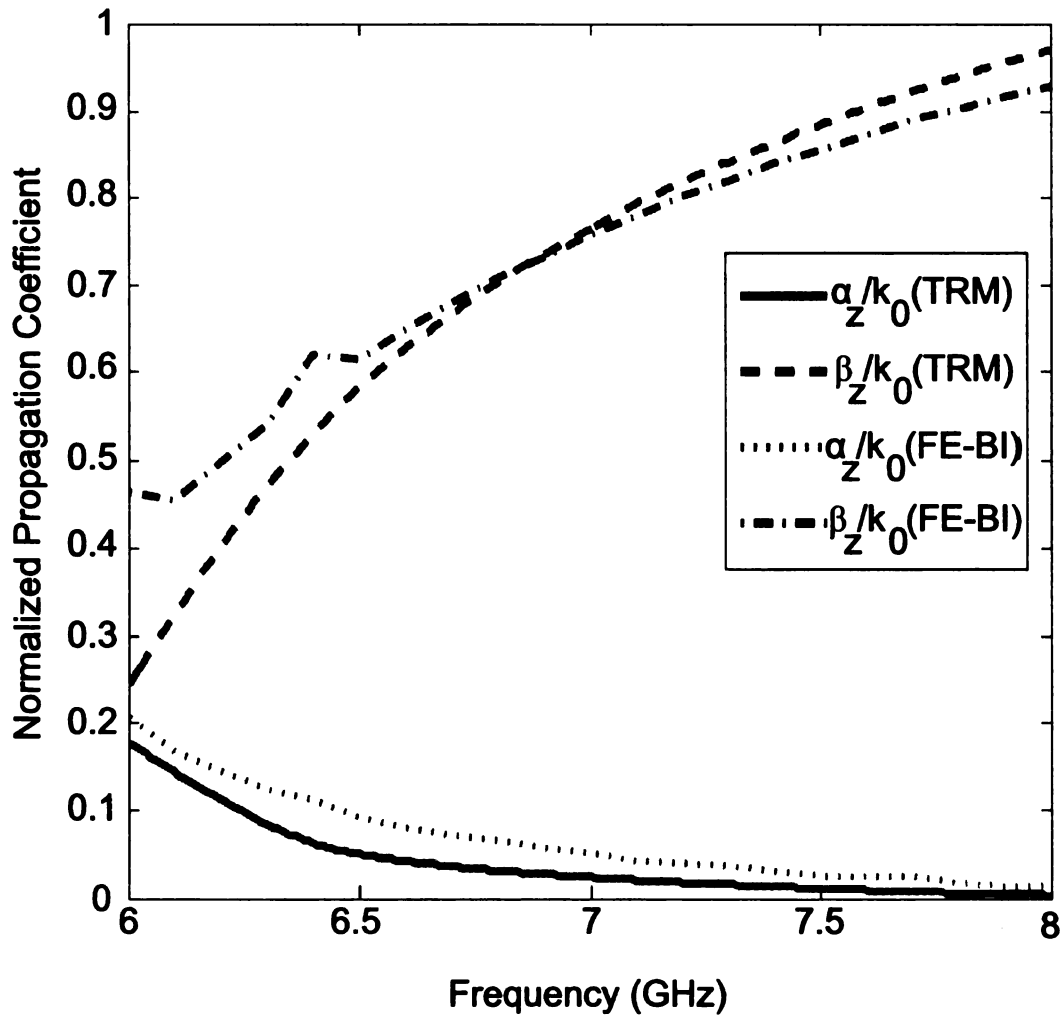


Figure 4.15. Propagation constant of the RT/Duroid 5880-filled TLW antenna computed using FE-BI and TRM.

4.1. It starts using the TRM to compute the propagation constants for different values of h and w . Figure 4.16 shows the effect of three different values of h in the propagation constants while w is kept constant. Similarly, Figure 4.17 shows the effect in these parameters for different values of w while h is kept constant. From these two figures the greatest bandwidth value happens for $w = 0.2361$ cm and $h = 1.4$ cm.

The next step in the TLW antenna design is to specify the antenna length using the 90% radiated power formula, equation (1.20). It is assumed that the antenna is designed for a frequency of 12 Ghz. At this frequency $\alpha_z/k_0 \approx 0.018$ (Figure 4.17), which means that the length is $L = 25$ cm. The design parameters are summarized on Table 4.4

Table 4.4. Air-filled TLW antenna design parameters.

L[cm]	w[cm]	h[cm]	h'[cm]	ϵ_r	Load[Ω]
25.0	0.2361	1.4	1.2	1.0	50.0

In order to optimize this design several terminations are considered. The rectangular, the bow-tie and the circular termination are simulated using FE-BI. Figure 4.18 shows these terminations; the points $a - b$ and $a' - b'$ denote the position for the coaxial feed and load respectively. The rectangular termination has six degrees of freedom (DF). ($L, w, \epsilon_r, \rho, h$ and h'). The bow-tie has seven DF ($L, w, \epsilon_r, \rho, \theta, h$ and h'). The circular termination has six DF (L, w, ϵ_r, r, h and h'). The FE-BI simulation results have shown that the circular termination has the best response in terms of

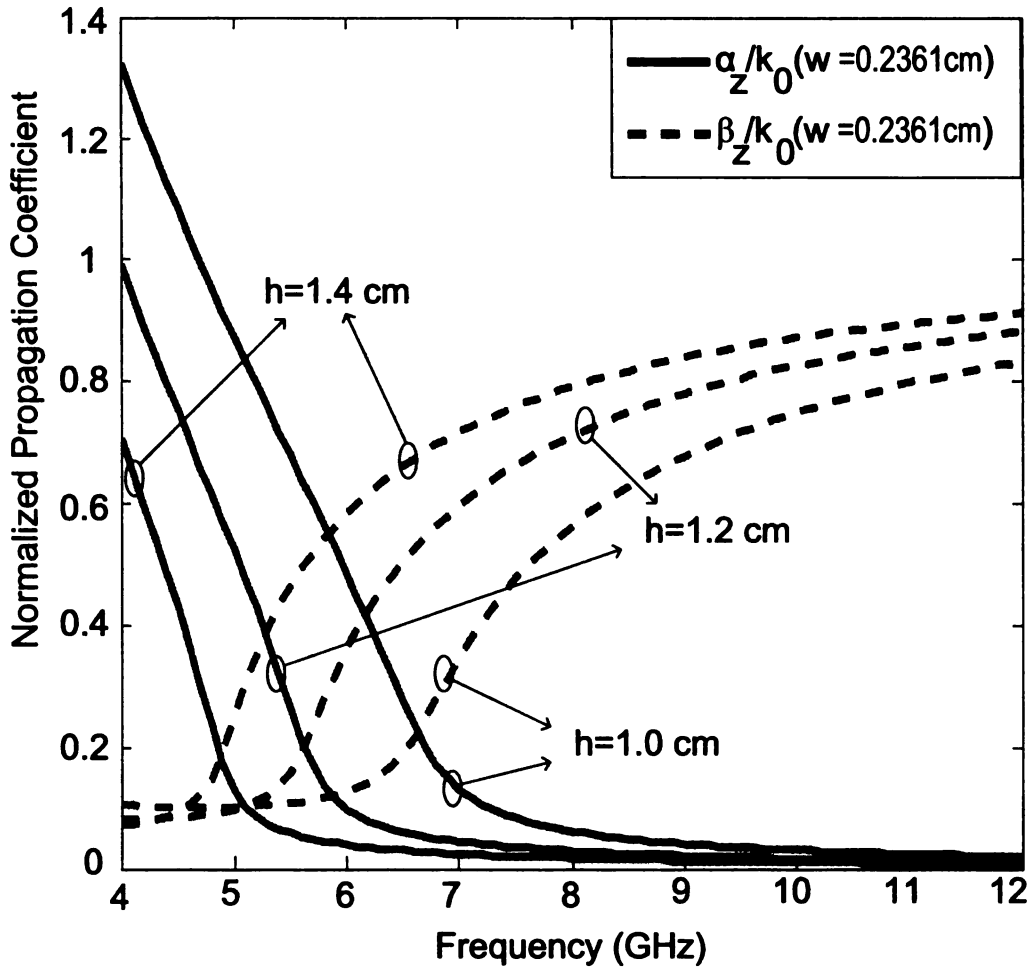


Figure 4.16. Effect of the variation of h in the propagation constants for the air-filled TLW antenna.

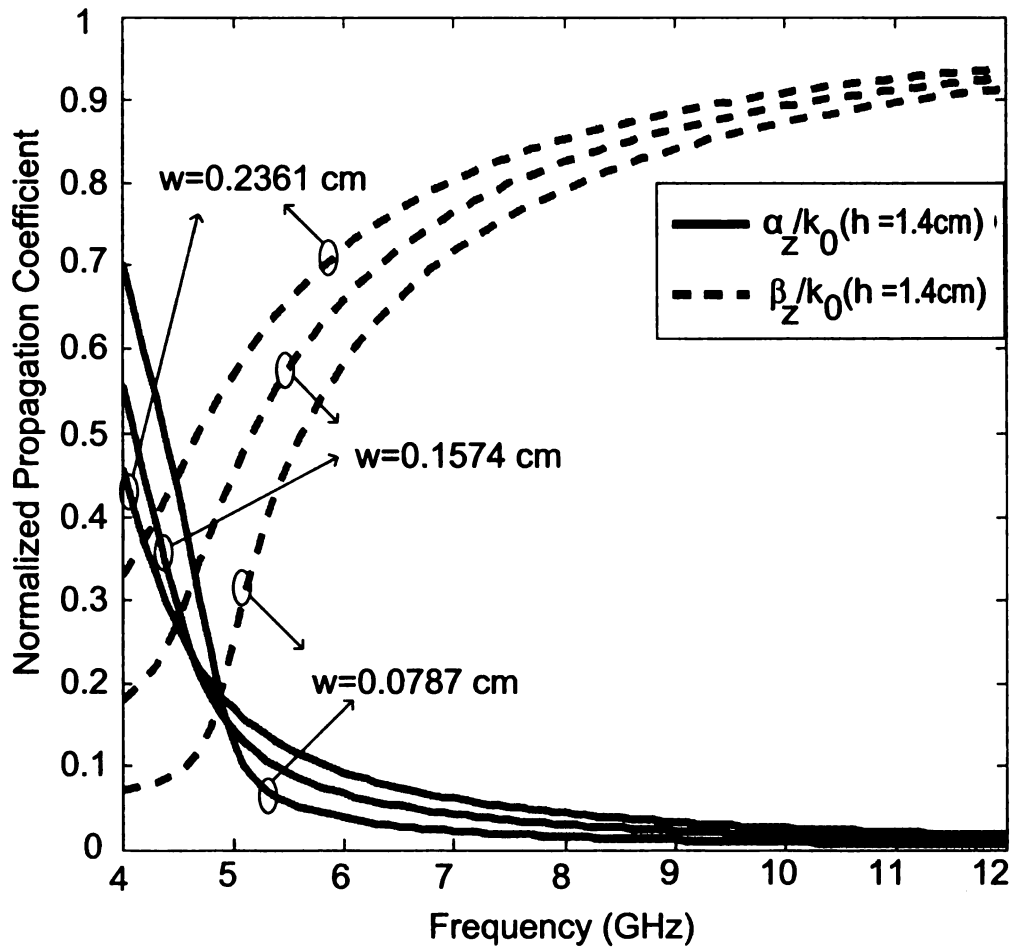


Figure 4.17. Effect of the variation of w in the propagation constants for the air-filled TLW antenna.

VSWR (Figure 4.19) and front to back ratio (Figure 4.20) of all three terminations. The antennas with the rectangular and bow-tie terminations have a front to back ratio of ≈ 15 dB whereas the circular termination case has one of ≈ 20 dB. The circular termination parameters are shown on Table 4.5.

The input impedance bandwidth for the circular case is 40% (Figure 4.19) and the front to back ratio is 20 dB (Figure 4.20). The input impedance for the circular case is shown on Figure 4.21. Similarly to the RT/Duroid 5880 filled case, this input impedance is dispersive along operational bandwidth. The behavior of the tangential component of the electric field (E_y) along the antenna aperture is shown on Figure 4.22 through Figure 4.25. It is clear the exponential behavior of this field at low frequencies whereas at high frequencies (9-12 GHz) standing waves start to appear along the aperture. The propagation constants computed using TRM and FE-BI are shown on Figure 4.26. The agreement between these two methods is reasonable.

The efficiency of the TLW antenna with circular termination is shown on Figure 4.27. The maximum efficiency happens at 12 GHz and is about 75%. The ratio P_{in}/P_{RL} for the TLW antenna with circular termination is shown on Figure 4.28, where P_{RL} is computed using (3.154). The maximum power absorbed by the load impedance is 3.7% at 12 GHz.

Table 4.5. Air-filled TLW antenna circular termination design parameters.

L[cm]	w[cm]	h[cm]	h'[cm]	ϵ_r	r[cm]	Load[Ω]
25.0	0.2361	1.4	1.2	1.0	0.3	50.0

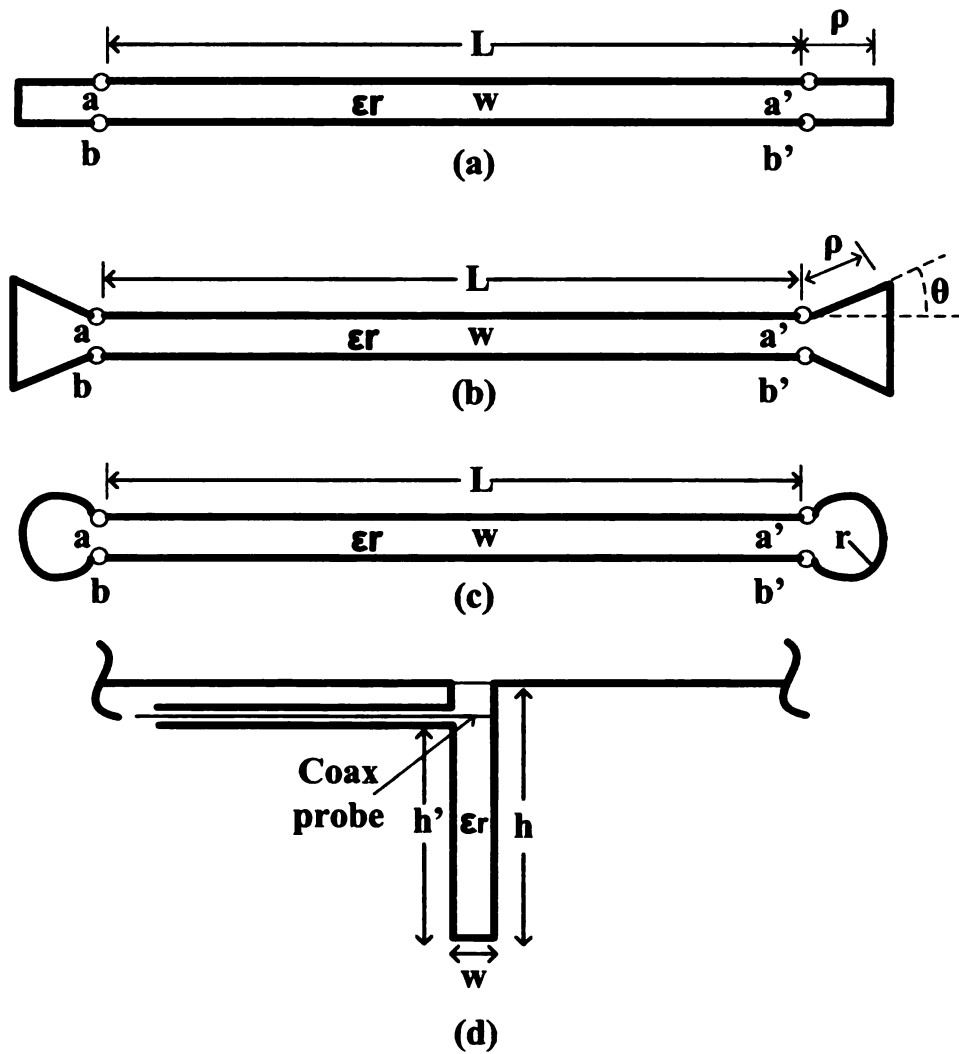


Figure 4.18. Different terminations: (a)Rectangular (b)Bow-tie (c)Circular (d)Side view.

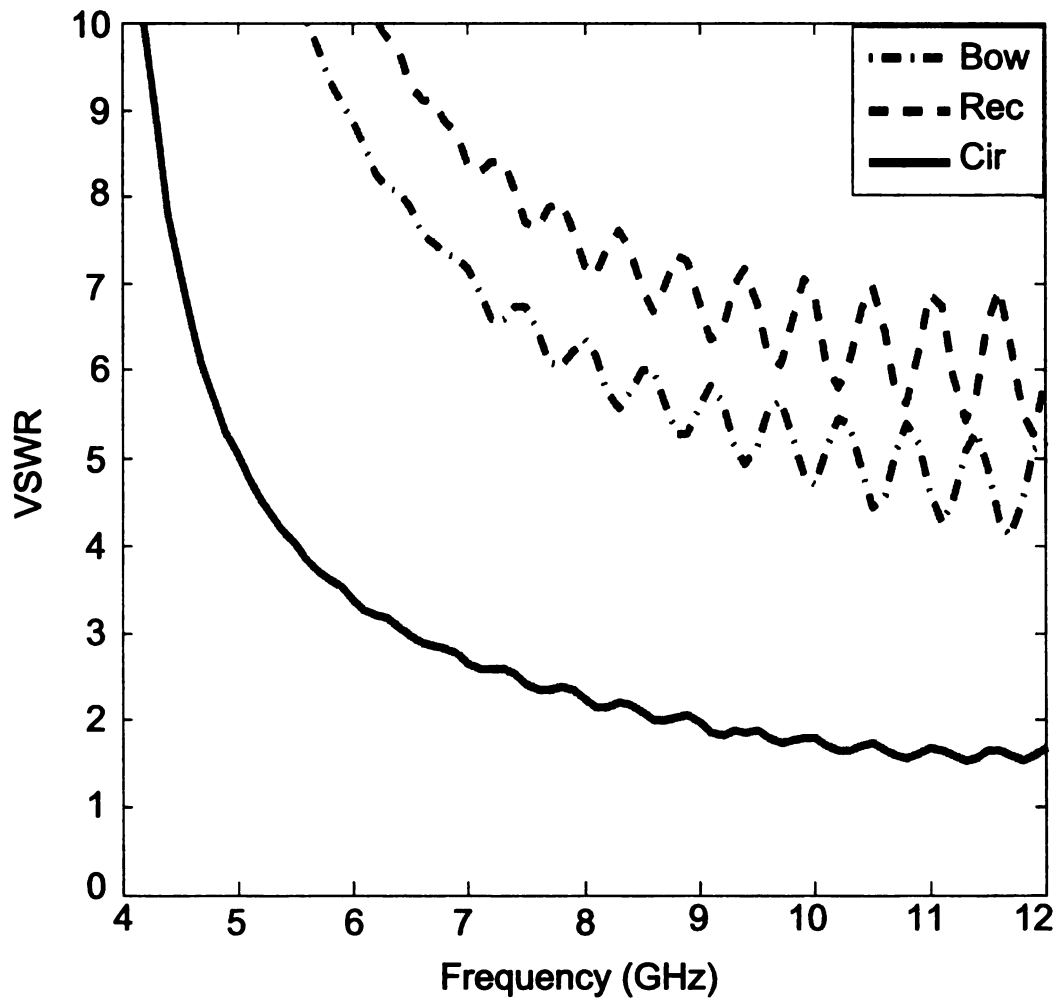


Figure 4.19. VSWR for the air filled TLW antenna with different terminations.

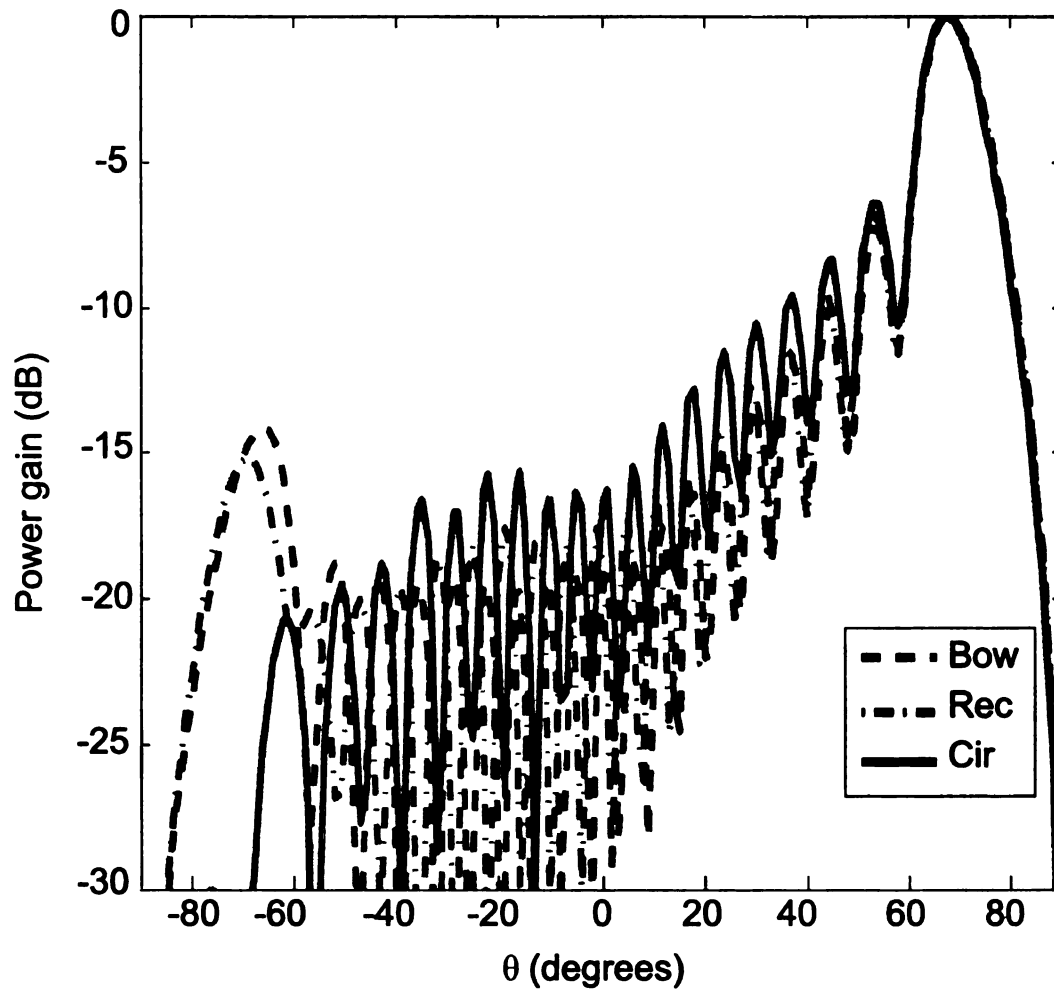


Figure 4.20. Radiation pattern at 12 GHz for the air filled TLW antenna with different terminations.

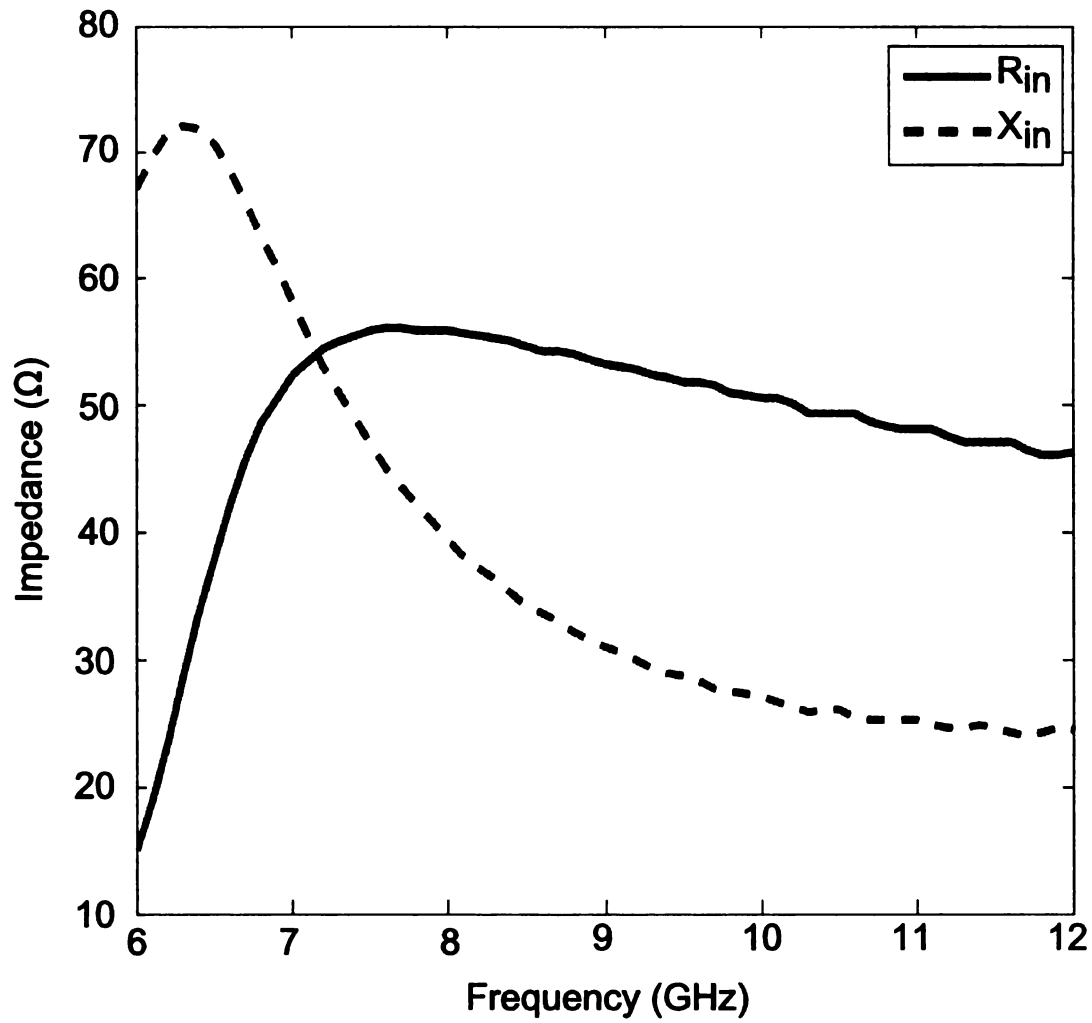


Figure 4.21. Input impedance of the air-filled TLW antenna with circular termination.

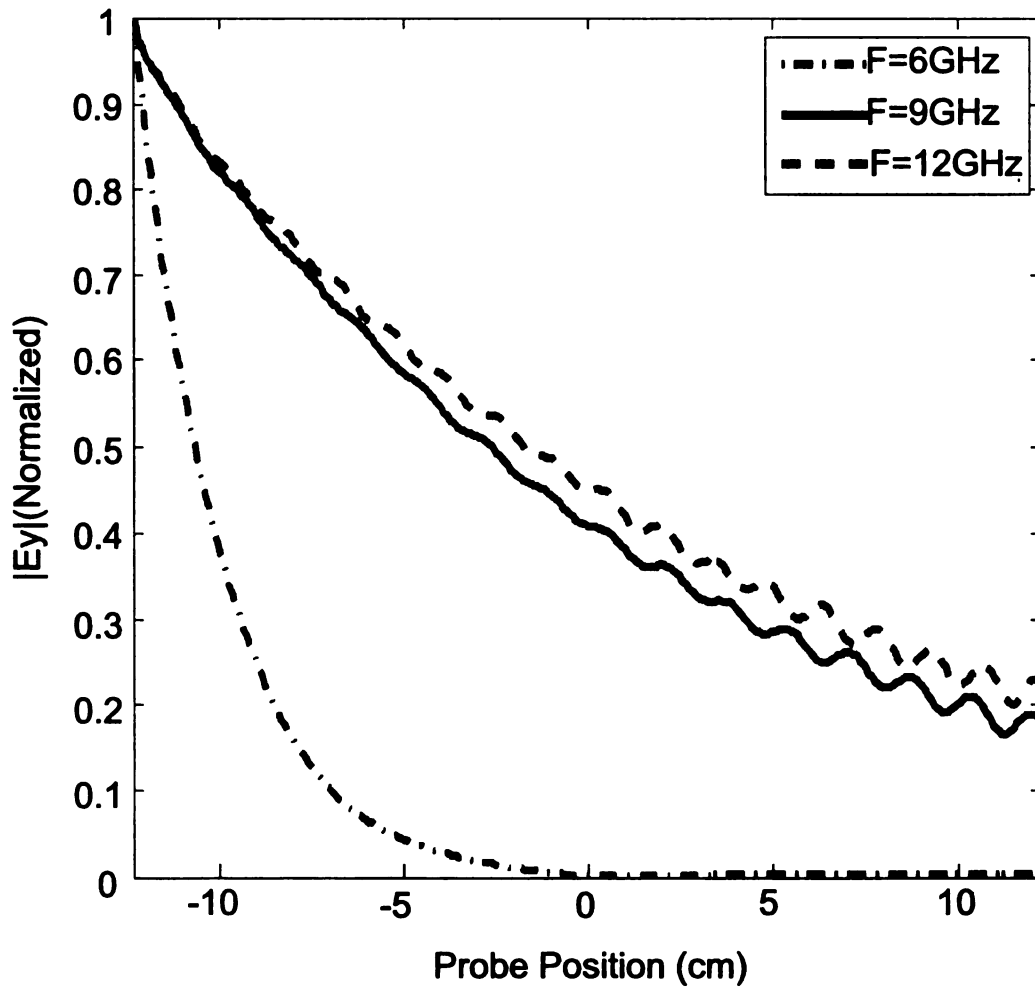


Figure 4.22. Magnitude of E_y of the air-filled TLW antenna with circular termination.

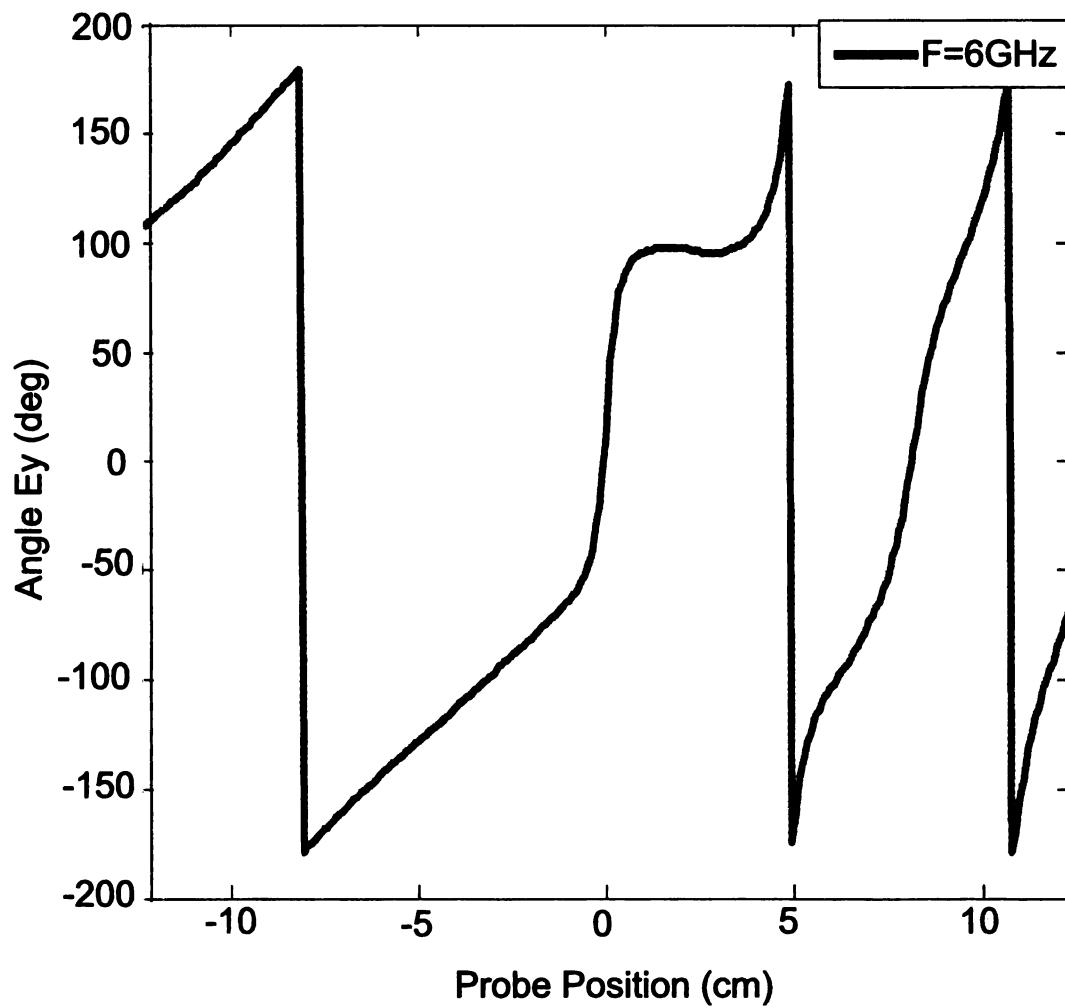


Figure 4.23. Phase of E_y at 6 GHz of the air-filled TLW antenna with circular termination.

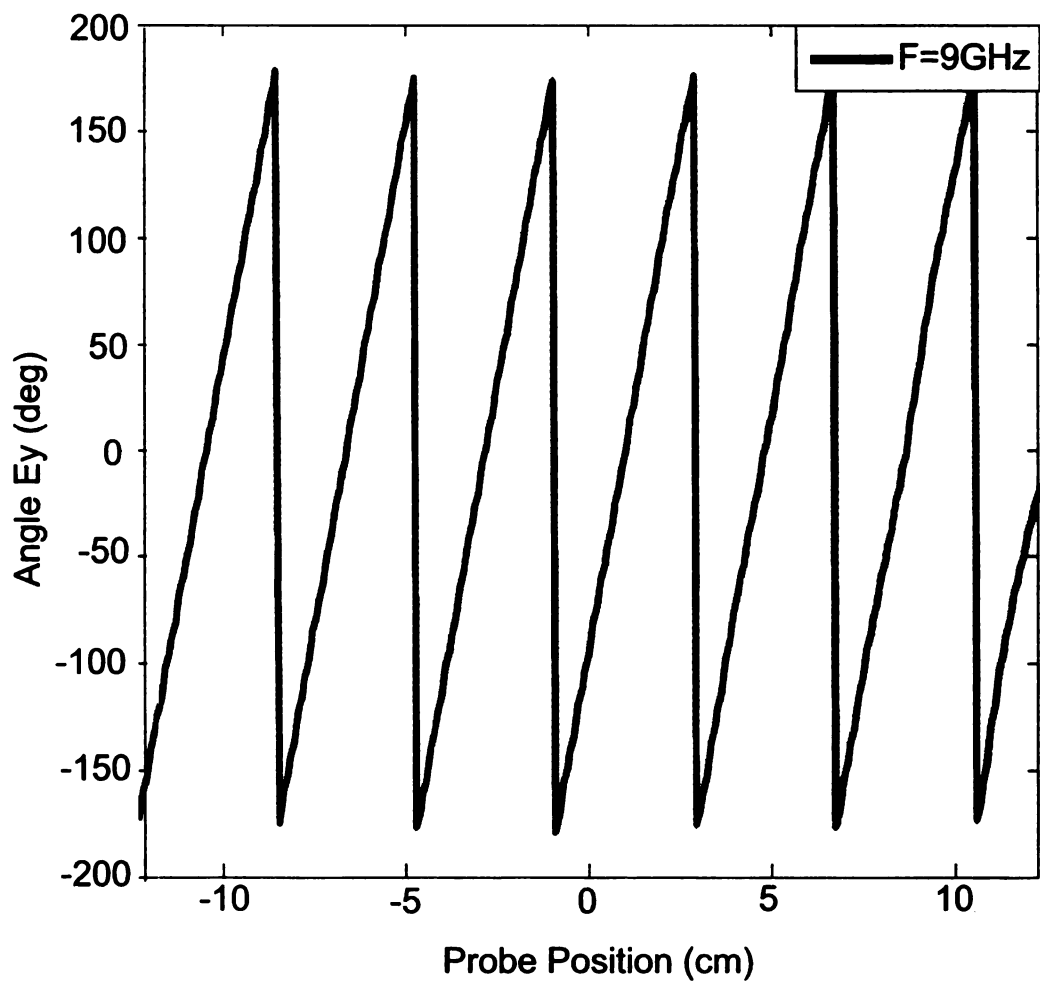


Figure 4.24. Phase of E_y at 9 GHz of the air-filled TLW antenna with circular termination.

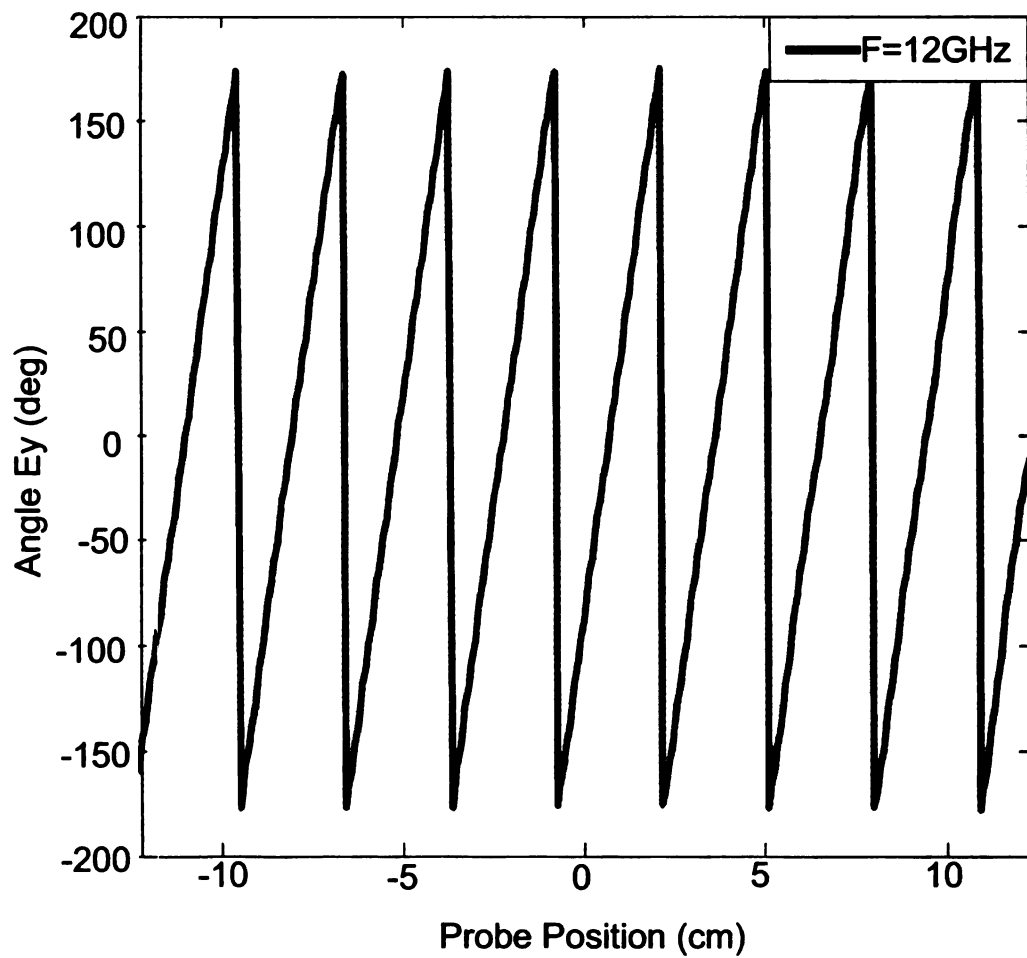


Figure 4.25. Phase of E_y at 12 GHz of the RT/Duroid 5880-filled TLW antenna with circular termination.

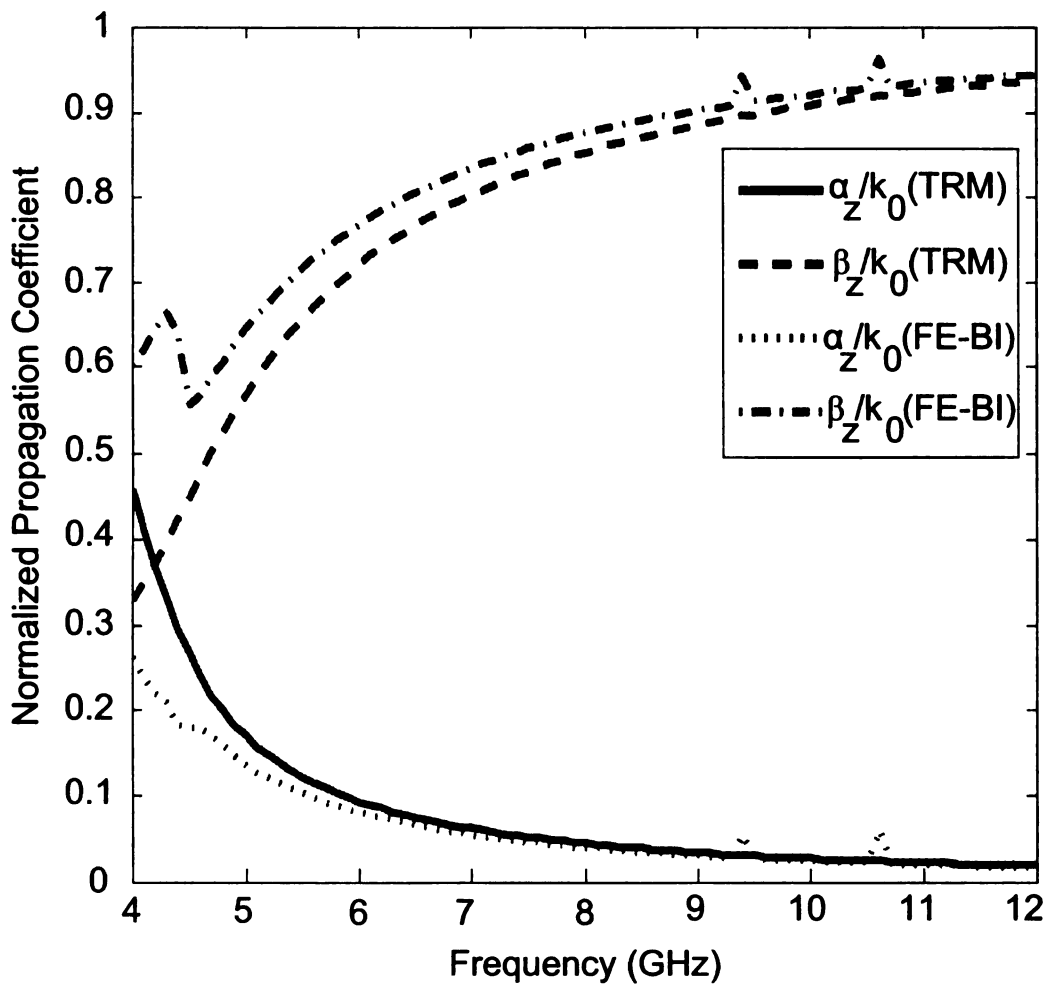


Figure 4.26. Propagation constant of the air filled TLW antenna with circular termination.

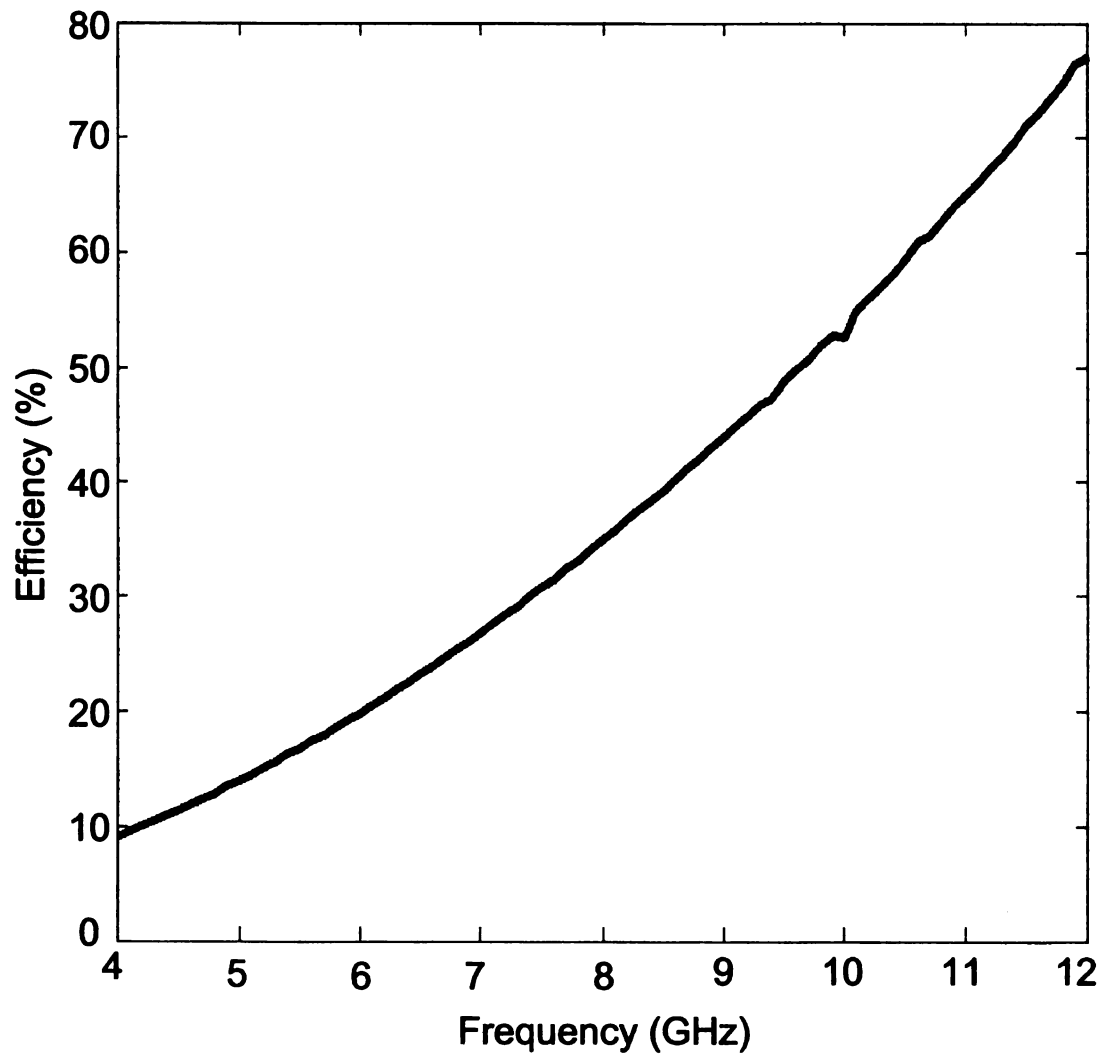


Figure 4.27. Efficiency of the TLW antenna with circular termination.

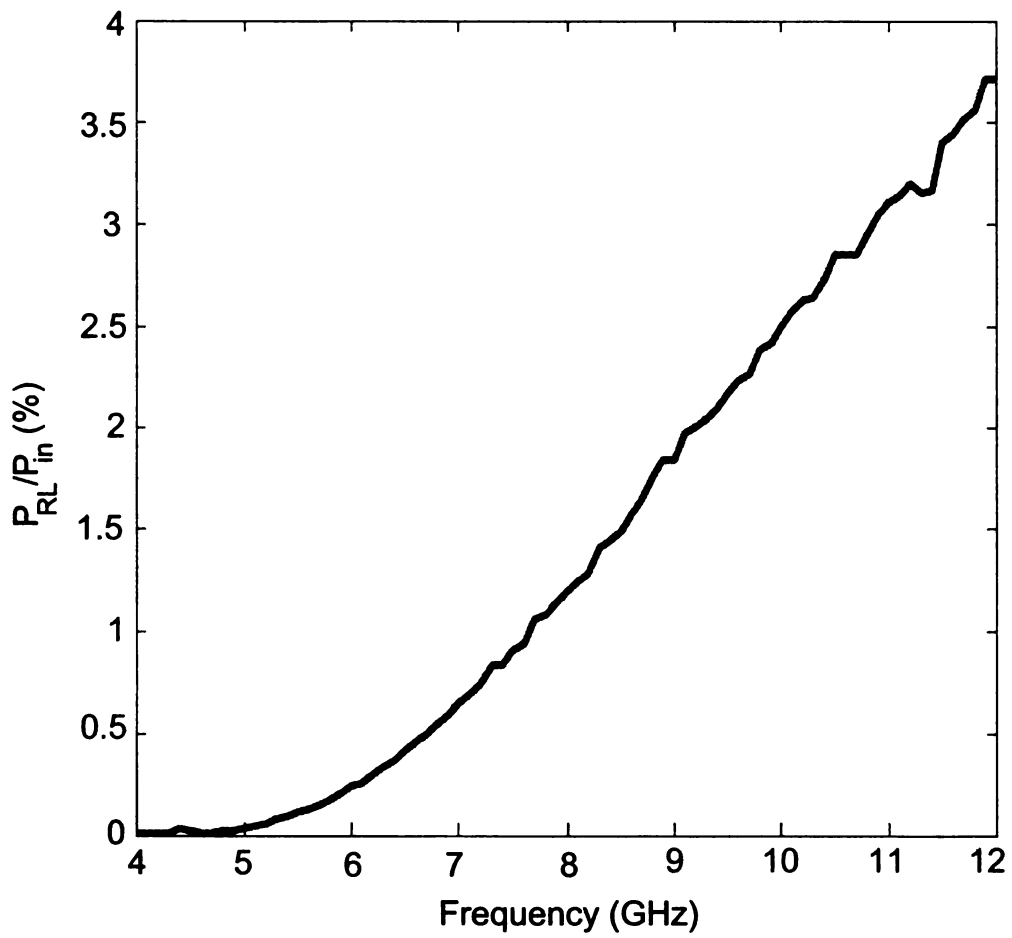


Figure 4.28. Ratio P_{RL} to P_{in} of the TLW antenna with circular termination.

CHAPTER 5

CONCLUSIONS AND FUTURE WORK

The contribution of this dissertation lies in the balun used to feed and in concert with the load to terminate a trough leaky-wave antenna. The main feature of this technique is its simplicity because this balun does not require the addition of significant complexity. The propagation constants are fundamental for the analysis and design of leaky-wave antennas. In this work, these constants were computed using the transverse resonance method in order to have an initial idea of the behavior of the input impedance and radiation pattern of the antenna. Since this method assumes an axially-infinite structure, the finite element boundary integral method was used to design a finite-length antenna. For this design several balun shapes were considered e.g., rectangular, bow-tie and circular. It was found that the circular termination was the most suitable in terms of VSWR and front to back ratio. The finite element boundary integral method was shown to be able to extract the propagation constants in order to validate the transverse resonance approach.

A trough leaky wave antenna filled with RT/Duroid 5880 was designed. Its impedance bandwidth was approximately 15.71% and its front to back ratio of 20 dB at 8.0 GHz. In addition, a trough leaky wave antenna filled with air was designed. The impedance bandwidth was approximately 40% and the front to back ratio was 20 dB at 12.0GHz.

In these two designs, a forward traveling-wave was obtained as it is shown on

Figure 4.8 and Figure 4.22, respectively. At high frequencies, standing waves started to appear on the antenna aperture. Standing waves are the result of a backward traveling-wave from the termination of the antenna. An optimum design requires minimizing backward traveling-waves. Since the magnitude of the oscillations in the air-filled case are less strong than in the duroid-filled case; it is evident that less energy is reflected from the load when the trough is filled with air. Reducing standing waves in a traveling-waves antenna is equivalent to optimize its antenna operational bandwidth. As it was expected, the operational bandwidth for the air-filled trough leaky-wave antennas is much larger than the one for the duroid-filled trough leaky-wave antenna.

Trough leaky-wave antennas and microstrip leaky-wave antennas are in general easy to feed. One of the advantages of the through leaky-wave antenna with respect to microstrip leaky-wave antennas is that it does not need a dielectric to support the conductor strip over the ground plane. This feature adds flexibility to the antenna design process.

At the time of this dissertation defense a trough leaky wave antenna prototype was in fabrication process. Unfortunately, experimental data was not available for this defense. As a future work, the simulated data will be compared with the experimental data in order to validate this design process and assess the feasibility of the trough leaky-wave antenna. In addition, new feeding techniques will be investigated in order to design a more efficient trough leaky-wave antenna.

APPENDICES

APPENDIX A

REVIEW OF SOME COMPLEX VARIABLE FUNCTIONS

A.1 The exponential function $w(z) = e^z$

In this appendix it is further discussed the properties of the function $w(z) = e^z$, considered in chapter 2 (section 2.1). The exponential is a single-valued function of its argument. Here, the complex variable z is defined as $z = re^{j\theta} = x + jy$, without loss of generality it is assumed $r = 1$. Consider any point z_0 in the complex z plane and any path from z_0 through the plane back to z_0 , a single value function is such that its value changes continuously along the path, returning to its original value at z_0 . Figure A.1 (a) shows the circular path in the z plane and Figure A.1 (b) shows the corresponding path in the w plane. If the start point is $z_0 = 1$ and the path followed is counter clock wise along the unit circle, this path is closed in the z plane (Figure A.1 (a)) as well as the path in the w plane (Figure A.1 (b)). For instance, let $z_1 = (r, \theta)$ and $z_2 = (r, \theta + 2\pi)$. It is clear that z_1 and z_2 represent the same point in the z plane. Substituting these two points into $w(z)$ yields the expressions

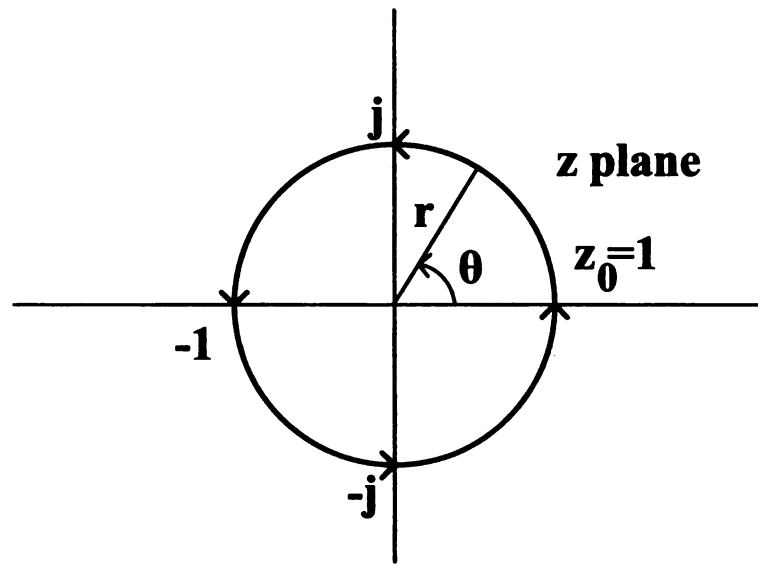
$$w(z_1) = e^{z_1} = e^{re^{j\theta}} \quad (\text{A.1})$$

$$w(z_2) = e^{z_2} = e^{re^{j(\theta+2\pi)}} \quad (\text{A.2})$$

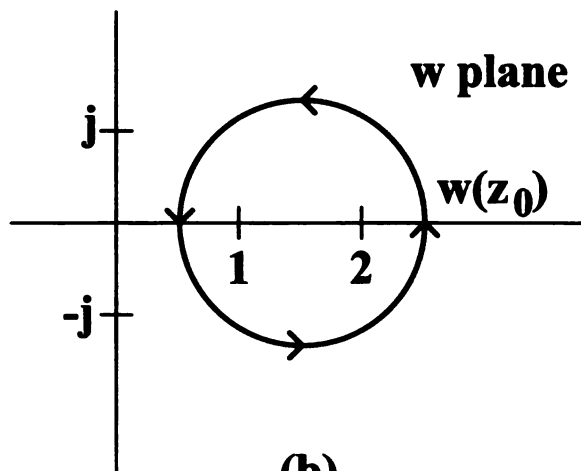
Since $e^{j(\theta+2\pi)}$ is periodic with period 2π , (A.1) and (A.2) represent the same point in the w plane. Therefore, the same value of e^z is obtained for different circuits e.g., θ , $\theta + 2\pi$, $\theta + 4\pi$, etc.

A.2 The square root function $w(z) = \sqrt{z}$

The square root is a double-valued function of its argument; this function was also considered in chapter 2 (section 2.1). Consider the definition of the complex variable $z = re^{j\theta}$ (assuming $r = 1$) and the closed path shown on Figure A.2 (a), starting at $r = 1, \theta = 0$. Figure A.2 (b) shows the corresponding path in the w plane, this path is not a closed one. After making a complete circle around the origin in the z plane the point $w = -1$ is obtained instead of $w = 1$. In order to arrive to $w = 1$, it is necessary to make a complete circle one more time ($2\pi \leq \theta < 4\pi$) in the z plane. But this new circle is not in the same sheet as the first one. Note that in this way it is avoided to encircle the origin. For the case $w(z) = \sqrt{z}$ two sheets are enough to characterize the values of $w(z)$ in a single-valued manner. Each one of these sheets are known as Riemann sheets [49]. The top sheet is cut along the positive real axis and joined the bottom sheet as shown on Figure A.2 (a). This cut is known as branch cut and $z = 0$ is known as branch point. The branch cut is chosen arbitrary but the branch point is a true singularity. It is usually convenient to take the branch cut along the positive or negative real axis.



(a)



(b)

Figure A.1. (a) A circular contour in the z plane. (b) The mapping of the z plane into w plane by the function e^z .

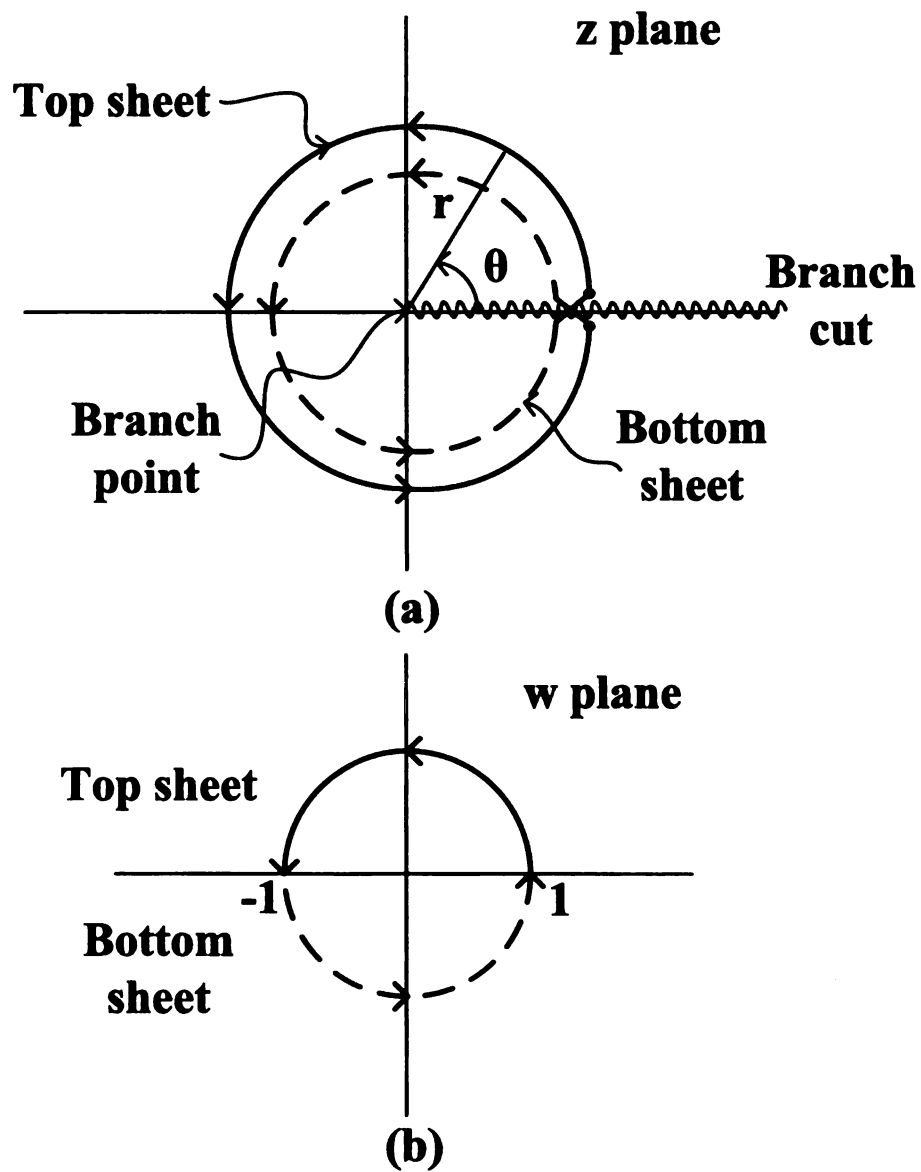


Figure A.2. (a) A circular contour in the z plane. (b) The mapping of the z plane into w plane by the function \sqrt{z} .

APPENDIX B

THIN-SUBSTRATE APPROXIMATION FOR MICROSTRIP PATCH ANTENNAS

Kuester *et al.* [32] investigated oblique incidence of a TEM wave in a dielectric-filled parallel-plate wave guide. This approximation is used to evaluate χ on (2.27) which is given by

$$\chi = 2 \tan^{-1} \left(\frac{\sqrt{k^2 - k_x^2}}{k_x} \tanh \Delta \right) - f_e(k_x^2) \quad (\text{B.1})$$

where

$$\Delta = \frac{w\sqrt{k^2 - k_x^2}}{\pi} \left\{ \frac{1 - \epsilon_r}{\epsilon_r} \left[\ln \left(jw\sqrt{k_0^2 - k^2 + k_x^2} \right) + \gamma - 1 \right] + 2Q(-\delta_\epsilon) - 2Q(\delta_\mu) \right\} \quad (\text{B.2})$$

$$f_e(k_x) = \frac{-2k_x w}{\pi} \left[\frac{\ln \left(jw\sqrt{k_0^2 - k^2 + k_x^2} \right) + \gamma - 1}{\epsilon_r} + 2Q(-\delta_\epsilon) - \ln(2\pi) \right] \quad (\text{B.3})$$

$$\gamma = 0.577215665$$

$$\delta_{\varepsilon} = \frac{\varepsilon_r - 1}{\varepsilon_r + 1} \quad (\text{B.4})$$

$$\delta_{\mu} = \frac{\mu_r - 1}{\mu_r + 1} \quad (\text{B.5})$$

$$Q(-\delta_{\varepsilon}) = \sum_{m=1}^{\infty} \left[\frac{\varepsilon_r - 1}{\varepsilon_r + 1} \right]^m \ln(m) \quad (\text{B.6})$$

$$Q(\delta_{\mu}) = 0 \quad (\text{B.7})$$

For $\varepsilon_r = 2.33$, equation (B.6) converges very rapidly, (i.e., $m > 10$) as it is shown on Figure B.1

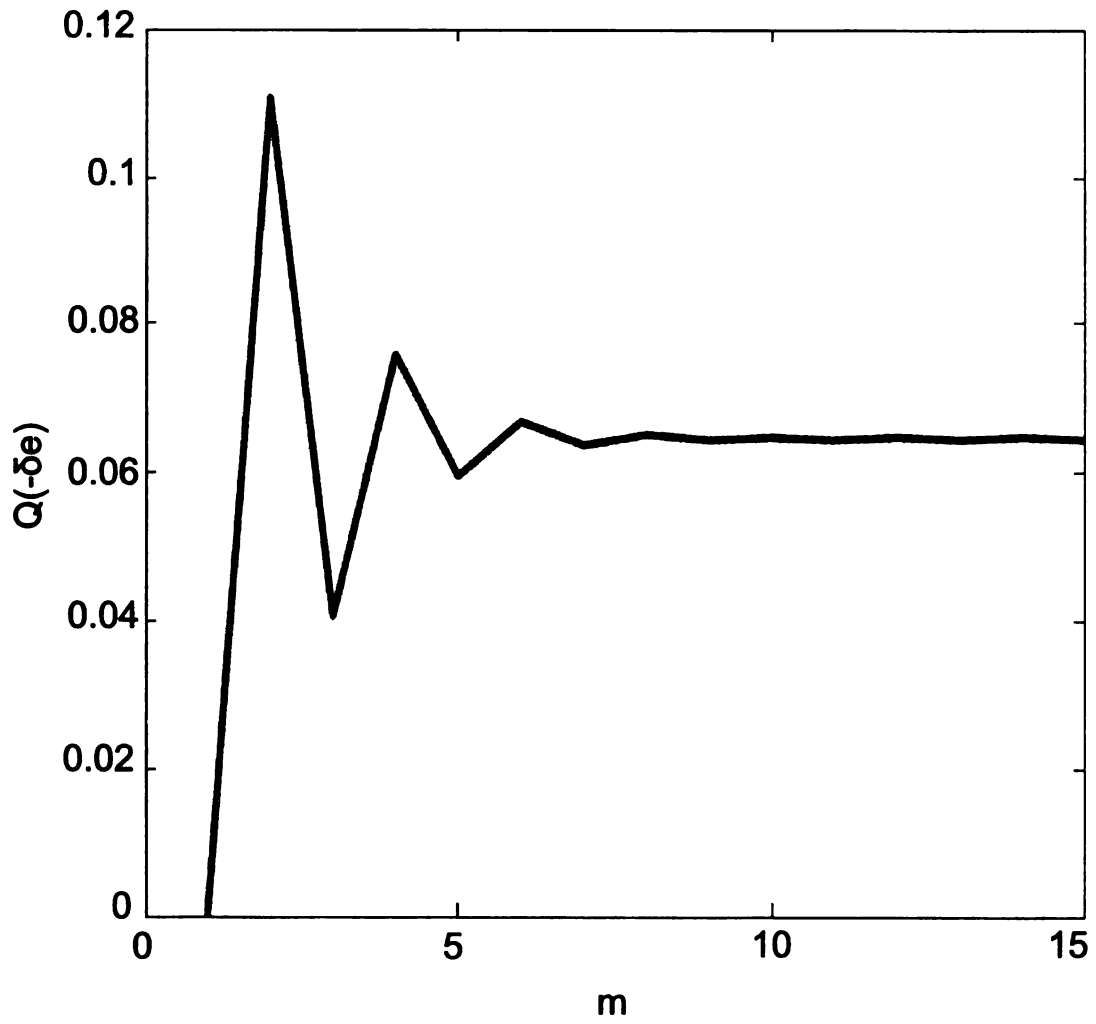


Figure B.1. Convergence for equation (B.6), ($\epsilon_r = 2.33$).

APPENDIX C

PROOF OF SOME PROPERTIES OF RWG BASIS FUNCTION

C.1 Proof of expression (3.114)

In this appendix it is proven expression (3.114) given in section 3.6. In addition, it is shown that its right hand side is zero. In order to be able to use the Gauss divergency theorem, the argument of the left hand side of (3.114) must have a continuous partial derivative on S' and C . If the triangles (Figure C.1) T_i^+ and T_i^- have continuous derivatives across their common edge l^c , they do not have any edge on the boundary. Therefore, Gauss divergency theorem can be used directly on the whole domain, this is,

$$\begin{aligned}
 \int_{S'} \nabla' \cdot \left[\left(\frac{e^{-jk_0 R}}{R} \right) (\hat{z} \times \vec{W}_j) \right] dS' &= \oint_C \left(\frac{e^{-jk_0 R}}{R} \right) (\hat{z} \times \vec{W}_j) \cdot \hat{m} dl \\
 &= \int_{l_1^+} \left(\frac{e^{-jk_0 R}}{R} \right) (\hat{z} \times \vec{W}_j) \cdot \hat{m} dl + \int_{l_2^+} \left(\frac{e^{-jk_0 R}}{R} \right) (\hat{z} \times \vec{W}_j) \cdot \hat{m} dl \\
 &\quad + \int_{l_1^-} \left(\frac{e^{-jk_0 R}}{R} \right) (\hat{z} \times \vec{W}_j) \cdot \hat{m} dl + \int_{l_2^-} \left(\frac{e^{-jk_0 R}}{R} \right) (\hat{z} \times \vec{W}_j) \cdot \hat{m} dl \quad (C.1)
 \end{aligned}$$

From expression (3.120),

$$\hat{z} \times \sum_i E_i \vec{W}_i = - \sum_i M_i \vec{f}_i(\vec{r}) \quad (C.2)$$

assuming that the expansion coefficients $E_i = M_i$, therefore

$$\hat{z} \times \vec{W}_i = -\vec{f}_i(\vec{r}) \quad (\text{C.3})$$

where $\vec{f}_i(\vec{r})$ are RWG basis function given on expression (3.119). Substituting (C.3) into equation (C.1), this becomes

$$\begin{aligned} \int_{S'} \nabla' \cdot \left[\left(\frac{e^{-jk_0 R}}{R} \right) \vec{f}_i(\vec{r}) \right] dS' &= \oint_C \left(\frac{e^{-jk_0 R}}{R} \right) \vec{f}_i(\vec{r}) \cdot \hat{m} dl \\ &= \int_{l_1^+} \left(\frac{e^{-jk_0 R}}{R} \right) \frac{l_i}{2A_i^+} \vec{\rho}_i^+ \cdot \hat{m} dl + \int_{l_2^+} \left(\frac{e^{-jk_0 R}}{R} \right) \frac{l_i}{2A_i^+} \vec{\rho}_i^+ \cdot \hat{m} dl \\ &\quad + \int_{l_1^-} \left(\frac{e^{-jk_0 R}}{R} \right) \frac{l_i}{2A_i^-} \vec{\rho}_i^- \cdot \hat{m} dl + \int_{l_2^-} \left(\frac{e^{-jk_0 R}}{R} \right) \frac{l_i}{2A_i^-} \vec{\rho}_i^- \cdot \hat{m} dl \quad (\text{C.4}) \end{aligned}$$

The resulting current interpolation for two triangles is shown on Figure C.1. This basis function has no component normal to the upper or lower edges of either triangle but only to the common edge. The direction of current is normal to the unit vector \hat{m} , the four integrals of (C.4) turn out to be zero.

On the other hand, if there is a boundary edge on either T_i^+ or T_i^- , the Gauss divergency theorem should be used on each triangle, this is,

$$\begin{aligned}
& \int_{S'} \nabla' \cdot \left[\left(\frac{e^{-jk_0 R}}{R} \right) \vec{f}_i(\vec{r}) \right] dS' = \oint_C \left(\frac{e^{-jk_0 R}}{R} \right) \vec{f}_i(\vec{r}) \cdot \hat{m} dl \\
& = \int_{T_i^+} \left(\frac{e^{-jk_0 R}}{R} \right) \frac{l_i}{2A_i^+} \vec{\rho}_i^+ \cdot \hat{m} dl + \int_{T_i^-} \left(\frac{e^{-jk_0 R}}{R} \right) \frac{l_i}{2A_i^-} \vec{\rho}_i^- \cdot \hat{m} dl \quad (C.5)
\end{aligned}$$

The integral over T_i^+ can be found as

$$\begin{aligned}
& \int_{T_i^+} \left(\frac{e^{-jk_0 R}}{R} \right) \frac{l_i}{2A_i^+} \vec{\rho}_i^+ \cdot \hat{m} dl = \int_{l_1^+} \left(\frac{e^{-jk_0 R}}{R} \right) \frac{l_i}{2A_i^+} \vec{\rho}_i^+ \cdot \hat{m} dl \\
& + \int_{l_2^+} \left(\frac{e^{-jk_0 R}}{R} \right) \frac{l_i}{2A_i^+} \vec{\rho}_i^+ \cdot \hat{m} dl + \int_{lc} \left(\frac{e^{-jk_0 R}}{R} \right) \frac{l_i}{2A_i^+} \vec{\rho}_i^+ \cdot \hat{m} dl \quad (C.6)
\end{aligned}$$

In a similar way, the integral over T_i^- is computed as

$$\begin{aligned}
& \int_{T_i^-} \left(\frac{e^{-jk_0 R}}{R} \right) \frac{l_i}{2A_i^-} \vec{\rho}_i^- \cdot \hat{m} dl = \int_{l_1^-} \left(\frac{e^{-jk_0 R}}{R} \right) \frac{l_i}{2A_i^-} \vec{\rho}_i^- \cdot \hat{m} dl \\
& + \int_{l_2^-} \left(\frac{e^{-jk_0 R}}{R} \right) \frac{l_i}{2A_i^-} \vec{\rho}_i^- \cdot \hat{m} dl + \int_{lc} \left(\frac{e^{-jk_0 R}}{R} \right) \frac{l_i}{2A_i^-} \vec{\rho}_i^- \cdot \hat{m} dl \quad (C.7)
\end{aligned}$$

Since the current direction is normal to \hat{m} the integrals over l_1^+ , l_2^+ , l_1^- , and l_2^- are zero on (C.6) and (C.7). Substituting (C.6) and (C.7) into (C.5) yields,

$$\oint_C \left(\frac{e^{-jk_0 R}}{R} \right) \vec{f}_i(\vec{r}) \cdot \hat{m} dl = \int_{lc} \left(\frac{e^{-jk_0 R}}{R} \right) \frac{l_i}{2A_i^+} \vec{\rho}_i^+ \cdot \hat{m} dl +$$

$$\int_{lc} \left(\frac{e^{-jk_0 R}}{R} \right) \frac{l_i}{2A_i^-} \vec{\rho}_i^- \cdot \hat{m} dl \quad (C.8)$$

The last two integrals on the right hand side of (C.8) have the same magnitude but opposite sign. Therefore, (C.1) or (C.8) becomes

$$\oint_C \left(\frac{e^{-jk_0 R}}{R} \right) \vec{f}_i(\vec{r}) \cdot \hat{m} dl = 0 \quad \text{Q.E.D} \quad (C.9)$$

C.2 RWG basis function are free of charge accumulation over its support

In this section, the Gauss divergence theorem is used to prove that RWG basis function are free of charge accumulation over its support.

From the current continuity condition for magnetic charges:

$$\nabla \cdot \vec{M}(\vec{r}) = -j\omega\rho_m(\vec{r}) \quad (C.10)$$

where ρ_m is the charge magnetic density on a triangle patch. The net charge on the support is given by

$$Q_m = \int_S \rho_m(\vec{r}) d\vec{r}. \quad (C.11)$$

Substituting (C.10) into (C.11) yields

$$Q_m = \frac{-1}{j\omega} \int_S \nabla \cdot \vec{M}(\vec{r}) d\vec{r} \quad (\text{C.12})$$

Using (3.118), equation (C.12) becomes

$$\begin{aligned} Q_m &= \frac{-1}{j\omega} \int_S \nabla \cdot \sum_i M_i \vec{f}_i(\vec{r}) d\vec{r} = \\ &= \frac{-\sum_i M_i}{j\omega} \int_S \nabla \cdot \vec{f}_i(\vec{r}) d\vec{r} \end{aligned} \quad (\text{C.13})$$

At this point, it is possible to use the result obtained on appendix C.2, in specific (C.9) to write

$$\begin{aligned} Q_m &= \frac{-\sum_i M_i}{j\omega} \int_S \nabla \cdot \vec{f}_i(\vec{r}) d\vec{r} = \\ &= \oint_C \vec{f}_i(\vec{r}) \cdot \hat{m} dl = 0 \end{aligned} \quad (\text{C.14})$$

which means that the net charge over the triangles shown on Figure C.1 is zero.

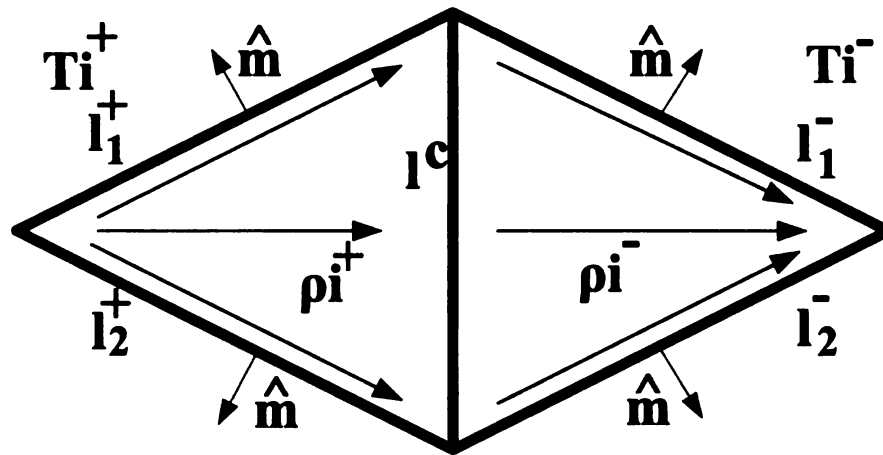


Figure C.1. Current interpolation between two triangles.

APPENDIX D

ANALYTICAL COMPUTATION OF INTEGRALS WITH SINGULARITIES

In this appendix it is discussed the computation of integrals with singularities encountered in 3.6.2. The derivation of these integrals is found on [41]. These singularities are of two type: uniform source distribution and linearly varying source distribution.

D.1 Integrals with uniform source distribution

These integrals contain proportional terms to

$$\int_{T^q} \frac{1}{R} dS' \quad (\text{D.1})$$

where T^q is a triangle element. The analytical computation for integrals of this type is given by

$$\begin{aligned} \int_{T^q} \frac{1}{R} dS' = & \sum_i \hat{P}_i^0 \cdot \hat{u}_i \left[P_i^0 \ln \frac{R_i^+ + l_i^+}{R_i^- + l_i^-} - |d| \right. \\ & \left. \times \left(\tan^{-1} \frac{P_i^0 l_i^+}{(R_i^0)^2 + |d| R_i^+} - \tan^{-1} \frac{P_i^0 l_i^-}{(R_i^0)^2 + |d| R_i^-} \right) \right] \end{aligned} \quad (\text{D.2})$$

where

$$\hat{l}_i = \frac{\vec{r}_i^+ - \vec{r}_i^-}{|\vec{r}_i^+ - \vec{r}_i^-|}$$

$$\hat{u}_i = \hat{l}_i \times \hat{n}$$

$$R_i^\pm = |\vec{r} - \vec{r}_i^\pm|$$

$$l_i^\pm = (\vec{\rho}_i^\pm - \vec{\rho}) \cdot \hat{l}_i$$

$$\vec{\rho}_i^\pm = \vec{r}_i^\pm - (\hat{n} \cdot \vec{r}_i^\pm) \hat{n}$$

$$P_i^0 = |(\vec{\rho}_i^+ - \vec{\rho}) \cdot \hat{u}_i|$$

$$\hat{P}_i^0 = \frac{(\vec{\rho}_i^+ - \vec{\rho}) - l_i^+ \hat{l}_i}{P_i^0}$$

$$R_i^0 = \sqrt{(P_i^0)^2 + d^2}$$

$$d = \hat{n} \cdot (\vec{r} - \vec{r}_i^\pm) \tag{D.3}$$

These vectors and scalars quantities are shown on Figure D.1. \vec{r}' is the position

vector from the origin to a source point on the triangular patch. \vec{r} is the position vector from the origin to an observation point. $\vec{\rho}'$ and $\vec{\rho}$ are the projections of \vec{r}' and \vec{r} respectively onto the plane of the patch. \vec{r}_i^\pm denotes the position vectors from the origin to the endpoints l_i^\pm . $\vec{\rho}^\pm$ is the projection of the position vector \vec{r}_i^\pm onto the patch plane. d is the height of the observation point above the patch surface. P_i^0 is the perpendicular distance of the projected observation point in the plane of the patch to the i th-edge of the patch. The unit vector \hat{l}_i is tangent to the i th-edge and points in the direction of increasing length. The unit vector \hat{u}_i is the outward normal vector to the i th-edge.

D.2 Integrals with linearly varying source distribution

These integrals contain proportional terms to

$$\int_{Tq} \frac{\vec{\rho}' - \vec{\rho}}{R} dS' \quad (\text{D.4})$$

The analytical computation for integrals of this type is given by

$$\int_{Tq} \frac{\vec{\rho}' - \vec{\rho}}{R} dS' = \frac{1}{2} \sum_i \hat{u}_i \left[\left(R_i^0 \right)^2 \ln \frac{R_i^+ + l_i^+}{R_i^- + l_i^-} + R_i^+ l_i - R_i^- l_i^- \right] \quad (\text{D.5})$$

The vectors and scalars quantities given on (D.5) are defined on (D.3) and Figure D.1.

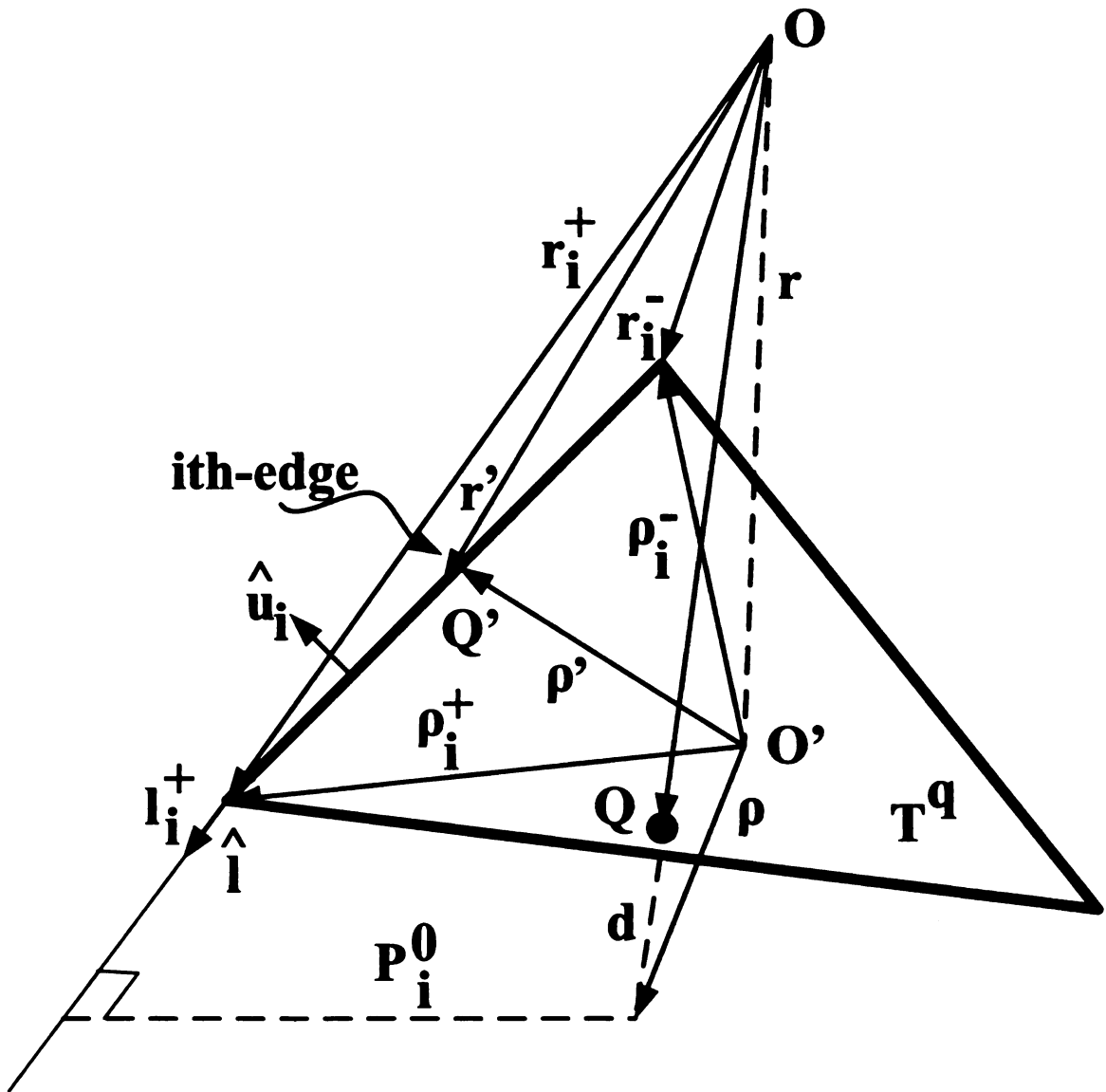


Figure D.1. Geometrical parameters associated with the evaluation of potential integrals over the triangle T^q (after [50]).

BIBLIOGRAPHY

BIBLIOGRAPHY

- [1] V. H. Rumsey, "Traveling Wave Slot Antennas," *Journal of applied physics*, vol. 24, pp. 1358-1365, November 1953.
- [2] R. F. Harrington, "Propagation Along a Slotted Cylinder," *Journal of applied physics*, vol. 24, pp. 1366-1371, November 1953.
- [3] L. O. Goldstone and A. A. Oliner, "Leaky-wave Antennas I: Rectangular Waveguides," *IRE transaction on antennas and propagation*, vol. AP-7, pp. 307-319, October 1959.
- [4] J. N. Hines, V. H. Rumsey, and C. H. Walter, "Traveling Wave Slot Antennas," *Proceedings of the IRE*, vol. 41, pp. 1624-1631, November 1953.
- [5] A. A. Oliner, "Leakage from Higher Modes on Microstrips Line with Applications to Antennas," *Radio science*, vol. 22, pp. 907-912, November 1987.
- [6] J. D. Kraus. *Antennas*. Mc Graw Hill, New York, 1950.
- [7] K. S. Lee, *Microstrip Line Leaky-Wave Antenna*. PhD thesis, Polytechnic University of New York, 1986.
- [8] P. Baccarelli, P. Burghignoli, F. Frezza, Alli. A., and P. Lampariello. "Novel Modal Properties and Relevant Scanning Behaviors of Phased Arrays of Microstrip Leaky-Wave Antennas," *IEEE Trans. Antennas and propagation*, 51(12), 3228-3238, December 2003.
- [9] A. A. Oliner and D. Jackson. "Leaky-Wave Antennas," Ch. 11, *Antennas Engineering Handbook*, Editor: J. L. Volakis, Mc Graw Hill, New York, Fourth edition, 2007.
- [10] W. Hong, T. L. Chen, C. Y. Chang, J. W. Sheen, and Y. D. Lin. "Broadband Tapered Microstrip Leaky-Wave Antenna," *IEEE Trans. Antennas and propagation*, 51(12), 1922-1928, August 2003.

- [11] L. C. Kempel, S. Schneider, T. Kastle, and G. A. Thiele. "Comparison of Two Termination Schemes for a Half-Width Leaky-Wave Antenna," URSI National Radio Science Mtg., Washington D.C., July 2005.
- [12] G. M. Zelinski, M. L. Hastriter, M. J. Havrilla, J. S. Radcliffe, A. J. Terzuoli, and G. A. Thiele. "FDTD Analysis of a New Leaky Traveling Wave Antenna," IEEE/ACES Int. Conf., Honolulu, Hawaii, April 2005.
- [13] F. W. Byron, R. W. Fuller. Mathematics of classical and quantum physics. Dover publications Inc., New York, 1992.
- [14] D. Killips, J. S. Radcliffe, L. C. Kempel, and S. Schneider. "Radiation by a Linear Array of Half-Width Leaky-Wave Antennas," ACES Journal, 21, 248-255, November 2006.
- [15] C.A. Jaramillo-Henao, L.C. Kempel and S. Schneider, "Simulation of Microstrip Leaky-Wave Antennas on Inhomogeneous Substrates Using Transverse Resonance and Finite Element Methods," Electromagnetics, vol. 28, pp. 27-41, January 2008.
- [16] Y. D. Lin, J. W. Sheen, and C. Tzuang. "Analysis and Design of Feeding Structures for Microstrip Leaky Wave Antennas," IEEE Trans. Microwave Theory Tech., 44(9), 1540-1547, September 1996.
- [17] J. L. Volakis, A. Chatterjee, and L. C. Kempel. Finite Element Method for Electromagnetics: Antennas, Microwave Circuits and Scattering Applications. IEEE Press, New York, 1998.
- [18] L.C. Kempel. "Computational Electromagnetics for Antennas", Ch. 59, Antennas Engineering Handbook, Editor: J. L. Volakis, Mc Graw Hill, New York, Fourth edition, 2007.
- [19] D.B. Davidson. Computational Electromagnetics for RF and Microwave Engineering. Cambridge University Press, 2005.
- [20] M. Abramowitz, I. Stegun. Handbook of Mathematical Functions With Formulas, Graphs and Mathematical Tables. Dover, 1965.
- [21] D. M. Pozar. Microwave Engineering. 3rd edition, Wiley, New York, 2005.
- [22] J. Jin. The Finite Element Method in Electromagnetics. John Wiley and Sons, New York, 2002.

- [23] D. P. Nyquist, D. R. Johnson, and S. V. Hsu. "Orthogonality and Amplitude Spectrum of Radiation Modes Along Open-Boundary Waveguides," *J. Opt. Soc. Am.*, 71, 49-54, September 1981.
- [24] G.M. Zelinski, Finite Difference Time Domain (FDTD) Analysis of a Leaky traveling Wave Microstrip Antenna. Master Thesis, Air Force Institute of Technology, Wright-Paterson Air Force Base, OH, 2005
- [25] C.H. Walter. *Traveling Wave Antennas*. McGraw-Hill, New York, 1965.
- [26] A. Hessel, "General characteristic of traveling-wave antennas," *Antenna Theory*, R. E. Collin and F. J. Zucker, New York: McGraw-Hill, 1969, ch. 19.
- [27] J. S. Bagby, C. H. Lee, D. P. Nyquist, and Yuan Y. "Identification of Propagation Regimes on Integrated Microstrip Transmission Lines," *IEEE Trans. Microwave Theory Tech.*, 41(11), 1887-1893, November 1993.
- [28] R.F. Harrington. *Time-Harmonic Electromagnetic Fields*. John Wiley and Sons, New York, 2001.
- [29] D. P. Nyquist. *Antenna Theory –Class Notes*. Michigan State University, East Lansing, MI, 2001.
- [30] IEEE Standard Definitions of Terms for Antennas, IEEE Standard 145-1993, Piscataway, IEEE.
- [31] W.L. Stutzman and G.A. Thiele, *Antenna Theory and Design*. John Wiley and Sons, New York, 1981.
- [32] E. F. Kuester, R. T. Johnk, and D. C. Chang. "The Thin-Substrate Approximation for Reflection from the End of a Slab-Loaded Parallel-Plate Waveguide with Application to Microstrip Patch Antennas," *IEEE Trans. Antennas and propagation*, 30(5), 910-917, September 1982.
- [33] G.M. Zelinsky, Finite Difference Time Domain (FDTD) Analysis of a Leaky Traveling Wave Microstrip Antenna. Ms Thesis, Air Force Institute of Technology, Wright-Patterson Air Force Base, Ohio, 2005
- [34] H. Jiang, R. Penno, K.M. Pasala, L.C. Kempel, S. Schneider. "Broadband Microstrip Leaky Wave Antenna with Inhomogeneous Materials," *IEEE Trans. Antennas and propagation*, 57(5), 1557-1561, May 2009.
- [35] C.A. Balanis. *Advanced Engineering Electromagnetics*. Wiley, New Jersey, 1989.

- [36] C. T. Tai. Dyadic Green Functions in Electromagnetic Theory. IEEE Press, New Jersey, 1994.
- [37] R. E. Collin. Field Theory of Guided Waves. IEEE Press, New York, 1991.
- [38] O.C. Zienkiewicz. The Finite Element Method in Engineering. McGraw Hill, New York, 1971.
- [39] E.J. Rothwell, M.J. Cloud. Electromagnetics. CRC Press, Florida, 2009.
- [40] S.M. Rao, D.R. Wilton, A.W. Glisson. "Electromagnetic Scattering by Surfaces of Arbitrary Shape," IEEE Trans. Antennas and propagation, 30(3), 409-418, May 1982.
- [41] D.R. Wilton, S.M. Rao, A.W. Glisson, D.H. Schaubert, O.M. Al-Bundak, C.M. Butler. "Potential Integrals for Uniform and Linear Source Distributions on Polygonal and Polyhedral Domains," IEEE Trans. Antennas and propagation, 32(3), 276-281, March 1984.
- [42] J.S. Savage, A.F. Peterson. "Quadrature Rules for Numerical Integration over Triangles and Tetrahedra," IEEE Antennas and Propagation Magazine, 38(3), 100-102, June 1996.
- [43] M. Merriman. A Text-book on The Method of Least Squares. 8th. edition, John Wiley and Sons, New York, 1960.
- [44] S.J. Chapman. Fortran 90/95 for Scientists and Engineers. 2nd. edition, McGraw-Hill, 2004.
- [45] A. Awhadiya, P. Barba, and L.C. Kempel. "Finite Element Method Programming Made Easy???", IEEE Antennas and Propagation Magazine, 45(4), Aug 2003.
- [46] D.B. Davidson. "Implementation Issues for Three-Dimensional Vector FEM Programs," IEEE Antennas and Propagation Magazine, 42(6), 100-107. Dec 2000.
- [47] C.A. Jaramillo, L.C. Kempel, S.W. Schneider. "A Trough Leaky Wave Antenna," APS, Jun 2009, Charleston, South Carolina.
- [48] C.A. Balanis. Antenna Theory Analysis and Design. Wiley, New Jersey, 1982.
- [49] J. Mathews, R.L. Walker. Mathematical Methods of Physics. Addison Wesley, California, 1964.

- [50] C.A. Macon, Modeling the Radiation from Cavity-Backed Antennas on Prolate Spheroids Using a Hybrid Finite Element-Boundary Integral Method. Ph.D. Thesis, Michigan State University, East Lansing, MI, 2001.
- [51] John D'Angelo, <http://www.skybluesystems.com>
- [52] J. Meese, L. Kempel, and S. Schneider. "Subdividing Distorted Prims into Tetrahedra," 19th Review of Progress in Applied Computational Electromagnetics, Monterey, CA, March 2003.

MICHIGAN STATE UNIVERSITY LIBRARIES



3 1293 03063 1042